

UNIVERSITÉ DU QUÉBEC  
INRS - ÉNERGIE MATÉRIAUX TÉLÉCOMMUNICATIONS

**Subcycle nonlinear terahertz optics:  
a carrier dynamics approach**

By

Xin Chai

A thesis submitted in partial fulfillment of the requirements for the degree of  
Doctor of Philosophy (PhD) in Energy and Material Sciences

Jury Members

President of the jury    Dr. Luca Razzari (INRS-EMT)  
& Internal examiner

External examiner    Dr. Lyubov Titova (Worcester Polytechnic Institute)  
                                 Dr. Jean-Michel Ménard (University of Ottawa)

Research director    Dr. Tsuneyuki Ozaki (INRS-EMT)

## Acknowledgement

I am first and foremost grateful to my research advisor, Professor Tsuneyuki Ozaki. I was extremely lucky to have an exceptional and furthermore, a super cool research director. During my PhD, I have been struggling to solve certain problems and it really took some time. However, he always trusted me with the freedom to pursue challenging projects and gave me the resources to see them through to completion. In this he taught me to become an independent researcher. The discussions with Prof. Ozaki were always encouraging, interesting and fruitful. Moreover, Prof. Ozaki has provided me with many opportunities of potential collaborations, international conferences as well as my future career.

I would sincerely like to thank my colleague Dr. Xavier Ropagnol for his support during my PhD. It is his expertise on the large-aperture photoconductive antenna terahertz source that makes this dissertation even possible. He was always there to ask and working closely with him has truly been a pleasure.

I am very thankful to my former colleague Dr. Hassan. A. Hafez for his great help, especially during the first two years of my PhD. He was always inspiring and motivating me.

I'm grateful to Dr. Muhammad Ashiq Fareed, who is super nice and intelligent. He helped us a lot on improving the quality of our manuscript.

I would also like to thank the technical team of ALLS: Philippe Lassonde and Antoine Laramée for their huge help on maintaining and aligning the laser facilities. Nothing will come out with a bad laser.

I am also very grateful to Prof. Savel'ev's group from Lomonosov Moscow State University for their tremendous effort on the DSTMS THz source.

I would also like to thank Prof. Richard Martel and Prof. Pierre Lévesque for the collaboration and providing the gated graphene samples.

I'm also very thankful to Prof. François Blanchard for his help on improving our THz experimental setup and his trust on me for modelling some of his experimental results.

I would also like to thank the NTT group: Prof. Hiroki Hibino, Dr. Yoshiaki Sekine, Dr. Katsuya Oguri and Dr. Makoto Takamura for their collaboration and supplying graphene samples.

I'm extremely grateful for Prof. Marc Dignam and Prof. David Cooke for the fruitful discussions we had on graphene and on the initial results of  $\text{In}_{0.53}\text{Ga}_{0.47}\text{As}$ .

I'm also very grateful for my colleagues Denis Ferachou, Marie Kirouac-Turmel, Sudipta Mondal, Fatemeh Amirkhan, Luis Sanchez-Mora, Singh Mangaljit, Isgandarov Elchin, Carlos. M. Garcia-Rosas for their help and collaboration.

Great thanks to the members of the jury: Prof. Luca Razzari, Prof. Lyubov Titova and Prof. Jean-Michel Ménard for reviewing and evaluating my thesis.

In the end, I would like to thank my family and my friends for everything. It has been a wonderful journey and I'm pretty sure that everything will become better and better.

## Abstract

The dynamics of free electrons in semiconductors play the central role in strong light-matter interaction with intense terahertz radiations. Terahertz pulse can serve as a transient voltage bias to drive high-field phenomena in solids. Various nonlinear effects can be excited by applying different terahertz field strengths and the observed experimental results are found to be extremely sensitive to the incident terahertz spectrum and its temporal profile. These properties suggest a rich variety of possible optoelectronic applications by controlling the carrier dynamics in semiconductors.

In this thesis, we investigate the nonlinear terahertz responses of free charge carriers in semiconductors, such as the *n*-doped semiconductor  $\text{In}_{0.53}\text{Ga}_{0.47}\text{As}$  and graphene, with terahertz time-domain spectroscopy as well as optical pump-terahertz probe spectroscopy. We start by discussing the terahertz responses of monolayer graphene. Then we discuss the significant impact of temporal dynamics in subcycle nonlinear optics. There are several limitations of the conventional Drude model and more importantly, the experimental observations may differ significantly within the well-known THz window. Strong subcycle nonlinear optics can only be achieved by carefully taking into account the time-scale of the variation in the temporal conductivity. Different experimental results are observed using different coherent terahertz sources in the frequency range between 0.1 and 3 THz. To retrieve nonlinear optics in the subcycle regime, we performed nonlinear THz-TDS on a common doped semiconductor material  $\text{In}_{0.53}\text{Ga}_{0.47}\text{As}$ , which possesses a much higher carrier density and a high conductivity contrast before and after strong carrier heating induced by intervalley scattering. Our findings suggest an incoherent

approach to subcycle control of terahertz high-frequency (or high-harmonic) generation based on intraband carrier scattering effects. These investigations will be important for future terahertz electronics and optoelectronics.

# Table of Contents

Acknowledgement.....	i
Abstract .....	iii
Chapter 1. Introduction .....	1
Chapter 2. Nonlinear time-resolved terahertz spectroscopy .....	3
2.1 Photoconductive antenna terahertz source .....	4
2.2 Optical rectification .....	8
2.3 Electro-optic sampling technique .....	12
2.4 Terahertz time-domain spectroscopy .....	16
2.5 Optical-pump terahertz-probe spectroscopy .....	19
Chapter 3. Terahertz spectroscopy of graphene.....	21
3.1 Terahertz electrodynamics of graphene .....	21
3.2 Ambient temperature effects on the carrier dynamics in graphene .....	23
3.3 Nonlinear terahertz time-domain spectroscopy of gated graphene .....	29
Chapter 4. Nonlinear terahertz optics induced by intraband carrier dynamics.....	33
4.1 Nonlinear THz intraband conductivity .....	33
4.2 Intuition of subcycle nonlinear THz optics induced by carrier scattering .....	36
4.3 Ensemble Monte-Carlo approach .....	40
Chapter 5. Subcycle nonlinear terahertz optics.....	46
5.1 Half-cycle nonlinear terahertz optics .....	47
5.2 Adding another half-cycle pulse with opposite polarity .....	53
5.3 Terahertz Harmonic generation due to intervalley scattering effect (theory) .....	62
Chapter 6. From intraband to interband nonlinear terahertz optics .....	66
6.1 Observation from intraband to interband carrier dynamics .....	67
Chapter 7. From linear to circular ponderomotive acceleration .....	77
7.1 Generation of elliptically polarized terahertz pulses .....	78
7.2 Elliptically polarized THz-TDS on $\text{In}_{0.53}\text{Ga}_{0.47}\text{As}$ .....	79
7.3 Development of detection approach using Stokes-Mueller formalism.....	81
Chapter 8. Conclusions and Perspectives.....	91
References .....	94



## List of Figures

Fig.2.1: Schematic diagram of the THz generation from a photoconductive antenna. A bias voltage $V_b$ is applied on the semiconductor substrate to drive the photoexcitation carriers. ....	4
Fig.2.2: A photo of the iLAPCA source (without binary mask) developed at ALLS. ....	6
Fig.2.3: THz pulses generated from a ZnSe based iLAPCA THz source. The inset shows the corresponding spectrum. Here, the long negative half-cycle is cut at 6.4 ps due to the overlap with the back reflected pulses from the detection crystal, substrate of the studied sample and the antenna substrate. ....	7
Fig.2.4: Schematic diagram of the THz generation by using titled-pulse-front technique in a $\text{LiNbO}_3$ crystal. ....	10
Fig.2.5: Quasi-single-cycle THz pulses generated from a $\text{LiNbO}_3$ crystal via OR. The inset shows the corresponding spectrum. ....	11
Fig.2.6: (a) Schematic diagram of the THz detection system using EO sampling technique. (b) A femtosecond laser pulse serves as an ultrafast detector to scan the THz waveforms. ....	12
Fig.2.7: Schematic diagram of a THz-TDS set-up. ....	16
Fig.2.8: Normal incidence and transmission of THz electric field through a thin conducting film deposited on a dielectric substrate: (a) substrate - thin film configuration and (b) thin film – substrate configuration, where another Fresnel loss at the substrate-air interface should be taken into account for the measured field by EO sampling. ....	17

Fig.2.9: (a) Schematic diagram of an optical/IR-pump THz-probe system (b) Differential transmission signal of a photoexcited GaAs substrate..... 19

Fig.3.1: THz-TDS measurements by changing the ambient temperature: the transmitted THz pulses (a) and (c) and the normalized peak field (b) and (d) for *p*-doped CVD graphene and *n*-doped epitaxial graphene. Adapted from [43]. ..... 25

Fig.3.2: Ambient temperature effects on the THz photoconductivity of graphene after photoexcitation:  $\Delta T/T_0$  as a function of the delay time between the optical pump and the THz probe beams for (a) *n*-doped epitaxial graphene, (c) *p*-doped CVD graphene, the black and red arrow indicate the reduction and enhancement of differential transmission by increasing the sample temperature; (b) and (d) are the corresponding peak of  $\Delta T/T_0$  as a function of the temperature for CVD graphene and epitaxial graphene. Adapted from [43]. ..... 26

Fig.3.3: Heating effect on the Fermi energy in (a) highly *p*-doped CVD graphene and (b) lightly *n*-doped epitaxial graphene. Adapted from [43]. ..... 27

Fig.3.4: Nonlinear THz-TDS of gated graphene: (a) THz peak transmission as a function of the Fermi energy for various THz field strengths. The arrow indicates the transmission enhancement with THz electric field for a certain Fermi energy. (b) Field-dependence of THz peak transmission at different Fermi energies. .... 29

Fig.3.5: The simulation results of the field-dependent scattering time as well as the electron temperature. Here, the phonon and electron temperatures are assumed to be identical for simplicity. .... 30

Fig.4.1: THz temporal profile of a half-cycle THz pulse generated from iLAPCA, where the THz field strength varies continuously. .... 35

Fig.4.2: Time evolution of the average electron drift velocity upon the application of a step-like electric field of 60 kV/cm according to the dynamic intervalley-electron-transfer model. Adapted from [51]. .... 37

Fig.4.3: Monte-Carlo simulation of carrier transport driven by a square-wave like electric field . (a) Applied transient electric field in time. (b) Calculated average drift velocity versus time for electrons in GaAs at room temperature. Adapted from [66]. .... 39

Fig.4.4: Intervalley scattering rates by absorption (ab) and emission (em) of phonons. (a)  $\Gamma$ -valley, (b) L valleys, (c) X valleys. The 0 eV energy corresponds to the bottom of each valley..... 43

Fig.5.1: (a) Amplitude spectra of the transmitted THz pulses through the bare substrate ( $E_{ref}$ ) and the InGaAs sample ( $E_{trans}$ ) with the incident peak field of 190 kV/cm. Inset: corresponding THz waveforms, where the blue arrow indicates the propagation direction. (b) Measured field dependence of  $E_{trans}$  and half-cycle duration (amplitude FWHM) as a function of the incident peak field  $E_{in}$  measured in air. (c) Measured transmission spectra at various incident fields. The gray area corresponds to the transmission lower than 1. (d) Calculated transmission spectra based on the described model. .... 48

Fig.5.2: (a) Incident THz waveform and the calculated current density with the field strength of 190 kV/cm. (b) Schematic of the experiment in momentum space: intense THz transient induces

carrier intervalley scattering. The increased field strength leads to a damping of the subcycle current density (or a current density cut) and an increase in the total relaxation time. (c) Impact of current drop on the transmitted THz waveforms of three tested field strengths shown in Fig. 5.1. The transmitted waveforms are normalized by the corresponding peak values. (d) Normalized transmitted THz waves obtained from calculation. .... 50

Fig.5.3: Calculated normalized temporal current density (black solid lines), and carrier populations in the  $\Gamma$ , L and X valleys at various fields of (a) 80 kV/cm, (b) 129 kV/cm, (c) 145 kV/cm and (d) 190 kV/cm, respectively (ensemble Monte-Carlo simulation). Due to strong intervalley scattering rates, some statistical fluctuations are shown on the normalized current density..... 51

Fig.5.4: (a) Schematic of the iLAPCA with a binary phase mask. Quasi-single-cycle THz wave is generated by inducing a time delay between two half-cycles. (b) the transmitted THz waveform through the substrate and (c) the corresponding spectrum, where several crests are shown due to the interference between the positive and negative polarities. .... 54

Fig.5.5: Transmitted THz pulses (solid black curve) and the instantaneous THz intensity (broken green curve) at various incident fields of (a) 74 kV/cm. (b) 105 kV/cm. (c) 130 kV/cm. and (d) 177 kV/cm. (e) the transmitted fields of negative ( $E_{neg}$ ) and positive extremes ( $E_{pos}$ ) versus the incident field. Inset:  $\Delta E_{trans}/E_{pos}$ , where  $\Delta E_{trans} = E_{pos}-E_{neg}$ . (f) field dependence of half-cycle durations (amplitude FWHM). Four field regions can be identified, representing: 1, the linear regime; 2, current truncation on the negative polarity; 3, current truncation on the positive polarity and 4, pulse broadening of the negative polarity. .... 55

Fig.5.6: Calculated temporal dynamics of intraband free carriers driven by quasi-single-cycle THz pulse (ensemble Monte-Carlo simulation). Normalized absolute value of the current density (gray shaded area), carrier population in  $\Gamma$  (magenta curve), L (broken green line) and X (blue point curve) valleys at different incident field strengths: (a) 74 kV/cm. (b) 117 kV/cm. (c) 137 kV/cm and (d) 177 kV/cm. .... 57

Fig.5.7: Simulated transmitted THz pulses at (a) 74 kV/cm. (b) 117 kV/cm. (c) 137 kV/cm and (d) 177 kV/cm. (e) the transmitted peak fields of negative ( $E_{neg}$ ) and positive ( $E_{pos}$ ) half-cycle pulses versus the incident THz field. (f) field dependence of half-cycle duration (amplitude FWHM). 59

Fig.5.8: (a) Calculated carrier average velocity driven by the quasi-single-cycle pulses with a peak field of 160 kV/cm. (b) average carrier energy at three valleys. The carrier momentum distribution at (a) 0.0 ps. (b) 2.17 ps. (d) 2.65 ps and (d) 4.4 ps. .... 61

Fig.5.9: HHG from single-cycle and multi-cycle THz pulses centered at 0.2 THz (Simulation). (a) nonlinear current density driven by single-cycle THz pules centered at 0.2 THz. The applied peak field is 180 kV/cm.  $t_{relax}$  corresponds to the carrier relaxation time and  $t_{E_{THz}}$  represents the acceleration time to scatter the carriers to side valleys. (b) the intensity spectra of the  $E_{in}$  and  $E_{trans}$ . The intensity is normalized to the peak intensity of  $E_{in}$ . (c) nonlinear current density driven by multi-cycle THz pules centered at 0.2 THz. The peak incident field used here is 350 kV/cm. (d) the normalized intensity spectra of the  $E_{in}$  and  $E_{trans}$ . .... 64

Fig.6.1: (a) Experimental-setup. The THz pulse energy is measured using a calibrated Golay Cell. (b) THz Michelson interferometer is used to retrieve the THz spectra. (c) THz intensity spectra. (d) Radiated THz pulse energies as a function of the IR pump energy. .... 68

Fig.6.2: Z-scan normalized transmission (enhancement ratio) of various THz pulse energies measured by the Golay cell. All the transmitted THz energies are normalized to the transmitted THz energy at  $Z = -15.3$  mm. .... 70

Fig.6.3: (a) Transmitted energy ratio between InGaAs sample and bare InP substrate versus the incident THz pulse energy at different Z-scan positions. (b) Calculated results by the described intraband model, where the time-domain simulations are performed at each  $50 \mu\text{m}$ . .... 71

Fig.6.4: Incident and calculated transmitted THz waveforms (a), (c), (e) as well as the corresponding average carrier energy (b), (d), (f) at 0.15, 0.3 and 1 MV/cm, respectively. .... 74

Fig.7.1: (a) A photo of the ZnSe based iLAPCA with crossed electrodes. (b) a combination of shadow and binary phase mask is used here to generate THz pulses with tunable ellipticity. Three phase plates can be placed before the vertically or horizontally oriented electrodes. .... 78

Fig.7.2: Transmitted THz waveforms through the bare InP substrate  $E_{\text{ref}}$  as well as the InGaAs sample  $E_{\text{trans}}$  with different thickness of phase masks of (a) 1, (b) 0.2 and (c) 0.12 mm. .... 79

Fig.7.3: Experimental set-up. We use a polarization state analyzer that is composed of two liquid crystal variable retarders and a Wollaston prism. .... 81

Fig.7.4: Schematic diagram of the detection system with a polarization state analyzer (PSA), which is composed of two liquid crystal variable retarders (LCVR) and one Wollaston prism. . 83

Fig.7.5: Temporal Stokes parameters of the probe beam (a) S0, (b) S1, (c) S2, and (d) S3. (e) The extracted THz signals by using the system with a PSA and by using the conventional EO sampling technique. .... 86

Fig.7.6: Temporal Stokes parameters of the probe beam (a) S1, and (b) S3. (c) Measured THz signals by using the system with a PSA and by using the conventional EO sampling technique. 87

Fig.7.7: Temporal Stokes parameters of the probe beam (a) S1, (b) S2, and (c) S3. (d) Measured 3D THz waveform. .... 89

## Publications during the PhD

[1]. **X. Chai**, X. Ropagnol, L. Sanchez Mora, S. Mohsen Raeis-Zadeh, S. Safavi-Naeini, F. Blanchard and T. Ozaki, “Stokes-Mueller method for full characterization of coherent terahertz waves with ultrahigh dynamic range.” (to be submitted).

[2]. **X. Chai**, X. Ropagnol, S. Mohsen Raeis-Zadeh, M. Reid, S. Safavi-Naeini, and T. Ozaki. “Subcycle nonlinear terahertz optics with elliptically polarization”, (to be submitted).

[3] **X. Chai**, X. Ropagnol, A. Ovchinnikov, O. Chefonov, A. Ushakov, C. M. Garcia-Rosas, E. Isgandarov, M. Agranat, T. Ozaki, and A. Savel’ev. “Observation of crossover from intraband to interband nonlinear terahertz optics.” *Optics Letters* 43, no. 21: 5463, (2018).

- [4]. F. Blanchard, **X. Chai**, X., T. Tanaka, T. Arikawa, T. Ozaki, R. Morandotti, and K. Tanaka, “Terahertz microscopy assisted by semiconductor nonlinearities.” *Optics Letters*, 43(20), 4997, (2018).
- [5]. **X. Chai**, X. Ropagnol, S. Mohsen Raeis-Zadeh, M. Reid, S. Safavi-Naeini, and T. Ozaki. “Subcycle Terahertz Nonlinear Optics.” *Physical Review Letters* 121, no. 14: 143901, (2018).
- [6]. O. V. Chefonov, A. V. Ovchinnikov, S. A. Romashevskiy, **X. Chai**, T. Ozaki, A. B. Savel’ev, M. B. Agranat, and V. E. Fortov. “Giant self-induced transparency of intense few-cycle terahertz pulses in n-doped silicon.” *Optics Letters* 42, no. 23: 4889, (2017).
- [7]. X. Ropagnol, **X. Chai**, S. M. Raeis-Zadeh, S. Safavi-Naeini, M. Kirouac-Turmel, M. Bouvier, C. Côté, M. Reid, M. A. Gauthier, and T. Ozaki. “Influence of Gap Size on Intense THz Generation From ZnSe Interdigitated Large Aperture Photoconductive Antennas.” *IEEE Journal of Selected Topics in Quantum Electronics* 23, no. 4: 1, (2017).
- [8]. H. A. Hafez, **X. Chai**, Y. Sekine, M. Takamura, K. Oguri, I. Al-Naib, M. M. Dignam, H. Hibino, and T. Ozaki. “Effects of environmental conditions on the ultrafast carrier dynamics in graphene revealed by terahertz spectroscopy.” *Physical Review B* 95, no. 16: 165428, (2017).
- [9]. H. A. Hafez, **X. Chai**, A. Ibrahim, S. Mondal, D. Férachou, X. Ropagnol, and T. Ozaki. “Intense terahertz radiation and their applications.” *Journal of Optics* 18, no. 9: 093004, (2016).
- [10]. H. A. Hafez, P. L. Lévesque, I. Al-Naib, M. M. Dignam, **X. Chai**, S. Choubak, P. Desjardins, R. Martel, and T. Ozaki. “Intense terahertz field effects on photoexcited carrier dynamics in gated graphene.” *Applied Physics Letters* 107, no. 25: 251903(2015).
- [11]. H. Razavipour, W. Yang, A. Guermoune, M. Hilke, D. G. Cooke, I. Al-Naib, M. M. Dignam, F. Blanchard, H. A. Hafez, **X. Chai**, and D. Ferachou. “High-field response of gated graphene at terahertz frequencies.” *Physical Review B*, 92(24), 245421, (2015).

## Patent

[1]. X. Chai and T. Ozaki, “Method and system for terahertz radiation detection and characterization”, US deposition reference: 14448. 168.

## Contributions to international conferences during the PhD

[1]. X. Ropagnol, **X. Chai**, M. Raeiszadeh, S. Safavi-Naeini, M. Reid, and T. Ozaki. “Intense THz Source of Sub-Cycle Pulses with Tunable Elliptical Polarization.” In 2018 43rd International Conference on Infrared, Millimeter, and Terahertz Waves (IRMMW-THz), IEEE, 2018.

[2]. **X. Chai**, X. Ropagnol, M. Raeiszadeh, S. Safavi-Nacini, M. Reid, and T. Ozaki. “Subcycle Nonlinear Terahertz Optics in Doped Semiconductor Thin Film.” 43rd International Conference on Infrared, Millimeter, and Terahertz Waves (IRMMW-THz), IEEE, 2018.

[3]. **X. Chai**, X. Ropagnol, M. Raeiszadeh, S. Safavi-Naeini, M. Reid, M. A. Gauthier, and T. Ozaki. “Extreme nonlinear carrier dynamics induced by intense quasi-half-cycle THz pulses in n-doped InGaAs thin film.” In CLEO: QELS\_Fundamental Science. Optical Society of America, 2017.

[4]. H. A. Hafez, P. L. Lévesque, I. Al-Naib, M. M. Dignam, **X. Chai**, S. Choubak, P. Desjardins, R. Martel, and T. Ozaki. “Optical-pump/intense-THz-probe spectroscopy of gated graphene.” In Infrared, Millimeter, and Terahertz waves (IRMMW-THz), 2016.

[5]. **X. Chai**, H. A. Hafez, I. Al-Naib, Y. Sekine, M. Takamura, K. Oguri, M. M. Dignam, H. Hibino, and T. Ozaki. “Effects of environmental changes on the carrier dynamics in graphene revealed by terahertz spectroscopy.” In Infrared, Millimeter, and Terahertz waves (IRMMW-THz), 2016.

[6]. **X. Chai**, X. Ropagnol, M. Raeiszadeh, S. Safavi-Naeini, M. Reid, M. A. Gauthier, and T. Ozaki. “Nonlinear ultrafast terahertz waveform modulation in highly n-doped In<sub>0.53</sub>Ga<sub>0.47</sub>As thin film.” In *Infrared, Millimeter, and Terahertz waves (IRMMW-THz)*, 2016.

[7]. H. A. Hafez, **X. Chai**, P. Lévesque, I. Al-Naib, M. Dignam, P. Lassonde, N. Thiré, F. Légaré, R. Martel, and T. Ozaki. “Carrier dynamics in gated graphene revealed by tunable-infrared-pump/terahertz-probe spectroscopy.” In *CLEO: Science and Innovations*. Optical Society of America, 2016.

[8]. H. H. Eid, P. Lévesque, I. Al-Naib, M. M. Dignam, **X. Chai**, D. Ferachou, R. Martel, and Ozaki, T. Ozaki. “Intense terahertz field-induced carrier dynamics in gated monolayer graphene.” In *CLEO: Science and Innovations*. Optical Society of America, 2015.

# Chapter 1

## Introduction

Terahertz (THz) radiation represents the electromagnetic spectrum that lies between the microwave and the far-infrared [1-3]. The typical THz window corresponds to the frequency range between 0.1 and 10 THz. In particular, this frequency range was called the “THz gap” due to the lack of efficient and compact table-top THz sources and detectors. During the last two decades, with the rapid development of THz sources and detection techniques, this commonly known “THz gap” has now become obsolete [3,4]. Efficient table-top THz sources, detectors and their applications have been facilitated by the advancement of the mode-locked femtosecond laser systems, which led to a fast progress in the applications of various fields, such as condensed matter physics, ultrafast photonics, biomedicine and communications [1,2].

One of the most interesting properties of this specific frequency range is its relatively low photon energy. For example, a 1 THz photon possess a photon energy of 4 meV, which is much smaller than the energy gap of common semiconductor materials. As a result, one can use THz spectroscopy to perform a straightforward contact-free and non-invasive detection of the ultrafast intraband carrier transport in doped semiconductor materials, or to monitor the relaxation of photoexcited carriers in semiconductors [4-6]. Hence, THz spectroscopy becomes a very convenient tool for the investigation of ultrafast carrier dynamics, which is essential for the applications of high-speed electronics and optoelectronics.

During the last decade, various THz sources and detection techniques have been developed using the laser facilities of the Advanced Laser Light Source (ALLS) at the INRS-EMT. The generated THz pulse energies have increased from a few nJ up to several  $\mu\text{J}$  [7-14]. Different techniques have been used, such as photoconductive generation, optical rectification as well as the relativistic plasma THz source. These THz sources possess different characteristics and can be used in different applications. In this study, we focus on THz generation from the nonlinear crystal  $\text{LiNbO}_3$  via optical rectification and the THz waves generated by a large-aperture photoconductive antenna.

In Chapter 2, we will discuss in detail these two THz generation techniques and the electro-optic sampling technique for coherent THz detection. Then, we will describe THz time-domain spectroscopy as well as optical-pump THz-probe spectroscopy. In Chapter 3, we will present the results of nonlinear THz spectroscopy of graphene and discuss the THz nonlinearities induced by scattering effects. In Chapter 4, we will discuss the limitation of the conventional Drude model and the importance of taking into account the time-scale of the nonlinearities. Then in Chapter 5, we will present the central content of this thesis --- subcycle nonlinear THz optics. We will present results of experiments on nonlinear spectroscopy of a doped semiconductor thin film along with detailed analysis and discussions, supported by ensemble Monte-Carlo simulation. In Chapters 6 and 7, we will discuss the role of interband carrier dynamics on the nonlinear THz responses and the initial experimental results using an elliptically polarized THz pulses, which also include a new detection method for such experiments.

## Chapter 2

### Nonlinear time-resolved terahertz spectroscopy

A great advantage of THz spectroscopy is that it allows a time-resolved electric field measurement, which is due to its pump-probe configuration nature. This is achieved by a fully coherent generation and detection configuration used in the THz spectroscopy system. In this section, we will start by discussing the THz generation and detection techniques with femtosecond laser systems, then introduce the technique of THz time-domain spectroscopy (THz-TDS) and optical-pump THz-probe (OPTP) spectroscopy.

In the presence of a medium, the generation of electromagnetic radiation can be described by the wave equation:

$$\nabla^2 E - \epsilon\mu \frac{\partial^2 E}{\partial t^2} = \mu \frac{\partial J}{\partial t} \quad (2.1)$$

Here,  $\mu$  is the permeability,  $\epsilon$  is the permittivity of the medium and is  $E$  the electric field.  $J$  can be induced by acceleration of free charge carriers or by oscillating bound electrons. A  $J(t)$  that evolves on the time scale of a few hundred femtoseconds to a few picoseconds will lead to the generation of electromagnetic waves in the THz frequency range. In this study, two THz sources are used, which are the photoconductive antenna (PCA) THz source and the THz source based on optical rectification (OR) in a nonlinear crystal. The PCA source is based on the acceleration of photoexcited carriers  $J(t)$  and on the other hand, OR is due to the anharmonically oscillating bound electrons (or polarization) in a noncentrosymmetric crystals.

## 2.1 Photoconductive antenna terahertz source

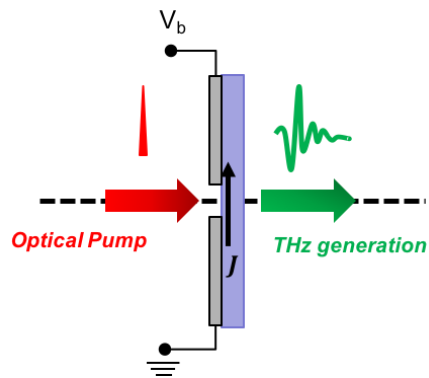


**Fig.2.1:** Schematic diagram of the THz generation from a photoconductive antenna. A bias voltage  $V_b$  is applied on the semiconductor substrate to drive the photoexcitation carriers.

The principal mechanism of THz generation from PCA is the surge current of photoexcited carriers accelerated by a bias field. For intense THz generation, large-aperture PCA (LAPCA) are normally used to increase the photoexcited area. Fig. 2.1 gives a schematic diagram of a LAPCA THz source with two electrodes deposited on a high-resistivity semiconductor substrate. Here, the femtosecond laser pulse, with a photon energy that is slightly higher than the bandgap of the semiconductor crystal, serves as a transient switch to generate free carriers in the substrate. Conversely to other THz source, the energy of the THz pulse is principally extracted from the DC field applied to the substrate rather than the optical energy.

In the far field, the emitted THz field is linearly proportional to the temporal derivative of the surged current density in the substrate [1,15]. Using the boundary condition of the generated

surface current in the substrate, the relation between the generated THz field in the far field and the applied DC field can be expressed as [1,2,4,6]:

$$E_{THz}(t) \propto \frac{\partial J}{\partial t} \propto E_b \frac{\partial \sigma(t)}{\partial t} \quad (2.2)$$

Here,  $E_{THz}(t)$  is the generated THz field in the far field,  $E_b$  is the bias electric field and  $\sigma(t)$  is the photoconductivity. The detailed derivation can be found in [1,15]. As can be seen from the relationship between the THz field  $E_{THz}(t)$  and the applied bias field, the generated THz peak field scales linearly with the bias field. In practice, this feature serves as the central guideline for the choice of the substrate material as well as the design of the antenna structure. For example, due to its relatively low breakdown field ( $\approx 10 \text{ kV/cm}$ ), semiconductor GaAs can only be used for conventional low-energy THz sources. Other wide bandgap materials such as ZnO and GaN have been demonstrated as better candidates for high-power LAPCA THz sources [16,17]. Since the laser wavelength we use at ALLS is at 800 nm, the semiconductor ZnSe was chosen as the substrate material for LAPCA [11]. It possesses a bandgap of 2.7 eV and therefore free carriers can be photoexcited by the second harmonic (400 nm) of a Ti:Sapphire laser system. With regard to the antenna structure, interdigitated LAPCA (iLAPCA) structure is currently the most widely used design for high-power THz source [4,15]. Ropagnol *et al.* [11,13] has developed a ZnSe based iLAPCA THz source at ALLS since 2013, and in 2016, with a surface area of  $12.2 \text{ cm}^2$ , a quasi-half-cycle THz pulse with an energy of  $8.3 \pm 0.3 \mu\text{J}$  was generated. As shown in Fig. 2.2, iLAPCA possesses a large photoexcitation surface area and furthermore, due to the reduced distance between different pairs of electrodes, relatively high-voltage source is not required in the experiment.

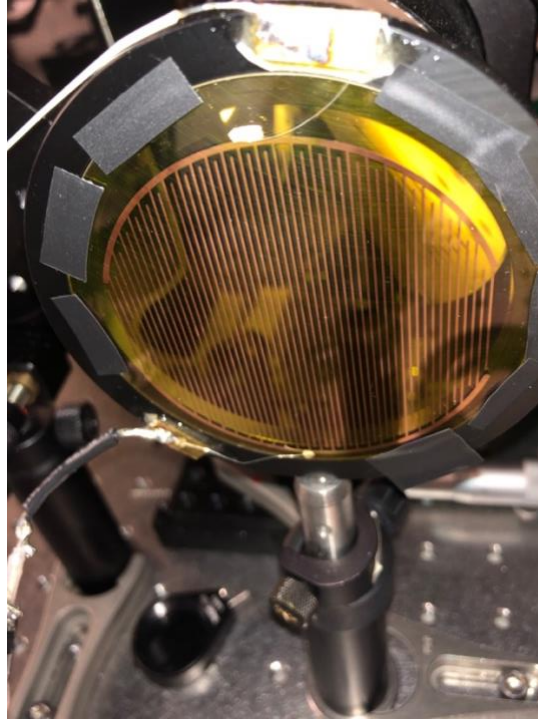


**Fig.2.2: A photo of the iLAPCA source (without binary mask) developed at ALLS.**

A second approach to increase the output THz power is by increasing the number of the generated free carriers with high pumping fluence. However, a saturation of THz emission from LAPCA will take place at high pump fluences due to the screening of the bias field by the emitted THz field [4,15]. As a result, when the LAPCA is operating in a saturation regime, the energy of the generated THz pulses become insensitive to the fluctuation of the pumping optical beam fluence. This saturation effect can then make iLAPCA a suitable THz source to operate at a low repetition rate laser system. As long as the iLAPCA is working under saturation regime, a good shot-to-shot stability can be easily achieved, which is essential for spectroscopic measurements if laser systems with low repetition rate are used. For example, the ZnSe iLAPCA source developed at ALLS is typically driven by the 10 Hz Ti: Sapphire laser system. Here, the system can provide

enough laser energy for the generation of pump pulse (approximately 15 mJ) at 400 nm to photoexcite the relatively large ZnSe substrate.

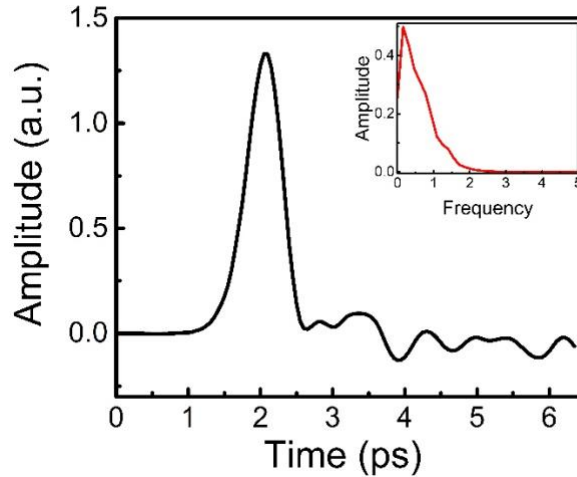


**Fig.2.3: THz pulses generated from a ZnSe based iLAPCA THz source. The inset shows the corresponding spectrum. Here, the long negative half-cycle is cut at 6.4 ps due to the overlap with the back reflected pulses from the detection crystal, substrate of the studied sample and the antenna substrate.**

Fig. 2.3 shows a typical THz pulse generated from our iLAPCA THz source. One unique property of the THz pulses generated from this iLAPCA is the strong asymmetry in the magnitude of the positive and negative components of the THz profile. This is caused by the rapid carrier acceleration followed by a slow reduction of the current density due to the long carrier relaxation from the conduction band to the valence band [15]. Hence, a quasi-half-cycle THz pulse is naturally generated. The second unique property of the generated THz waves is its low frequency, typically in the low THz frequency range between 0.05 and 1 THz. In the time domain, this

corresponds to a very long half-cycle duration with a high ponderomotive energy, which is advantageous for many applications such as free carrier acceleration.

## 2.2 Optical rectification

Optical rectification (OR) is a second-order nonlinear effect that takes place when the applied optical field is sufficiently strong to induce large electron displacements from equilibrium in a noncentrosymmetric crystal. The radiated THz field is expressed by the following equation [4,9]:

$$E_{THz} \propto \partial J_{bound} / \partial t = \partial^2 P(t) / \partial t^2 \quad (2.3)$$

By assuming two frequency components of the driving light field,  $E_1(t) = \cos(\omega_1 t)$  and  $E_2(t) = \cos(\omega_2 t)$ , the second-order polarization  $P^{(2)}(t)$  can be described by:

$$P(t) \propto \chi^{(2)} \cos(\omega_1 t) \cos(\omega_2 t) = \frac{\chi^{(2)}}{2} [\cos(\omega_1 + \omega_2)t + \cos(\omega_1 - \omega_2)t] \quad (2.4)$$

Here,  $E_{opt}$  is the electric field of the pump beam and  $\chi^{(2)}$  is the second-order electric susceptibility tensor. The first term in Eq. (2.3) is relevant for higher harmonic generation and the second term, which is the frequency difference, corresponds to the optical rectification. The interaction with intense laser field results in a quasi-DC polarization, leading to difference frequency generations in the THz frequency range. Hence, choosing the nonlinear crystals with high nonlinear coefficient at the optical pump wavelength is important for the improvement of the optical-to-THz conversion efficiency. For example, the most widely used nonlinear crystals at 800 nm are ZnTe ( $r_{41} = 4.04$  pm/V) and LiNbO<sub>3</sub> ( $r_{33} = 30.9$  pm/V) [4,9]. In addition, as the incident optical pump and the generated THz radiation propagates inside the nonlinear crystal, a phase matching condition between the optical group velocity and the THz phase velocity is also

crucial to build up the energy of the THz pulses. For example, ZnTe or DAST enables a simple collinear experimental configuration at 800 nm. However, the nonlinear coefficient of the ZnTe crystal is relatively low and high energy THz pulses can only be generated by using large aperture ZnTe crystal [7]. On the other hand, although organic crystals such as DAST possess higher conversion efficiency, they normally suffer from lower damage threshold compared with inorganic crystals [4,9]. The inorganic crystal LiNbO<sub>3</sub> is currently being used as an intense THz source in many THz laboratories. Due to the large difference in the refractive indices, a noncollinear configuration must be used to achieve proper phase matching conditions. For optical-to-THz conversion, the following two relations need to be fulfilled for conservation of energy and momentum:

$$\Delta\omega = \omega_1 - \omega_2 = \Omega_{THz} \quad (2.5)$$

$$\Delta k = k_1 - k_2 = K_{THz} \quad (2.6)$$

This leads to the phase matching conditions in the infinitesimal limit:

$$v_{THz,phase} = \frac{\Omega_{THz}}{K_{THz}} = \frac{\partial\omega}{\partial k} = v_{opt,gr} \quad (2.7)$$

The group velocity of the optical pump must be equal to the phase velocity of the THz waves. For stoichiometric LiNbO<sub>3</sub>, the optical group index  $n_{opt}$  is 2.25 for a pump wavelength  $\lambda_{pump}$  of 800 nm, while the THz phase refractive index is 4.96. As a result, phase matching condition can only be fulfilled at an angle of  $\gamma = 63^\circ$ , which gives:

$$v_{THz,phase} = v_{opt,gr} \cos \gamma \quad (2.8)$$

Experimentally, this can be realized by titling the pulse front using a diffraction grating.

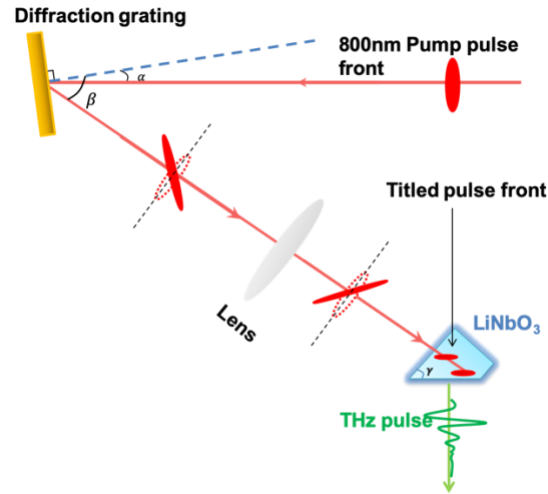


**Fig.2.4: Schematic diagram of the THz generation by using titled-pulse-front technique in a LiNbO<sub>3</sub> crystal.**

As shown in Fig. 2.4, with an incident angle  $\alpha$ , the diffraction angle  $\beta$  is defined through the grating equation  $\sin \alpha + \sin \beta = mN\lambda$ , where  $m$  is the diffraction order and  $N$  is the groove-density of the grating. Using a converging-lens with a demagnification factor  $F$ , the relation between  $\gamma$  and  $\beta$  is given as:

$$\tan \gamma = \frac{mFN\lambda}{n_{opt} \cos \beta} \quad (2.9)$$

Here, the LiNbO<sub>3</sub> crystal is cut at this angle in order to provide a normal output angle for the generated THz radiation.

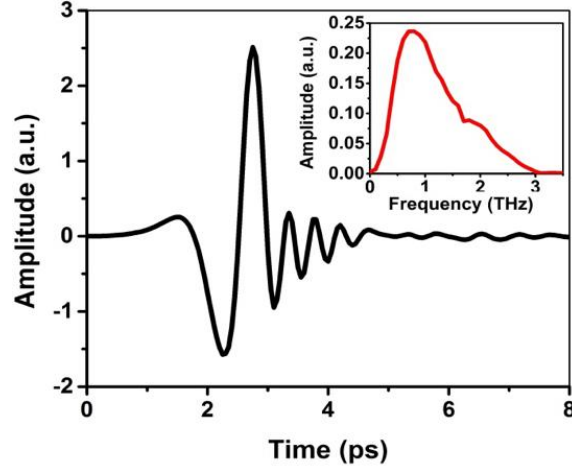


**Fig.2.5: Quasi-single-cycle THz pulses generated from a LiNbO<sub>3</sub> crystal via OR. The inset shows the corresponding spectrum.**

A typical THz pulse generated from the LiNbO<sub>3</sub> source is shown in Fig. 2.5. Quasi-single-cycle THz pulses are generated, and the central frequency normally lies around 0.75 THz. It is important to note that this frequency is approximately 5 times higher than that of the central frequency generated by the iLAPCA THz source (inset of Fig. 2.3). As we will discuss in the following chapters, even though they are both table-top THz sources, this difference may lead to very different experimental observations of nonlinear THz optics.

Due to the high conversion efficiency at 800 nm, the LiNbO<sub>3</sub> source based THz-TDS system can work with a high repetition rate laser system. The system used in this work was developed on the 2.5 kHz beamline of ALLS, giving rise to a high sensitivity, a better signal-to-noise ratio as well as fast scanning speed. The optical-pump THz-probe experiment was performed on this setup. The peak electric field of this THz source is between 60 and 70 kV/cm and a pair of wire-grid polarizers is used to vary the incident THz electric field on the investigated sample.

## 2.3 Electro-optic sampling technique

THz detection is the opposite process of generation and it can be realized by using either PCA or electro-optic (EO) sampling technique on a nonlinear crystal. The EO sampling technique utilizes the Pockels effect, which is analogous to THz generation by OR and is very popular due to its simplicity [1,2,18]. Here, a static (THz) electric field induces birefringence in nonlinear crystals such as ZnTe and GaP, and then modulates the polarization state of the transmitted optical beam.

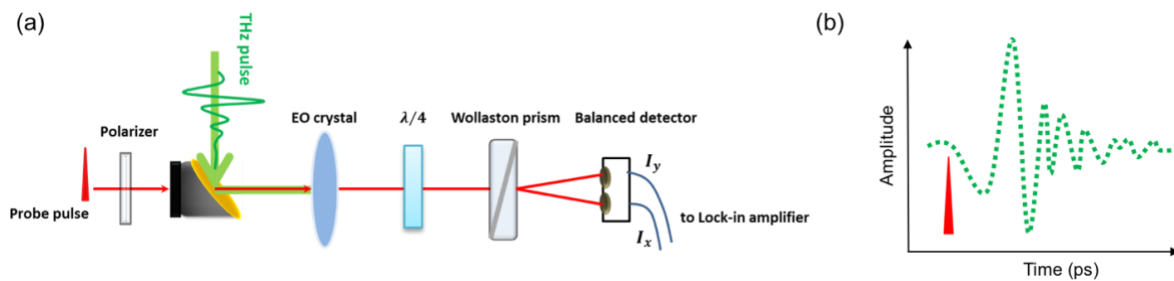


**Fig.2.6: (a) Schematic diagram of the THz detection system using EO sampling technique. (b) A femtosecond laser pulse serves as an ultrafast detector to scan the THz waveforms.**

A standard EO sampling detection system is shown in Fig. 2.6. A quarter-wave plate and a Wollaston prism are typically used for a balanced detection via two photodetectors. By using an optical delay stage, the femtosecond optical pulse can thus scan the THz temporal profile point by point, which makes THz-TDS extremely powerful because both amplitude and phase are resolved directly.

Here, we will derive in detail the EO sampling technique using the general Stokes-Mueller formalism and then explain its advantages and disadvantages. This is important as an introduction

and comparison to the technique described in Chapter 7.3, where we present an improved EO sampling approach based on the Stokes-Mueller formalism.

The Stokes vector represents the full polarization state of light, and the effect of a particular optical element is described by a  $4 \times 4$  Mueller matrix [19]. A Stokes vector contains four elements  $S_0, S_1, S_2$  and  $S_3$ . The first parameter  $S_0$  represents the total light intensity. Then  $S_1$  corresponds to the intensity difference between the horizontal and vertical polarization component. The third element  $S_2$  is the intensity difference between two linear polarization components orientated at  $\pm 45^\circ$  and the last element  $S_3$  represents the intensity difference between right- and left-hand circular polarization. Here, only  $S_0$  is observable in practice. We use a horizontally linearly polarized probe beam for THz detection and its corresponding Stokes vector can be written as:

$$S_{in} = \begin{pmatrix} 1 \\ 1 \\ 0 \\ 0 \end{pmatrix} \quad (2.10)$$

When the Pockels effect takes place, the detection crystal can be treated as a wave plate with its birefringence controlled by the THz electric field. For a (110) ZnTe or GaP detection crystal, the phase retardation  $\phi$  experienced by the probe beam over a thickness of  $d_{EO}$  is given as [2]:

$$\phi = \frac{\omega_0 d_{EO}}{2c} n_0^3 r_{41} E_{THz} \sqrt{1 + 3 \cos^2 \alpha} \quad (2.11)$$

Here,  $\omega_0$  is the optical frequency of the probe beam,  $c$  is the speed of light,  $n_0$  is the refractive index at the optical probe wavelength and  $r_{41}$  is the nonlinear coefficient of the specific nonlinear crystal. For a typical THz spectroscopy system, the THz polarization orientation  $\alpha$  is fixed horizontally ( $0^\circ$ ) and the generated refractive-index axes ( $\theta$ ) are along  $\pm 45^\circ$  according to the following equation [20]:

$$\cos 2\theta = \frac{\sin \alpha}{\sqrt{1+3\cos^2 \alpha}} \quad (2.12)$$

We use the Mueller matrix of a waveplate ( $M_{EO}$ ) with its axis oriented at  $\pm 45^\circ$ :

$$M_{EO} = \begin{pmatrix} 1 & 0 & 0 & 0 \\ 0 & \cos \phi & 0 & \sin \phi \\ 0 & 0 & 1 & 0 \\ 0 & -\sin \phi & 0 & \cos \phi \end{pmatrix} \quad (2.13)$$

And the transmitted Stokes vector of the probe beam is then obtained by multiplying  $M_{EO}$  with  $S_{in}$ :

$$S_{THz} = \begin{pmatrix} 1 \\ \cos \phi \\ 0 \\ -\sin \phi \end{pmatrix} = M_{EO} * S_{in} \quad (2.14)$$

Then after transmitted through a quarter-wave plate ( $M_{\lambda/4}$ ) with orientation of  $45^\circ$  and a Wollaston prism (vertically  $M_{VP}$  and horizontally  $M_{HP}$  linear polarizer), the final differential vector  $S_{diff}$  before for the two photodetectors becomes:

$$M_{\lambda/4} = \begin{pmatrix} 1 & 0 & 0 & 0 \\ 0 & 0 & 0 & 1 \\ 0 & 0 & 1 & 0 \\ 0 & -1 & 0 & 0 \end{pmatrix} \quad (2.15)$$

$$M_{VP} = \begin{pmatrix} 1 & -1 & 0 & 0 \\ -1 & 1 & 0 & 0 \\ 0 & 0 & 0 & 0 \\ 0 & 0 & 0 & 0 \end{pmatrix} * 0.5 \quad (2.16)$$

$$M_{HP} = \begin{pmatrix} 1 & 1 & 0 & 0 \\ 1 & 1 & 0 & 0 \\ 0 & 0 & 0 & 0 \\ 0 & 0 & 0 & 0 \end{pmatrix} * 0.5 \quad (2.17)$$

$$S_{diff} = M_{VP} * M_{\lambda/4} * S_{THZ} - M_{HP} * M_{\lambda/4} * S_{THZ} = \begin{pmatrix} \sin\phi \\ -1 \\ 0 \\ 0 \end{pmatrix} \quad (2.18)$$

As can be seen from equation (2.18), the lock-in amplifier measures straightforwardly the differential signal that is proportional to  $\sin\phi$ . Since this can be realized with a very simple experimental configuration, EO sampling technique have become the most widely used THz detection method in the THz community.

However, the one-dimensional measurement of  $\sin\phi$  also causes two problems for intense THz detection. Firstly, a small-angle approximation must be used, because the linear relationship no longer preserves when the phase retardation  $\phi$  becomes larger. Secondly, when the phase delay is above  $\pi/2$ , an over-rotation will take place due to the symmetric nature of the sinusoidal function around  $\pi/2$  [21]. These problems are two of the limitations of the EO sampling technique, which affects strongly the detection dynamic range [22]. In Chapter 7.3, we will introduce an improved EO sampling technique that solves this problem naturally, and can also provide additional information on the THz polarization orientation.

## 2.4 Terahertz time-domain spectroscopy

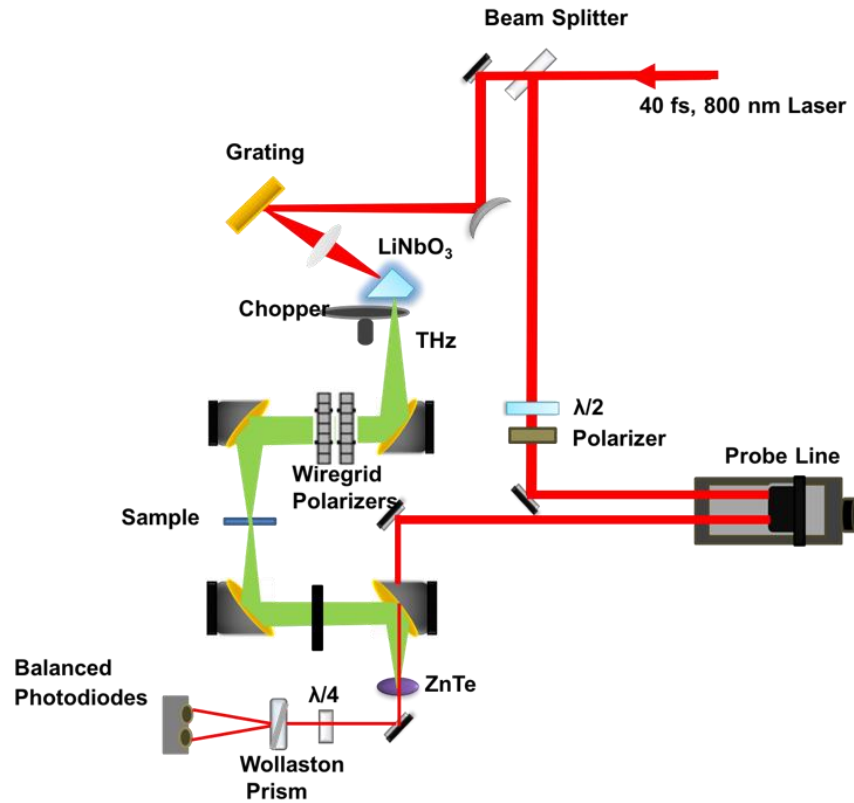
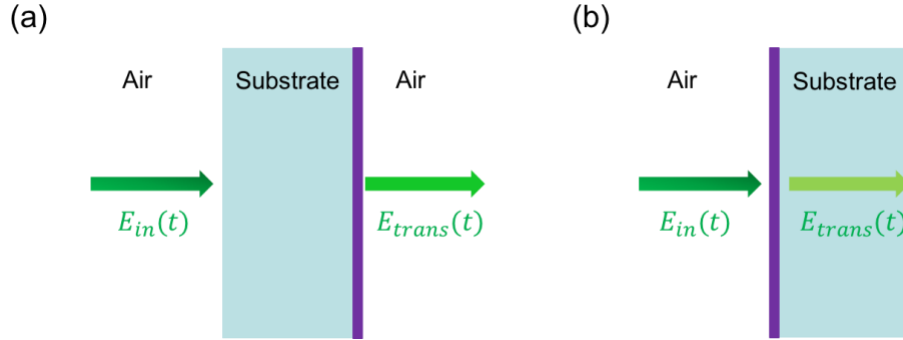


Fig.2.7: Schematic diagram of a THz-TDS set-up.

Since both amplitude and phase can be resolved directly, THz-TDS is an extremely powerful and convenient technique for investigating the dielectric properties of the material. Fig. 2.7 shows a typical THz-TDS system with a LiNbO<sub>3</sub> THz source. All the THz-TDS systems possess a similar configuration, in which the optical laser beam is separated into two parts. One part is used for THz generation and the other part with weak energy serves as the probe beam for THz detection. The generated THz beam is collected by one or two off-axis mirrors to first focus on the studied sample. Then another pair of off-axis mirrors are used to collect the THz beam and focus on the detection

crystal. To perform nonlinear measurements, one can use a pair of wire-grid polarizers to tune the incident THz intensity, or change the applied bias voltage on an iLAPCA THz source.



**Fig.2.8: Normal incidence and transmission of THz electric field through a thin conducting film deposited on a dielectric substrate: (a) substrate - thin film configuration and (b) thin film – substrate configuration, where another Fresnel loss at the substrate-air interface should be taken into account for the measured field by EO sampling.**

Two measurements are required for THz-TDS: one reference waveform measured in air  $E_{in}(t)$  or with a substrate of known dielectric properties  $E_{ref}(t)$ , and a second waveform  $E_{trans}(t)$  measured after transmission through the whole sample. Here, we will focus on a special case, where the sample is composed of one thin conducting film deposited on a semi-insulating substrate. In this thesis, both the  $n$ -doped semiconductor  $\text{In}_{0.53}\text{Ga}_{0.47}\text{As}$  sample as well as the graphene sample possess such configuration. In the thin-film limit, since the wavelength and skin depth are much larger than the thickness of the conducting film, the driving THz field is assumed to be uniform for all the charge carriers. The thin-film transmission equation in the time domain is given by [23]:

$$E_{trans}(t) = \frac{1}{Y_0 + Y_S} (2Y_0 E_{in}(t) - J(t)d) \quad (2.19)$$

Here,  $d$  is the thickness of the thin film.  $Y_0 = (377 \Omega)^{-1}$  is the free-space admittance,  $J(t)$  is the current density, and  $Y_S = NY_0$  is the admittance of the substrate, in which  $N$  is the refractive

index of the substrate. All the carriers in the thin film are assumed to experience the same driving field  $E_{trans}(t)$ . It is important to note that a Fresnel loss due to the transmission through the substrate-air interface should be taken into account to calculate the transmitted field in the air measured by the detection crystal.

As shown in Fig. 2.8, during the experiment, the sample can be placed in one of two possible configurations, *substrate – thin film* (Fig.2.8(a)) or *thin film – substrate* (Fig. 2.8(b)). Here, equation (2.19) corresponds to the experimental configuration of *thin film – substrate*. In fact, the two systems may lead to very different nonlinear THz transmissions and it is thus important to distinguish them in detail. As discussed in the following, nonlinear transmission could be much stronger for the configuration of *substrate – thin film* of Fig. 2. 8 (a). In this case, the incident THz field experiences first a Fresnel loss and the amplitude reduces to  $2/(N + 1)$  of the original field strength. In the thin film transmission equations, the free-space admittance  $Y_0$  also needs to be changed to  $Y_s$  before  $E_{in}(t)$ . The obtained THz transmission equation then becomes as:

$$E_{trans}(t) = \frac{1}{Y_0 + Y_s} \left( \frac{4Y_s}{N+1} E_{in}(t) - J(t)d \right) \quad (2.20)$$

By comparing the two factors before  $E_{in}(t)$  between equation (2.20) and equation (2.19), we obtain an increase ratio of  $2N/(N + 1)$ . Hence, for any substrate material with a refractive index of  $N > 1$ , the applied field on the thin conducting layer is higher for the configuration of *substrate – thin film – air*. For example, a refractive index of 3 will lead to an enhancement factor of 1.5, which is significant for any nonlinear THz measurements.

## 2.5 Optical-pump terahertz-probe spectroscopy

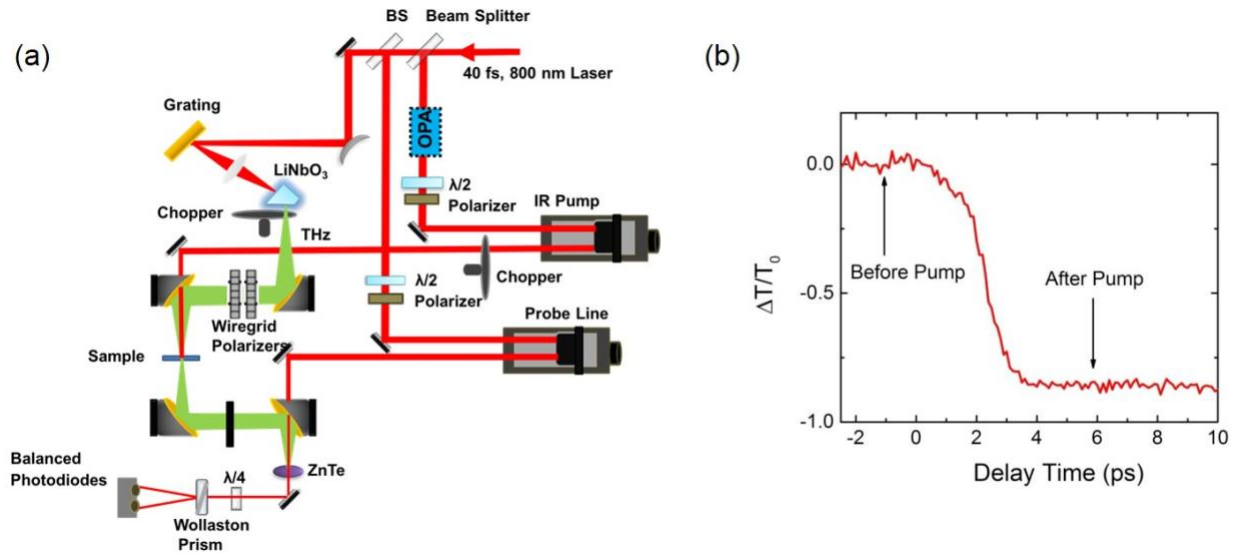


**Fig.2.9: (a) Schematic diagram of an optical/IR-pump THz-probe system (b) Differential transmission signal of a photoexcited GaAs substrate.**

The THz-TDS system is based on a THz-pump optical-probe configuration, and as a result we can retrieve the THz signal in the time domain using an EO sampling technique. On the other hand, we can also use the THz pulse to serve as a probe signal on the studied sample. For example, one widely used technique is optical-pump THz-probe (OPTP) spectroscopy. Here, a sample is photoexcited optically and then the THz pulse is used to probe the transient changes on the conductivities after photoexcitation. A schematic diagram of the experimental set-up is shown in Fig. 2.9 (a). Compared with the THz-TDS system, an extra delay line is added to tune the time delay between the optical pump and the THz pulse. Another optical chopper is used here on the pump line to obtain the differential signal  $\Delta T/T_0$ , which measures the change in the material property before and after photoexcitation with different time delays. Fig. 2.9 (b) shows the

measured differential signal  $\Delta T/T_0$  of a photoexcited GaAs semiconductor. The optical pump generates free charge carriers within the semiconductor sample and as a result we observe a THz absorption enhancement or transmission reduction with negative  $\Delta T/T_0$ . Due to the huge signal variation before and after photoexcitation, a bare substrate of GaAs or silicon is normally used to find the zero-time position of the OPTP experimental setup.

## Chapter 3

### Terahertz spectroscopy of graphene

#### 3.1 Terahertz electrodynamics of graphene

Graphene is a monolayer of carbon atoms arranged in a honeycomb lattice [24]. This unique structure led to a gapless, linear band dispersion with charge carriers behaving as massless Dirac fermions [24,25]. Many of graphene's spectacular transport and optical properties are a direct consequence of this unique band structure. In contrast to usual semiconductor systems with parabolic or non-parabolic dispersion, the absolute value of the electron velocity is a constant (Fermi velocity  $v_F = 10^6$  m/s) [24,25]. Assuming an incident monochromatic THz wave:

$$E_{THz}(t) = E_{THz} \cos \omega t \quad (3.1)$$

and neglecting the interband transition, a strongly anharmonic temporal current density will thus be generated:

$$J(t) \propto v_F \text{sign}[\sin \omega t] \quad (3.2)$$

Here, the nonlinear effects become important even at small fields and the generated square-wave-like current density will lead to the generation of odd order harmonics [26-28]. This is particularly interesting for applications in the THz frequency domain, because for doped graphene the interband transitions of THz photons are normally Pauli blocked. It has been theoretically predicted that graphene can be used as a natural THz frequency multiplier [26-28]. This was one of the most important motivations to study the nonlinear interaction of graphene with intense THz waves. In reality, on the other hand, due to the single-layer structure, the electronic property of

graphene can be strongly affected by the surrounding medium and various scattering effects [29-33]. The electron mobility of graphene at room temperature is only a few thousands  $\text{cm}^2/\text{Vs}$ , with an electron scattering time ranging from  $10^{-14} - 10^{-12}$  s. As shown in the following discussion, rather than the linear band dispersion, it is the carrier scattering effects that dominate the nonlinear THz responses at high electric fields.

Quantitatively, the electromagnetic responses of graphene can be described in terms of conductivity and separated into interband and intraband absorption. The intraband conductivity describes the intraband charge carrier dynamics and is normally described by a Drude response of a 2D massless Dirac system [34-41]:

$$\sigma_{intra}(\omega) = \frac{2e^2/\hbar^2}{\pi(1/\tau - i\omega)} k_B T_e \ln[2 \cosh(E_F/2k_B T_e)] = \frac{D}{1/\tau - i\omega} \quad (3.1)$$

Here,  $E_F$  is the Fermi-level energy,  $T_e$  is the electron temperature,  $\tau$  is the scattering time and  $D$  is the Drude weight. The interband conductivity, on the other hand, can be expressed by [42-44]:

$$\sigma_{inter}(\omega) = \frac{e^2}{8\hbar} \left[ \tanh\left(\frac{\hbar\omega + 2E_F}{4k_B T_e}\right) + \tanh\left(\frac{\hbar\omega - 2E_F}{4k_B T_e}\right) \right] \quad (3.2)$$

When  $\hbar\omega$  is higher than  $2E_F$  (without Pauli blocking), a universal absorption of  $e^2/4\hbar$  is obtained at room temperature for visible light. In practice, the graphene samples are normally doped with a certain Fermi energy ranging from approximately 100 meV up to 400 meV [45]. The minimum Fermi energy we have in our gated graphene samples is around 70 meV. As a result, the interband THz absorption is Pauli blocked and the THz conductivity can be fully described by Equation (3.1). The THz conductivity can then be tuned by changing either the Drude weight or the scattering time.

In the following two sections, we will first study the effect of environmental conditions on the carrier dynamics in graphene and then give a brief discussion on the nonlinear THz responses of gated monolayer graphene.

### **3.2 Ambient temperature effects on the carrier dynamics in graphene**

Our group has been studying the interaction of THz radiation with graphene since 2010. By performing nonlinear THz-TDS and optical-pump intense-THz-probe spectroscopy on highly doped epitaxial graphene with a fixed Fermi energy, Hafez *et al.* [39,46] have demonstrated that the combined effect of the optical pump and the THz electric field on the scattering times plays the largest role in defining the induced nonlinear carrier dynamics in monolayer graphene. Using gated graphene, Razavipour *et al.* [40] have demonstrated that the high-field THz responses of graphene are strongly Fermi energy dependent as well. The nonlinear THz response of graphene is found to be mainly dependent on the presence of free carriers and dominated by the increase in the scattering rate with increasing THz fields. Furthermore, at low Fermi energies, the differential THz transmission after target can be switched between positive and negative by changing the applied THz field strength, which paved the way to the development of optical switching applications [47].

For future technological applications, a thorough understanding of the stability of graphene under ambient environmental conditions is needed and crucial [41]. We then extended our investigations by employing THz-TDS as well as OPTP spectroscopy to study the effects of the ambient temperature on the optoelectronic properties of graphene. This work is in collaborations with Prof. Hiroki Hibino's group from NTT, Japan and Prof. Dignam's group from Queen's University (Kingston, Ontario).

In this experiment, we tested two types of large-scale monolayer graphene samples on the same 4H-SiC substrate, prepared by epitaxial growth methods from 4H-SiC and by transferring the chemical vapor deposited (CVD) graphene to a 4H-SiC substrate. The graphene samples are fabricated and characterized by the NTT group. The CVD graphene samples have shown high ( $\sim 10^{12} - 10^{13} \text{cm}^{-2}$ ) hole doping concentrations, while the epitaxial graphene samples have shown relatively low ( $\sim 10^{11} - 10^{12} \text{cm}^{-2}$ ) electron doping. We performed linear THz spectroscopy on the graphene samples in air at various temperatures ranging from room temperature up to  $300^\circ\text{C}$ . The sample under test is sandwiched in a specially designed sample holder with two aluminum plates with holes at the center and connected to a coil heater. The THz pulse is generated by optical rectification of 800 nm, 40 fs, Ti:Sapphire laser pulses in a  $\text{LiNbO}_3$  crystal using the pulse-front tilting technique [4]. In this study, the electric field is kept at minimum of approximately 1.5 kV/cm to avoid any nonlinear effects induced by intense THz electric field.

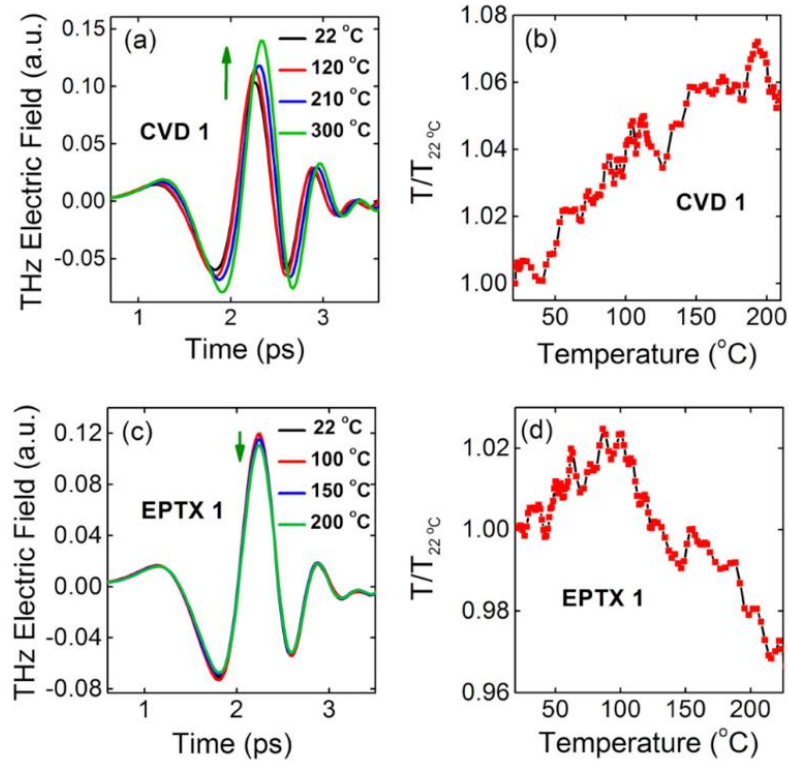


**Fig.3.1: THz-TDS measurements by changing the ambient temperature: the transmitted THz pulses (a) and (c) and the normalized peak field (b) and (d) for *p*-doped CVD graphene and *n*-doped epitaxial graphene. Adapted from [43].**

Fig. 3.1 (a) and (c) show the THz-TDS measurements by varying the ambient temperatures for CVD and epitaxial graphene. Fig.3.1. (b) and (d) show the corresponding THz peak transmission normalized to THz transmission of the sample at room temperature as a function of the sample temperature. Interestingly, the two graphene samples exhibit almost opposite behaviors as the temperature is increased. The THz transmission of the *p*-doped CVD graphene generally increases with increasing temperature, while the THz transmission of *n*-doped epitaxial graphene initially increases slightly but the general trend is a decrease in the transmission as the temperature increases.

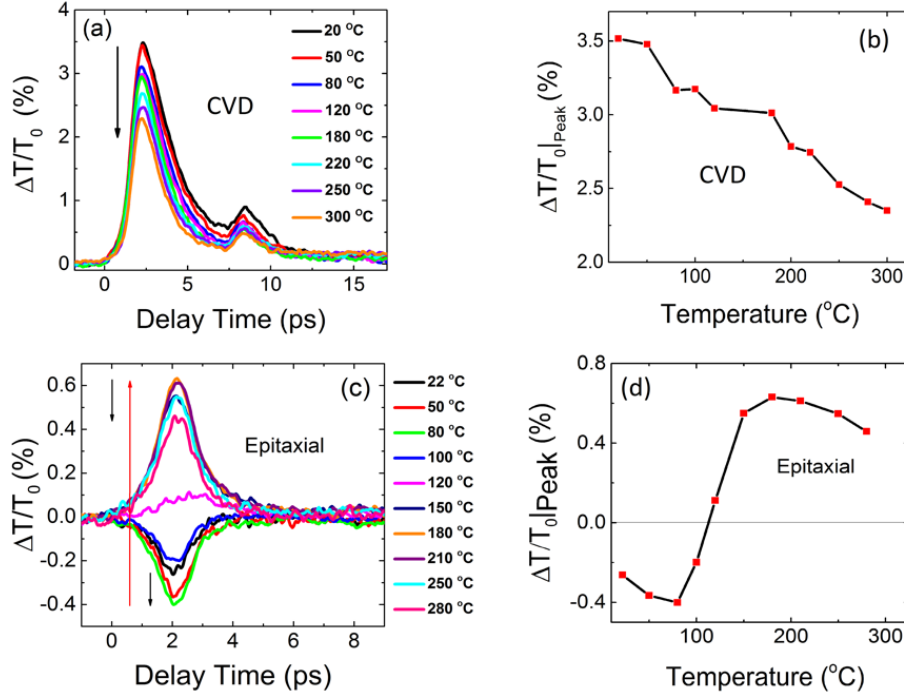


**Fig.3.2: Ambient temperature effects on the THz photoconductivity of graphene after photoexcitation:  $\Delta T/T_0$  as a function of the delay time between the optical pump and the THz probe beams for (a) *n*-doped epitaxial graphene, (c) *p*-doped CVD graphene, the black and red arrow indicate the reduction and enhancement of differential transmission by increasing the sample temperature; (b) and (d) are the corresponding peak of  $\Delta T/T_0$  as a function of the temperature for CVD graphene and epitaxial graphene. Adapted from [43].**

We then performed OPTP measurements to measure the temperature effects on the differential signals after photoexcitation by an 800 nm optical pump. Fig. 3.2 shows the OPTP response of the graphene samples defined by the THz differential transmission  $\Delta T/T_0$  after photoexcitation. For the highly *p*-doped CVD graphene sample, we observe a positive  $\Delta T/T_0$  at room temperature that decreases monotonically with increasing temperature (as represented by the black arrow), as shown in Figs. 3.2 (a) and 3.2 (b). The observed second peak of the differential signal in Fig. 3.2 (a) is due to the back reflection of the pump laser pulse from the substrate of the graphene sample.

On the other hand, the lightly *n*-doped epitaxial graphene shows a negative  $\Delta T/T_0$  at room temperature, which interestingly turns positive with increasing temperature, as shown in Fig. 3.2 (c) and 3.2 (d). These observations are analogous to those reported with gated graphene, in which the Fermi energy is changed by electrical gating [37,47,48]. Compared with non-doped semiconductor such as GaAs (Fig.2.9 (b)), graphene is a semi-metal and conductive at room temperature. When the Fermi energies are close to the charge neutral point, the additional carriers provided by the optical pump lead to a negative differential transmission signal, similar to normal semiconductors after photoexcitation. On the other hand, if the initial Fermi energy is already high, increased electron temperature due to photoexcitation may lead to a significant increase of scattering rate and in turn giving rise to a positive differential transmission after photoexcitation as shown here. This can be explained by the change of intraband conductivity as described in equation (3.1), in which the relative variations of the Drude weight and the scattering time determine the sign of the differential signal  $\Delta T/T_0$  after photoexcitation.

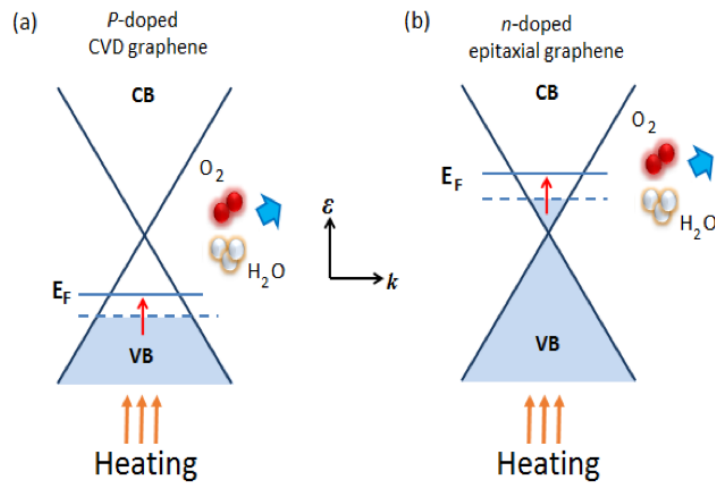


**Fig.3.3: Heating effect on the Fermi energy in (a) highly p-doped CVD graphene and (b) lightly n-doped epitaxial graphene. Adapted from [43].**

It has been reported in earlier studies that the desorption of air and oxygen molecules away from the surface of graphene can result in reduced hole doping (or equivalently increased electron doping) [29]. As a result, by heating, CVD graphene becomes less *p*-doped, while epitaxial graphene becomes more *n*-doped. We have confirmed this hypothesis by performing van der Pauw and Hall-effect measurements at temperatures comparable to those reported here, which have shown a dominant change of carrier density compared with the mobility change [41]. The highly *p*-doped CVD graphene with highly Fermi energy in the valence band exemplifying metal-like properties experienced an increase in the Fermi energy towards the charge neutral point without switching to the semiconductor-like regime, resulting only in a reduction in the positive  $\Delta T/T_0$ . In contrast to this, the crossover in the OPTP response of epitaxial graphene from a negative  $\Delta T/T_0$  to a positive  $\Delta T/T_0$  can be attributed to temperature-induced increase from a low Fermi energy in the conduction band exemplifying semiconductor-like properties, to higher Fermi energies exemplifying metal-like properties [37,41,47,48]. The Fermi energy thus exceeded a certain value that separates the two regimes when the sample is heated.

In summary, we have demonstrated that the linear THz responses are determined by the number of free charge carriers or the Fermi energy of graphene. The electronic properties of graphene are extremely sensitive to the sample temperature, which can tune the Fermi energy of graphene through desorption of water and oxygen molecules. This paves the way for using graphene in thermal switching and environmental sensing applications. However, this extreme sensitivity can also pose a great challenge in using graphene in many optoelectronic applications that require highly thermal stability.

### 3.3 Nonlinear terahertz time-domain spectroscopy of gated graphene

In 2013, in collaboration with Prof. Richard Martel's group at the University of Montreal, Hafez *et.al.* [40,47] designed a graphene device in the form of a field-effect-transistor, in which the carrier density can be controlled by electrochemical doping with a layer of ionic gel that is transparent in the THz frequency range. By controlling the Fermi-level energy, we can then study both the electric field and carrier density dependency of the nonlinear THz responses of graphene. For this sample, the minimum Fermi energy is 70 meV away from the CNP. Since the ionic gel is not homogeneously distributed on the graphene sample, the Fermi energy of graphene for the THz detection region is an average of the detection beam size.

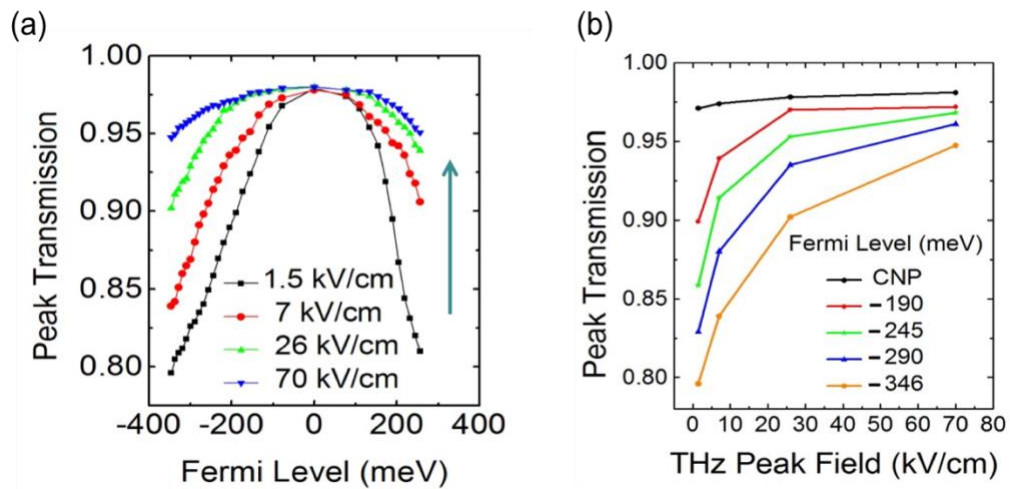


**Fig.3.4: Nonlinear THz-TDS of gated graphene: (a) THz peak transmission as a function of the Fermi energy for various THz field strengths. The arrow indicates the transmission enhancement with THz electric field for a certain Fermi energy. (b) Field-dependence of THz peak transmission at different Fermi energies.**

We measured the transmitted THz pulses through graphene and the graphene-free part of the sample and plotted the peak transmission as a function of the graphene Fermi energy at various field strengths. As can be seen from Fig. 3.4 (a), the peak transmission reaches the maximum value when the Fermi energy is close to the charge neutral point (CNP). Here, the carrier density is at its minimum and the maximum transmission is a result of the lowest THz conductivity due to the reduced Drude weight. On the other hand, as indicated by the arrow in Fig. 3.4. (a), increasing the THz field results in an increase in the THz transmission, which is more pronounced for graphene with higher doping. When the doping concentration is decreased, the relative increase in transmission with increasing THz field is less pronounced, indicating less nonlinear THz field effects. These observations emphasize that the nonlinear response of the graphene sample is mainly dependent on the presence of free carriers and can be explained by increased scattering when the THz field is increased.

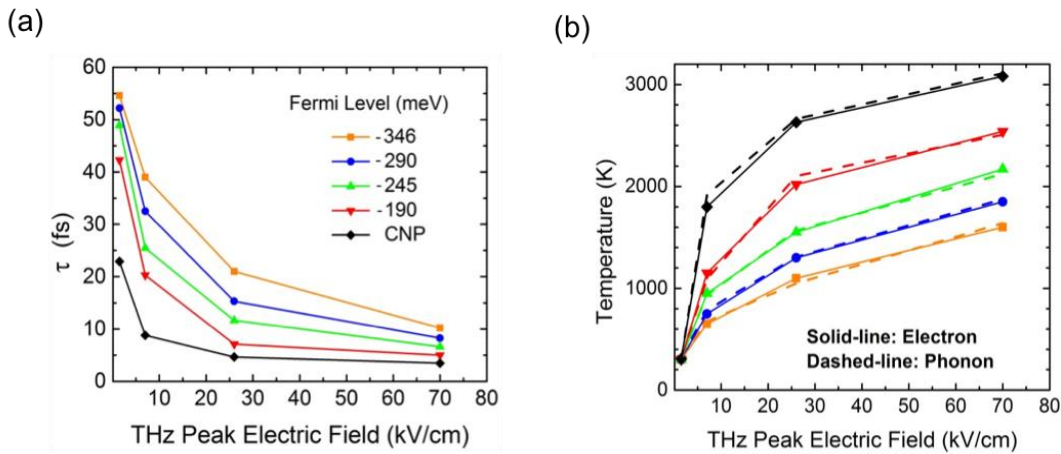


**Fig.3.5: The simulation results of the field-dependent scattering time as well as the electron temperature. Here, the phonon and electron temperatures are assumed to be identical for simplicity.**

To model the observed nonlinear effects, we account for intraband absorption using Equation (3.1) and take into account neutral ( $\tau_{sr}$ ) and charged impurity scattering ( $\tau_{Coul}$ ) as well as optical phonon scattering ( $\tau_{op}$ ) [39,40,46,47]. Two potential types of optical phonons can contribute to scattering: optical phonons in the graphene itself and polar surface phonons in the substrate. Due to the weak coupling strength, the scattering rate contribution from the surface phonons in the substrate materials is much smaller than those due to the graphene optical phonons [40]. As a results, here we only take into account the contributions from the optical phonons in graphene. The scattering time  $\tau$  is expressed as:

$$\begin{aligned} \frac{1}{\tau} &= \frac{1}{\tau_{Coul}} + \frac{1}{\tau_{sr}} + \frac{1}{\tau_{op}} \\ &= \frac{C_1}{E_{eff}} + C_2 \varepsilon_k + \frac{D_0^2}{2\hbar^2 v_F^2 \sigma_m \omega_0} \frac{\varepsilon_k + \hbar\omega_0}{e^{\hbar\omega_0/k_B T} - 1} \end{aligned} \quad (3.3)$$

where  $C_1$  ( $3.63 \text{ ps}^{-1}\text{eV}$ ) and  $C_2$  ( $30 \text{ ps}^{-1}\text{eV}$ ) are constants that depend on the density of the charged and neutral impurities, respectively.  $E_{eff}$  is the effective Fermi energy for a given electron temperature,  $\varepsilon_k$  is the average carrier kinetic energy driven by the THz field,  $\hbar\omega_0 = 147 \text{ meV}$  is the optical phonon energy,  $D_0 = 5 \times 10^9 \text{ eV/cm}$  is the deformation potential for the zone-edge optical phonons,  $\sigma_m = 7.6 \times 10^{-8} \text{ g/cm}^2$  is the 2D mass density of graphene,  $k_B$  is the Boltzmann constant and  $T$  is the phonon temperature that serves as a fitting parameter for the calculation of the scattering time as shown in Fig. 3.5 (a). High-field THz pulses lead to strong carrier heating and in turn reduce the total scattering time as well as the THz absorption.

In conclusion, we observed a strong increase in the THz transmission with increasing field. This transmission enhancement appears to result from a decrease in the carrier scattering time with increasing electric field. Higher field-induced THz transmission modulation range was observed for graphene with a high Fermi energy. As demonstrated by the ambient temperature effect as well

as the gating effect, the number of carriers that interact with the THz pulses are important for both low- and high-field responses. In addition, by performing OPTP measurements, we have observed a crossover from semiconductor-like to metal-like behavior by increasing the Fermi energy of graphene. The change of the Fermi energy can be realized by changing the ambient temperature of graphene or by control the gate-voltage of the gated graphene. The nonlinear THz responses are similar for both CVD and epitaxial graphene, in which the Fermi energy as well as the scattering rate determines the corresponding nonlinear THz conductivity.

It is worth mentioning that due to the strong carrier scattering effect, we did not observe any signature of THz coherent harmonic generation due to the linear band dispersion. However, another question is also raised here because we didn't actually lose the nonlinearity. The scattering effect itself takes place during each half-cycle acceleration, resulting in a nonlinear variation of the THz conductivity. In the following sections, we will discuss nonlinear terahertz optics induced by intraband carrier dynamics as well as the importance to take into account the temporal variation of the THz conductivity.

## Chapter 4

### Nonlinear terahertz optics induced by intraband carrier dynamics

Nonlinear optics refers to the nonlinear behavior of light in a medium, in which the dielectric polarization responds nonlinearly to the electric field of the incident light [49]. For THz-driven free charge carrier dynamics in graphene or in common doped semiconductors [39,40,46,50-53], we use the THz conductivity of the material to describe the corresponding response to the THz electric field. Analogously, for a centrosymmetric system, the nonlinear variation of THz conductivity should have led to the generation of odd-order harmonics. On the other hand, even-order harmonics could be observed in a noncentrosymmetric system. In the following, we will discuss three possible intraband approaches that can be used for nonlinear THz optics.

#### 4.1 Nonlinear THz intraband conductivity

##### 4.1.1 Nonparabolic band dispersion

As discussed in Chapter 3.1, the initial motivation to perform nonlinear THz spectroscopy on graphene was due to its unique linear band dispersion, which should have led to the generation of harmonics even at relatively low fields. In fact, similar effects exist for common semiconductors as well. When an electron occupies higher energy levels in the conduction band, the energy-momentum dispersion deviates from a parabolic dispersion [54]. As a result, the carrier will no longer respond harmonically to the driving field, giving rise to a nonlinear response that may lead

to HHG. Here, the nonlinearity is naturally induced by the material itself and carrier oscillation in a single valley of the conduction band is enough to observe nonlinear effects such as harmonic generation.

In general, a nonparabolicity parameter can be used to calculate the energy-dependent electron effective mass variation, giving rise to an increase of the carrier effective mass during acceleration. For example, in the central  $\Gamma$  valley, the nonparabolicity factor of  $\text{In}_{0.53}\text{Ga}_{0.47}\text{As}$  is  $1.33 \text{ eV}^{-1}$  and for semiconductor  $\text{InSb}$ , the corresponding factor is as high as  $4.1 \text{ eV}^{-1}$ . Very recently, by using a free electron laser at 4 THz, third harmonic generation has been observed in  $\text{InSb}$  and the corresponding results are attributed to the highly nonparabolic band dispersion [55].

#### **4.1.2 Intraband Bloch oscillation**

When the laser field is sufficiently intense for the carrier momentum to reach the edge of the Brillouin zone, Bragg reflection then takes place and the electrons will perform Bloch oscillations [56-58]. Here, the number of oscillations within one half-cycle increases with the driving laser field [56,57]. This is a long-standing prediction by Bloch and Zener and has recently been demonstrated using mid-IR and multi-THz pulses [56,57]. Experimentally, Bloch oscillations has led to the observation of high harmonic generation (HHG) [56,57,59-63].

For the observation of such effect, extremely intense field ( $72 \text{ MV/cm}$  in [56,57]) and high speed acceleration (30 THz) is needed in order to drive the carriers to the edge of the Brillouin zone before scattering takes place. In the conventional THz window, due to the relatively low field (hundreds of  $\text{kV/cm}$ ) as well as the slowly varying electric field (1 THz), scattering effects may eventually dominate the nonlinear responses [57,64].

### 4.1.3 Carrier scattering: limitation of the Drude model

Both nonparabolic band dispersion and the Bloch oscillations are coherent effects and can be induced by coherent intraband carrier motion. On the other hand, coherence will be vanished if scattering effect takes place. However, as we discussed earlier, nonlinear THz response is determined by the THz conductivity. A coherent subcycle nonlinear conductivity should lead to the observation of nonlinear effects such as harmonic generation. Various scattering effects dominate the high field responses of graphene, giving rise to a transmission enhancement by increasing the incident THz electric field. Here, it is clear that the charge carriers in graphene won't respond harmonically to the driving THz field. Furthermore, since the direction of carrier motion always synchronizes with the driving THz waveform and the carrier heating (or conductivity reduction) takes place within each half-cycle pulse, a nonlinear current density should be generated, which could eventually emit harmonics.

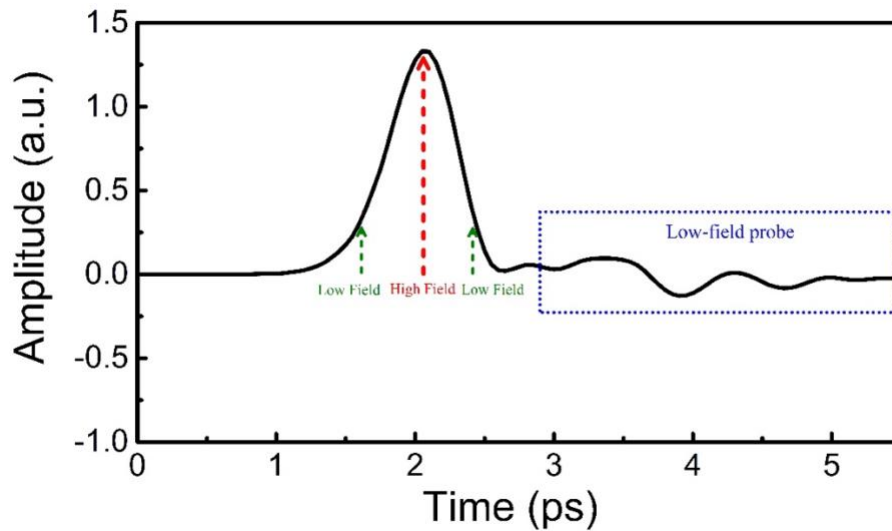


**Fig.4.1:** THz temporal profile of a half-cycle THz pulse generated from iLAPCA, where the THz field strength varies continuously.

To understand such subcycle variation of THz conductivity, the temporal dynamics must be taken into account. For the conventional Drude model of common semiconductors, the free carrier dynamics in the time domain can be described by an equation of motion [5]:

$$\frac{dv(t)}{dt} = \frac{eE(t)}{m_e} - \frac{v(t)}{\tau} \quad (4.1)$$

Here,  $\tau$  is the scattering time that normally serves as a single relaxation parameter. For an incident pulse with a certain field, the scattering time as well as the carrier effective mass  $m_e$  are kept constant and therefore the temporal nonlinearities cannot be revealed directly. As illustrated in Fig. 4.1, within one half-cycle, the THz electric field changes continuously from low field, to high field and then to low field. Hence, the total scattering time  $\tau$  as well as the carrier effective mass  $m_e$  should be time-dependent as well. Equation (4.1) can thus be written as the following for modelling the subcycle nonlinear carrier dynamics:

$$\frac{dv(t)}{dt} = \frac{eE(t)}{m_e(t)} - \frac{v(t)}{\tau(t)} \quad (4.2)$$

It is clear that the resulting THz conductivity varies along the whole temporal waveform, leading to the generation of a nonlinear current density that could emit harmonics in the THz frequency domain.

## 4.2 Intuition of subcycle nonlinear THz optics induced by carrier scattering

In practice, such subcycle nonlinear effects had not been observed very clearly in the time domain on monolayer graphene or in other common semiconductors materials such as doped  $\text{In}_{0.53}\text{Ga}_{0.47}\text{As}$  thin conducting film or photoexcited GaAs [50,51,65]. A distorted current density

caused by the scattering effect should have changed the transmitted THz waveform. For graphene, the increased carrier temperature leads to an increase of the scattering rate and in turn alters the THz temporal conductivity along the THz waveform. For polar semiconductors such as  $\text{In}_{0.53}\text{Ga}_{0.47}\text{As}$  or GaAs, on the other hand, the high field responses are dominated by the intervalley scattering effect, which redistributes the carrier effective mass as well as the momentum by scattering carriers from the central valley to the side valleys. The intervalley scattering rate is energy-dependent and a Drude model incorporating the dynamic intervalley-electron-transfer has been used to simulate the THz responses [50,51,65]. In this model, the intervalley scattering rate is calculated by the electron energy with a seventh-order polynomial function [50,51,65]. The temporal dynamics are thus taken into account here to calculate the energy-dependent intervalley scattering rate.

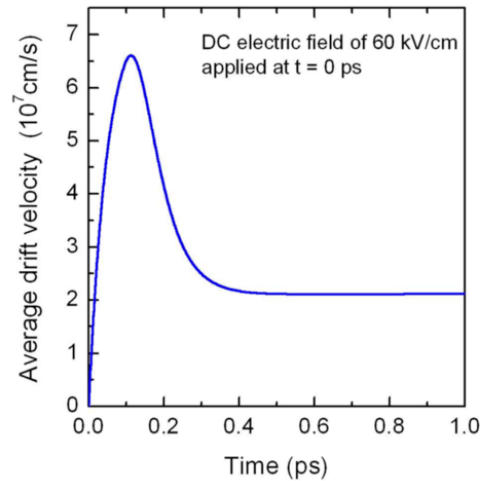


**Fig.4.2: Time evolution of the average electron drift velocity upon the application of a step-like electric field of 60 kV/cm according to the dynamic intervalley-electron-transfer model. Adapted from [51].**

As shown in Fig. 4.2, for a step-like DC field, the simulated average drift velocity signal is strongly nonlinear, which shows an acceleration followed by a rapid reduction, and become constant afterwards. By using THz pulses generated from a ZnTe nonlinear crystal via optical rectification, Razzari *et al.* [50] has observed a transmission enhancement by increasing the THz electric field. In this work, the nonlinear transmission enhancement did not lead to a clear observation of harmonic generation or high frequency generation. However, if a nonlinear current density, such as the one shown in Fig.4.2, can be generated within one half-cycle, a clear change in the transmitted THz spectra should have be observed.

In fact, this controversy can be explained intuitively by comparing the time scale of the THz pulses versus that of the temporal current density shown in Fig. 4.2. Here, the half-cycle duration before the signal become constant is approximately 300 fs, which is comparable to the half-cycle duration of the THz pulses generated from ZnTe (centered at 1 THz) or that from LiNbO<sub>3</sub> THz source (centered at 0.75 THz). Hence, a longer half-cycle duration, that can confine the subcycle nonlinearities more efficiently, could be more favorable to observe such subcycle nonlinear effects.

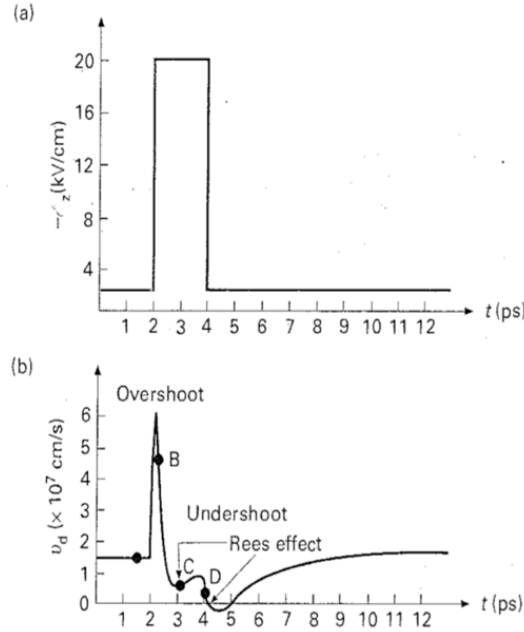


**Fig.4.3: Monte-Carlo simulation of carrier transport driven by a square-wave like electric field . (a) Applied transient electric field in time. (b) Calculated average drift velocity versus time for electrons in GaAs at room temperature. Adapted from [66].**

In fact, similar transient effect has been predicted using the more precise Monte-Carlo simulation approach. As shown in Fig. 4.3, a square electric field with a duration of 2 ps was applied on a doped semiconductor GaAs and the resulting average carrier velocity has shown a similar trend as the dynamic intervalley-electron-transfer model. (Fig. 4.2). If we compare the velocity waveform here, the pulse duration at full-width at the half-maximum (FWHM) amplitude is approximately 300 fs, which is too short for a clear observation of subcycle nonlinear THz optics using high frequency THz pulses (ZnTe or LiNbO<sub>3</sub>). A longer half-cycle pulse is thus needed here to provide a higher temporal contrast similar to the square electric field used in the simulation here. A low central frequency THz pulses are therefore required, which can be realized with our iLAPCA THz source.

For nonlinearities induced by scattering, there is no fundamental difference between graphene and common semiconductors. Increased scattering rate leads to a decrease of the THz conductivity. However, we need higher modulation or contrast between high and low fields to obtain a clear experimental observation by using a half-cycle THz pulse generated by iLAPCA. In one half-cycle pulse, this effect is much stronger for polar semiconductor materials that possess a high-mobility central valley and extremely low mobilities at upper valleys.

It is worth noting that very recently, Hafez *et al.* [67] has observed HHG from monolayer graphene using an extremely narrow-band (centered at 0.3 THz) multi-cycle THz pulses generated from a superconducting radiofrequency accelerator-based superradiant THz source. The observations were attributed to the nonlinear variation of the THz conductivity due to carrier heating.

### 4.3 Ensemble Monte-Carlo approach

To model the temporal carrier dynamics of semiconductor  $\text{In}_{0.53}\text{Ga}_{0.47}\text{As}$ , we adapted a more complete approach: the ensemble Monte-Carlo model. The Monte-Carlo technique has been used for over 30 years as a numerical method to simulate the nonequilibrium transport in semiconductor materials. In a Monte-Carlo simulation, the carrier dynamics are assumed to consist of free flights terminated by instantaneous scattering events. After each scattering event, the energy  $\varepsilon_{\mathbf{k}}$  and the momentum  $\mathbf{k}$  are changed according to the specific scattering mechanism. To account for the transient dynamics, we take into account the dynamics of an ensemble of carriers in the simulation.

To calculate intraband current density  $J(t)$ , we perform a theoretical analysis using an analytical-band ensemble Monte-Carlo approach incorporating the carrier dynamics in the  $\Gamma$ , L and X valleys of the conduction band [54,68,69]. Four equivalent L valleys and three equivalent

X valleys are considered in this model. The energy separation between the L valleys and the  $\Gamma$  valley is 0.55 eV, and that between the X valleys and the  $\Gamma$  valley is 0.67 eV [70]. The physical constants used in the simulation are summarized in Table I [50,70]:

**TABLE I**

<b>Physical constant</b>	<b><math>\Gamma</math> valley</b>	<b>L valleys</b>	<b>X valleys</b>
Number of valleys	1	4	3
Effective mass ratio	0.041	0.26	0.54
Nonparabolicity factor (eV) <sup>-1</sup>	1.33	0.59	0.65
Longitudinal polar optic phonon energy (eV)	0.00345	0.00345	0.00345
Transverse polar optic phonon energy (eV)	0.00312	0.00312	0.00312
Acoustic phonon deformation potential (eV/cm)	9.2	9.2	9.2
Intervalley deformation potential (eV/cm)			
From $\Gamma$	0.0	$7.0 \times 10^8$	$7.0 \times 10^8$
From L	$7.0 \times 10^8$	$7.0 \times 10^8$	$5.0 \times 10^8$
From X	$7.0 \times 10^8$	$5.0 \times 10^8$	$5.8 \times 10^8$
Intervalley phonon energy (eV)			
From $\Gamma$	0.0	$2.276 \times 10^{-2}$	$2.38 \times 10^{-2}$
From L	$2.384 \times 10^{-2}$	$2.312 \times 10^{-2}$	$2.69 \times 10^{-2}$
From X	$2.276 \times 10^{-2}$	$2.696 \times 10^{-2}$	$2.27 \times 10^{-2}$

For a single electron, we simulate its free acceleration interrupted by different scattering events. Then we repeat the process for each particle in the ensemble until the simulation is completed for each fixed time interval  $\Delta t$ . This  $\Delta t$  is used to synchronize the movement of all the carriers. Within

each  $\Delta t$ , the simulation of each carrier is independent of other carriers and it consists of several free flight time intervals interrupted by scattering effects.

Within each time interval of free flight, the movement of each electron is described by the Bloch theorem:

$$\hbar d\mathbf{k}/dt = -e\mathbf{E}_{THz} \quad (4.3)$$

Here,  $\mathbf{k}$  is the electron wavevector and the corresponding velocity in real space is then given by:

$$\mathbf{v} = \hbar^{-1} \frac{d\varepsilon_{\mathbf{k}}}{d\mathbf{k}} \quad (4.4)$$

where  $\varepsilon_{\mathbf{k}}$  is the electron energy. At high energies, the non-parabolic effects on the band dispersion are taken into account as well with:

$$\varepsilon_{\mathbf{k}}(1 + \alpha\varepsilon_{\mathbf{k}}) = \frac{\hbar^2 \mathbf{k}^2}{2m^*} \quad (4.5)$$

Here, we used a non-parabolic factor of  $\alpha = 1.33, 0.59$  and  $0.65 \text{ eV}^{-1}$  for  $\Gamma, L$  and  $X$  valleys, respectively. The effective mass ratio  $m^*$  is  $0.041, 0.26$  and  $0.54$  at the bottom of valley  $\Gamma, L$  and  $X$ .

To account for different scattering effects, we take into account typical scattering mechanisms in compound semiconductor such as polar optical phonon scattering, acoustic scattering, Coulomb scattering as well as intervalley scattering [54,69]. Here, all the scattering rates are calculated according to the Fermi's Golden Rule [54,69]. Fig. 4.4 shows the calculated intervalley scattering rates for different valleys.

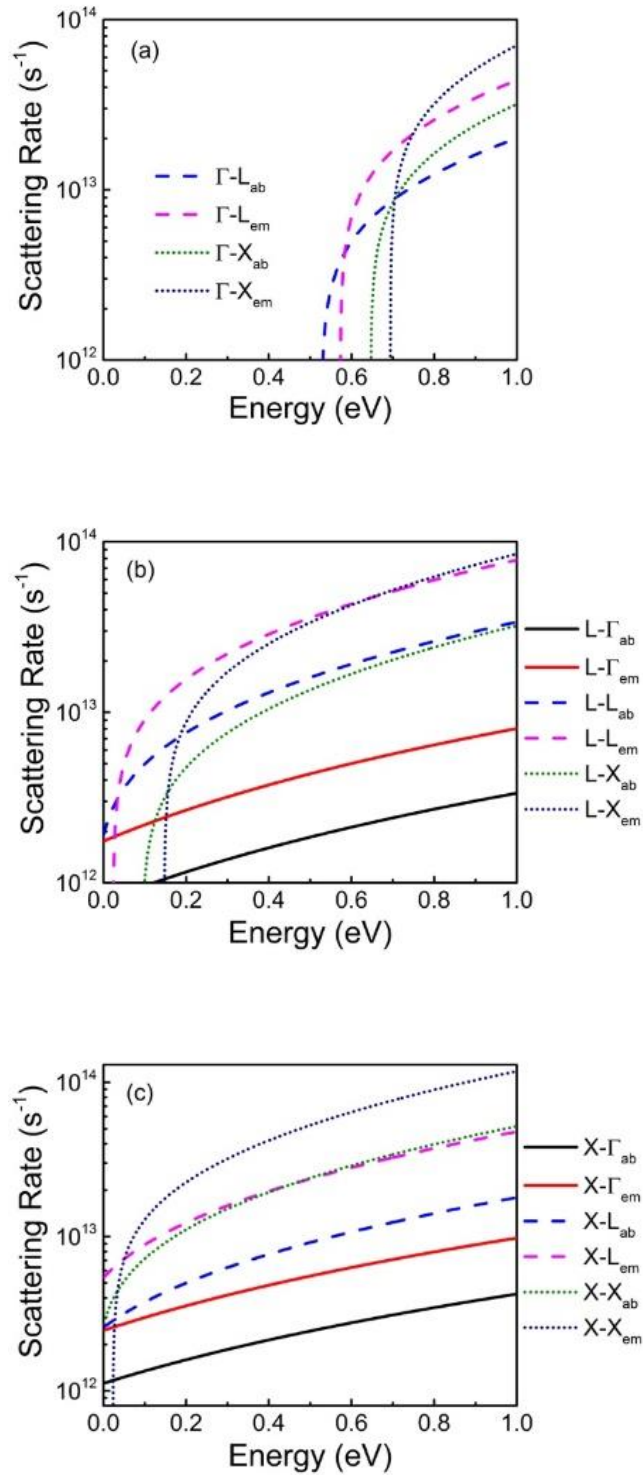


**Fig.4.4: Intervalley scattering rates by absorption (ab) and emission (em) of phonons. (a)  $\Gamma$ -valley, (b) L valleys, (c) X valleys. The 0 eV energy corresponds to the bottom of each valley.**

For inelastic scattering process, the energy is varied by emission or absorption of phonons. The anisotropic and isotropic processes are treated differently within a spherical coordinate system for the rotation of  $\mathbf{k}$ . For example, acoustic phonon and intervalley scattering are isotropic scattering processes. After each scattering, the polar angle  $\theta$  as well as the azimuthal angle  $\varphi$  of the electron are calculated by [54,69]:

$$\cos \theta = 1 - 2r \quad (4.6)$$

$$\varphi = 2\pi r \quad (4.7)$$

Here,  $r$  is generated randomly between 0 and 1. On the other hand, Coulomb scattering and polar optical phonon scattering are anisotropic processes. We calculate the polar angle after polar optical phonon scattering for parabolic bands in a rotated coordinate system by [54,69]:

$$\cos \theta = \frac{(1+\xi)-(1+2\xi)^r}{\xi} \quad (4.8)$$

$$\xi = \frac{2\sqrt{\varepsilon_{\mathbf{k}}(\varepsilon_{\mathbf{k}} \pm \hbar\omega_{polar})}}{(\sqrt{\varepsilon_{\mathbf{k}}} + \sqrt{\varepsilon_{\mathbf{k}} \pm \hbar\omega_{polar}})^2} \quad (4.9)$$

Here,  $\hbar\omega_{polar}$  is the polar optical phonon energy. The final angle after ionized impurities (Coulomb scattering) is described by [54,69]:

$$\cos \theta = 1 - \frac{2r}{1+4k^2L_D^2(1-r)} \quad (4.10)$$

where  $L_D$  is the Debye screening length. The azimuthal angle for both scattering processes is calculated using equation (4.8).

In conclusion, we have introduced several intraband mechanisms that can be used to induce subcycle nonlinear THz optics. In particular, it is important to take into account carefully the temporal carrier dynamics and their effect on the transmitted THz waveforms. In addition, we have introduced the ensemble Monte-Carlo method, which can provide a much more complete picture of the transient carrier dynamics in semiconductor materials. In the following discussion of subcycle nonlinear THz optics, we use this approach to perform the theoretical simulation of nonlinear THz responses of the  $n$ -doped  $\text{In}_{0.53}\text{Ga}_{0.47}\text{As}$  semiconductor thin layer.

## Chapter 5

### Subcycle nonlinear terahertz optics

*This chapter is written based on:*

*Chai, Xin, Xavier Ropagnol, S. Mohsen Raeis-Zadeh, Matthew Reid, Safieddin Safavi-Naeini, and Tsuneyuki Ozaki. "Subcycle Terahertz Nonlinear Optics." Physical Review Letters 121, no. 14 (2018): 143901.*

*with the Reuse and Permission License from American Physical Society.*

To reach the regime of subcycle nonlinear optics, we used the iLAPCA based THz source. The generated half-cycle duration extends to 580 fs (amplitude full-width at half-maximum (FWHM)). With such long acceleration, we can tune the light-matter coupling from linear to nonlinear and turn on the THz waveform reshaping within a single half-cycle. The electric field of the radiated THz pulse is controlled by varying the bias voltage on the antenna, which induces only very small distortions on the emitted THz pulse waveforms. The sample under study was positioned carefully at the THz focus for high-field transmission measurements at normal incidence and the transmitted electric field of the THz pulse is measured via electro-optic sampling in a 300  $\mu\text{m}$  (110)-cut GaP crystal. Our InGaAs sample (MTI Corp.) consists of a 500-nm-thick n-type  $\text{In}_{0.53}\text{Ga}_{0.47}\text{As}$  (100) epilayer with a doping concentration of approximately  $2 \times 10^{18} \text{ cm}^{-3}$ . Since the current density is linearly proportional to the carrier density, higher doping concentration can provide a higher amplitude contrast or modulation between the low-field and high-field responses, as demonstrated

by the THz-TDS measurements of the gated graphene. However, at much higher doping concentration above around the order of  $10^{19}$   $\text{cm}^{-3}$ , the thin film semiconductor becomes degenerate and behaves like a metal, which can strongly reduce the transmitted THz energy as well. The InGaAs thin film is grown by metal-oxide chemical vapor deposition on a lattice matched, 0.35 mm thick semi-insulating InP substrate. The InP substrate has shown an overall THz Fresnel transmission of 0.7 and nonlinear effects are not observed when the experiment is carried out on a bare substrate.

## 5.1 Half-cycle nonlinear terahertz optics

Fig. 5.1 (a) shows the transmitted THz waveforms through the bare substrate ( $E_{ref}$ ) and semiconductor sample ( $E_{trans}$ ) when the incident peak field is at 190 kV/cm. We observed high frequency generation (HFG) with spectral amplitude enhancement from approximately 1 THz up to 2.5 THz. In the time domain [inset of Fig. 1(a)], a clear truncation of the half-cycle pulse is shown, where the front part of the incident half-cycle has been chopped after transmission through the sample.

To study the nonlinear effect, we varied the incident THz peak field  $E_{in}$  from 31 kV/cm to 190 kV/cm. Fig. 5.1(b) plots the transmitted THz peak fields and the half-cycle durations as a function of the incident field. The sample has shown linear transmission at low fields, while strong nonlinear transmission enhancement is observed at high fields. Meanwhile, the half-cycle duration maintains above 500 fs at low fields and decreases rapidly when the field is above 129 kV/cm, where transmissions greater than unity have been observed at high frequencies [Fig. 5.1(c)]. As

can be seen from Fig. 5.1 (c), the region of spectral amplitude enhancement enlarges with field and covers the spectral range above 1 THz.

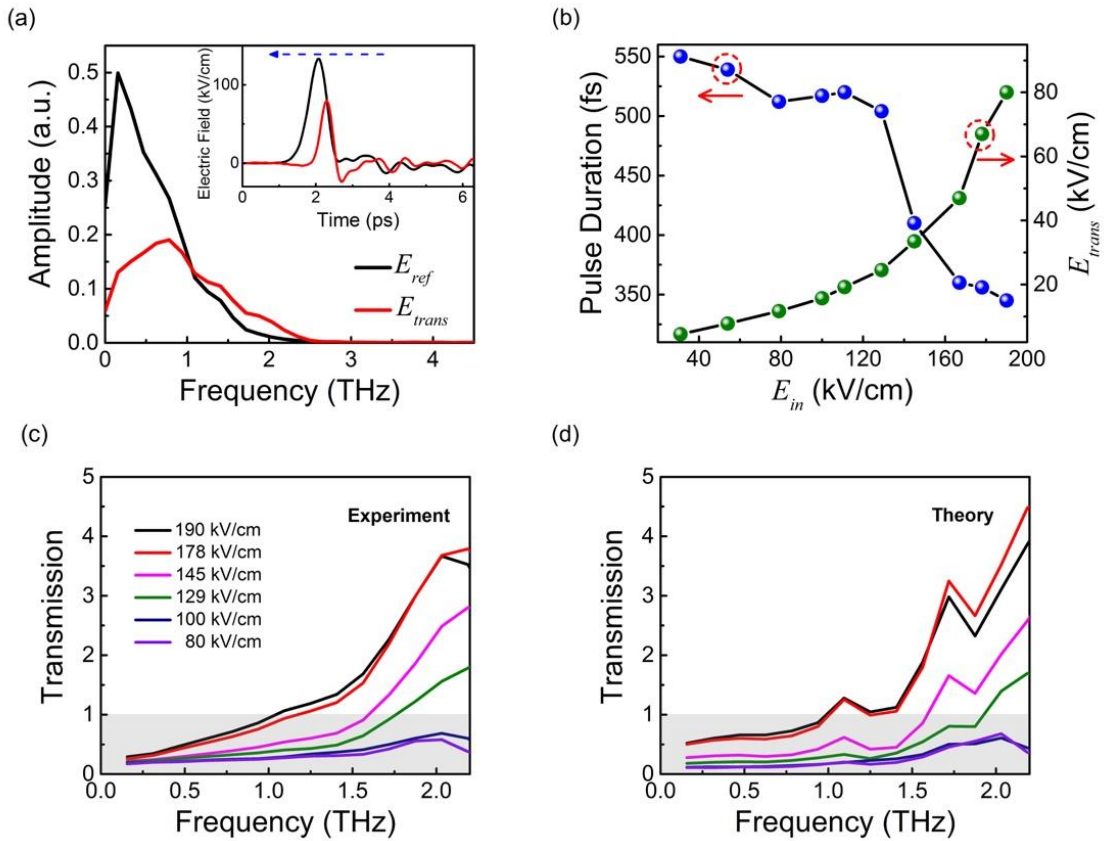


**Fig.5.1:** (a) Amplitude spectra of the transmitted THz pulses through the bare substrate ( $E_{ref}$ ) and the InGaAs sample ( $E_{trans}$ ) with the incident peak field of 190 kV/cm. Inset: corresponding THz waveforms, where the blue arrow indicates the propagation direction. (b) Measured field dependence of  $E_{trans}$  and half-cycle duration (amplitude FWHM) as a function of the incident peak field  $E_{in}$  measured in air. (c) Measured transmission spectra at various incident fields. The gray area corresponds to the transmission lower than 1. (d) Calculated transmission spectra based on the described model.

To understand the subcycle nonlinear carrier dynamics, we performed theoretical analysis in the time domain by using the thin-film transmission equation (Equation 2.20). We rewrite the equation here for clarity:

$$E_{trans}(t) = \frac{1}{Y_0 + Y_S} \left( \frac{4Y_S}{N+1} E_{in}(t) - J(t)d \right)$$

Here,  $d = 500 \text{ nm}$  is the thickness of the sample.  $Y_0 = (377 \Omega)^{-1}$  is the free-space admittance and  $Y_S = NY_0$  is the admittance of the substrate, in which  $N = 3.1$  is the refractive index of InP [50]. In the thin film regime, all the carriers are assumed to experience the same driving field  $E_{trans}$ , which is measured at 80 kV/cm when the incident peak field is at 190 kV/cm. As apparent from this linear relation between the current density and the emitted field, an ultrafast nonlinear distortion on a periodic current density  $J(t)$  should contain high-order harmonics of the driving frequency and a continuous high frequency band could be generated when broadband subcycle pulses are used. This is the fundamental difference of the harmonic spectra between the broadband subcycle pulses and narrowband multi-cycle pulses. To characterize the transient carrier dynamics, we used the analytical-band ensemble Monte-Carlo approach as a solution of the Boltzmann transport equation as described in Chapter 4.3. In contrast to HHG driven by mid-infrared laser pulse [56,57], the ballistic motion can be largely suppressed at high energies due to the relatively weak but slow-varying field in the picosecond range ( $\omega_{0.15 \text{ THz}}^{-1} \approx 1.07 \text{ ps}$ )[57,71]. The dynamics of each carrier in the ensemble were simulated simultaneously and  $J(t)$  was determined by the average drift velocity.

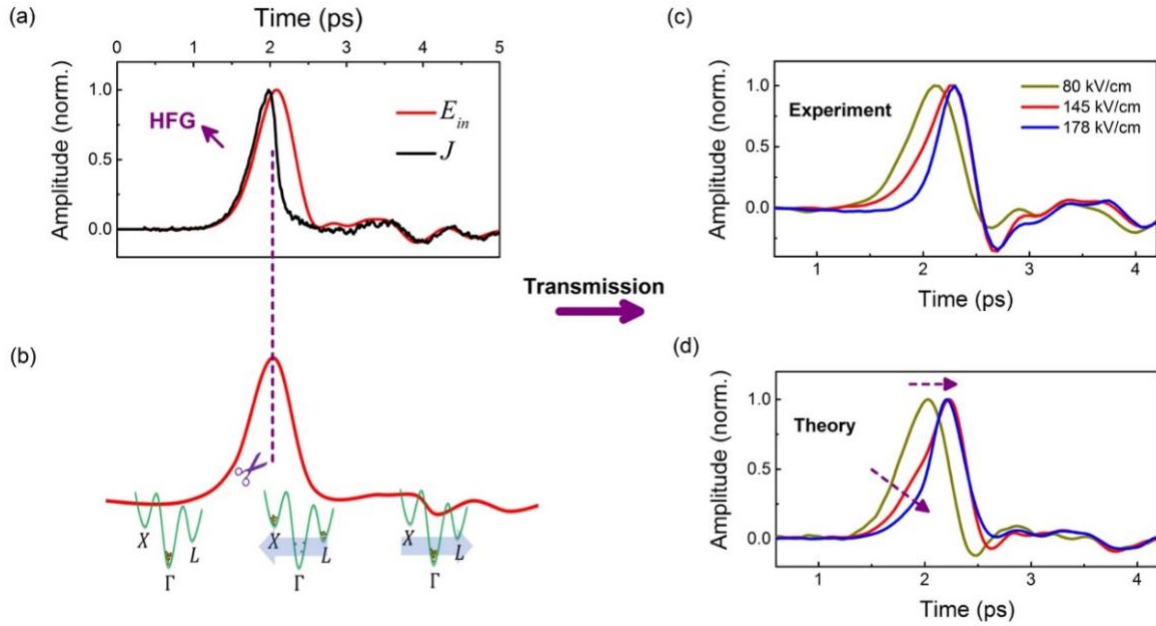


**Fig.5.2: (a) Incident THz waveform and the calculated current density with the field strength of 190 kV/cm. (b) Schematic of the experiment in momentum space: intense THz transient induces carrier intervalley scattering. The increased field strength leads to a damping of the subcycle current density (or a current density cut) and an increase in the total relaxation time. (c) Impact of current drop on the transmitted THz waveforms of three tested field strengths shown in Fig. 5.1. The transmitted waveforms are normalized by the corresponding peak values. (d) Normalized transmitted THz waves obtained from calculation.**

Fig. 5.1 (d) shows the calculated THz transmissions for various field strengths. A continuous high frequency band is generated due to the subcycle current drop as shown in Fig. 5.2. This rapid drop in current density further causes a temporal shift of the transmitted THz peak. Here, all the THz pulses are measured from the same starting time. At high fields, the rear part of the half-cycle experiences a much lower conductivity and in turn pushes the THz peak backwards in time. This can be understood as a huge reduction of the current density  $J(t)$  within one half-cycle using Equation 5.1, higher  $E_{trans}(t)$  is expected for the rear part of the half-cycle pulse. These

observations are reproduced accurately by our time-domain analysis, in which a rapid crossover from drift energy to thermal energy dominant carrier motions takes place within the half-cycle pulse [72].

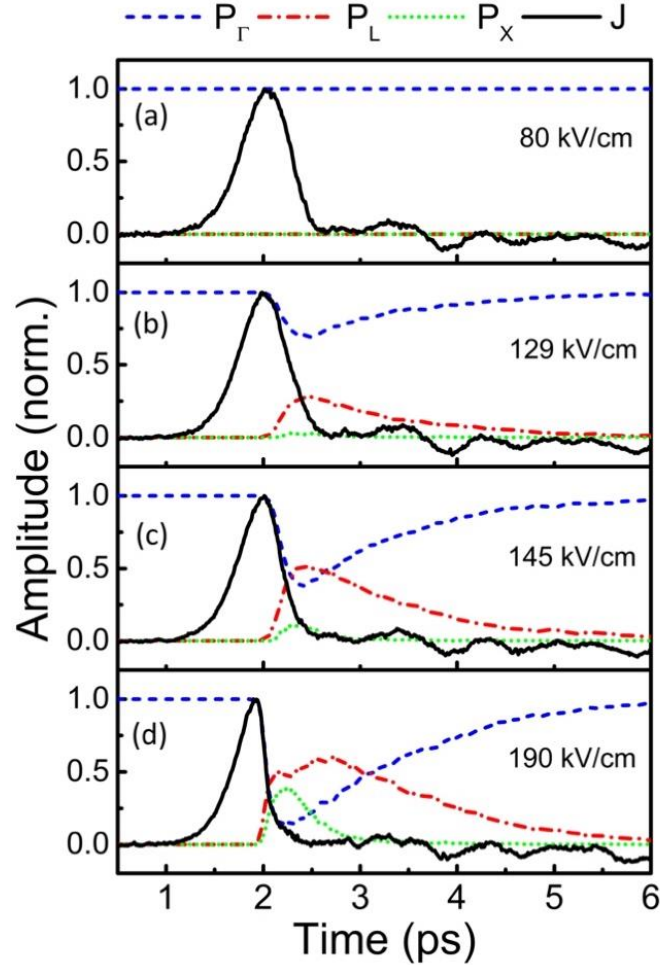


**Fig.5.3:** Calculated normalized temporal current density (black solid lines), and carrier populations in the  $\Gamma$ , L and X valleys at various fields of (a) 80 kV/cm, (b) 129 kV/cm, (c) 145 kV/cm and (d) 190 kV/cm, respectively (ensemble Monte-Carlo simulation). Due to strong intervalley scattering rates, some statistical fluctuations are shown on the normalized current density.

Here, we will discuss the subcycle carrier dynamics in detail obtained from the ensemble Monte-Carlo simulation. At low (80 kV/cm) THz electric fields, carriers remain in the  $\Gamma$  valley and basically follow the incident THz temporal profile [Fig. 5.3 (a)]. As the incident field starts to increase, carriers acquire more kinetic energy, and intervalley transitions from the  $\Gamma$  valley to the L valleys take place, giving rise to THz absorption bleaching [Fig. 5.3 (b)]. However, this process has shown dynamic features on a time scale slightly longer than the THz pulse duration. Consequently, the temporal current profile remains approximately identical to that at lower fields. On the other hand, by further increasing the applied field to 145 kV/cm, significant nonlinear processes take place where a clear pulse shortening is observed in the temporal current waveform [Fig. 5.3 (c)]. At this field, the ponderomotive acceleration is strong enough to cause intervalley scattering effects between the  $\Gamma$ , L and X valleys. Intense THz transient provides sufficient energy to the carriers and enables intervalley scattering from the  $\Gamma$  and L valleys to X valleys and cause carrier scattering between equivalent X and L valleys as well. At the highest field of 190 kV/cm, a small drop of the  $P_L$  is shown as the  $P_X$  approaches its maximum, indicating that the carriers can be further scattered to the X valleys as long as the THz field remains intense [Fig. 5.3 (d)]. The FWHM of the half-cycle pulse of current density decreases from 570 fs at low fields down to around 360 fs at high field. As the time-scale of the conductivity suppression becomes much shorter than the original THz pulse duration, high-frequency components are generated in the current density as well as the transmitted field.

## **5.2 Adding another half-cycle pulse with opposite polarity**

For coherent intraband Bloch oscillation, charge carriers perform several oscillations during every half-cycle of the laser and emit high-order harmonics [56,57]. Here, the drop of current density due to scattering causes a truncation of the half-cycle pulse and in turn increases the bandwidth of the transmitted pulse. However, the scattered hot carriers in the upper valleys possess much longer relaxation time [50,51,73]. Hence, the next half-cycle should display a nontrivial dependence on the field strength of the first half-cycle, giving rise to distinct responses for single- and multi-cycle pulses as well. To experimentally demonstrate the different nonlinearities, we build a quasi-single-cycle THz pulse by using a binary phase mask on the same iLAPCA THz source [10,72]. The artificially generated second half-cycle pulse serves as a half-cycle probe pulse, which can reveal the similar temporal carrier dynamics using a single-cycle pulse.

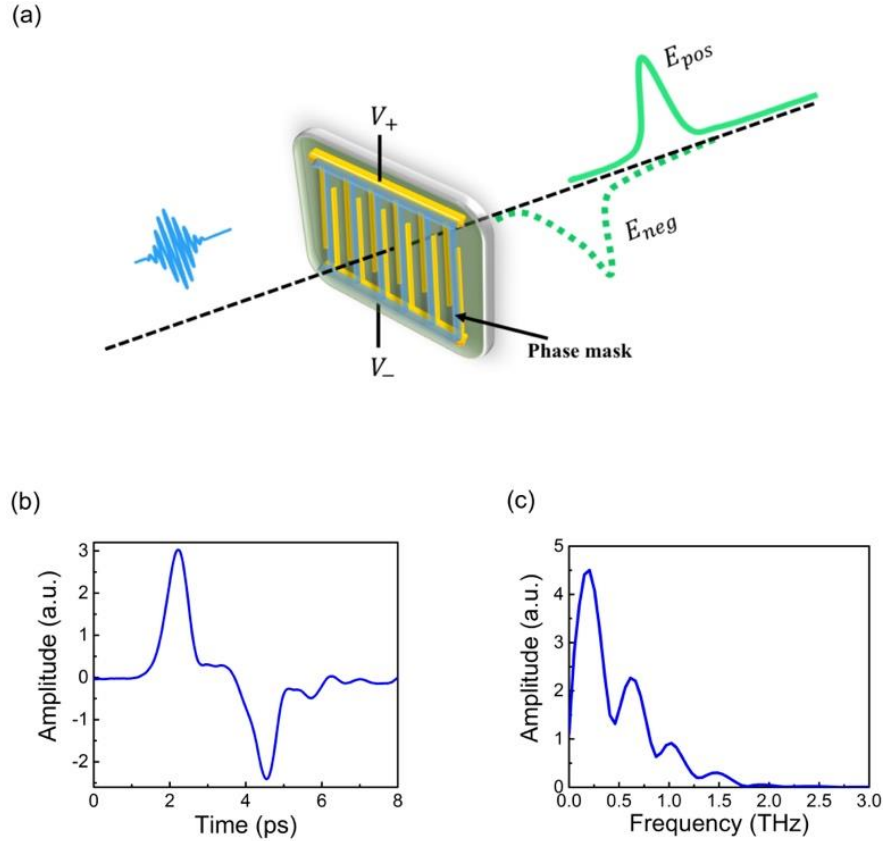


**Fig.5.4: (a) Schematic of the iLAPCA with a binary phase mask. Quasi-single-cycle THz wave is generated by inducing a time delay between two half-cycles. (b) the transmitted THz waveform through the substrate and (c) the corresponding spectrum, where several crests are shown due to the interference between the positive and negative polarities.**

Figure 5.4 (a) shows the schematic of the iLAPCA with a binary phase mask. Instead of a shadow mask that is used to generate half-cycle pulses, we use a binary phase mask (1 mm thickness) to induce a patterned phase delay on the pump laser [10]. Due to the phase delay between the pump laser pulse, the generated two half-cycle THz pulses with opposite polarity are separated in time. With this structure, we obtain a quasi-single-cycle pulse with similar field strengths for positive and negative extremes. By optimizing the position of the binary phase mask,

we achieve a negative peak field that is approximately equal to 80% of the positive peak field. The incident single-cycle THz pulse possess a half-cycle duration (FWHM) of 645 fs for  $E_{pos}$  and 550 fs for  $E_{neg}$ .

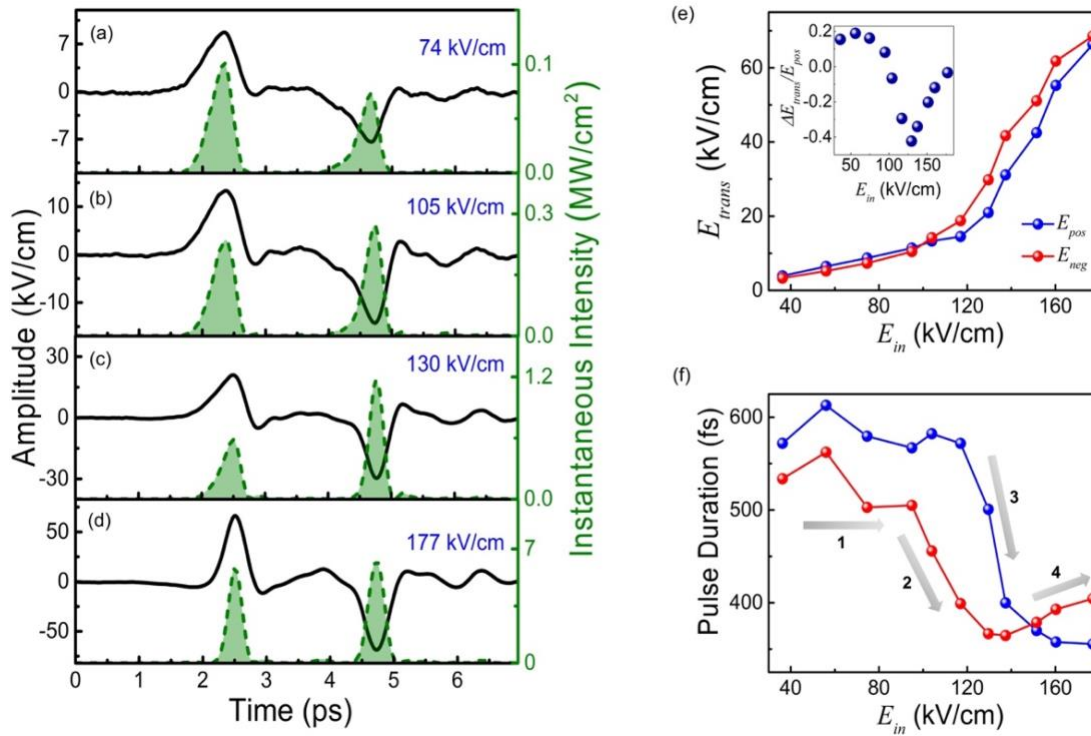


**Fig.5.5:** Transmitted THz pulses (solid black curve) and the instantaneous THz intensity (broken green curve) at various incident fields of (a) 74 kV/cm. (b) 105 kV/cm. (c) 130 kV/cm. and (d) 177 kV/cm. (e) the transmitted fields of negative ( $E_{neg}$ ) and positive extremes ( $E_{pos}$ ) versus the incident field. Inset:  $\Delta E_{trans}/E_{pos}$ , where  $\Delta E_{trans} = E_{pos} - E_{neg}$ . (f) field dependence of half-cycle durations (amplitude FWHM). Four field regions can be identified, representing: 1, the linear regime; 2, current truncation on the negative polarity; 3, current truncation on the positive polarity and 4, pulse broadening of the negative polarity.

We performed nonlinear THz-TDS on the InGaAs sample using the quasi-single-cycle pulses. Four transmitted waveforms at different field strengths are shown in Fig. 5.5 (a), (b), (c) and (d). Transmitted peak fields [Fig. 5.5 (e)] as well as the half-cycle duration [Fig. 5.5 (f)] are extracted for both  $E_{pos}$  and  $E_{neg}$ . At low fields (Region 1 in Fig. 5.5 (f)), linear responses are obtained, and the transmitted THz waveforms remain similar to the incident pulses with  $E_{neg}$  smaller than  $E_{pos}$ . When the peak field is increased to 105 kV/cm, we observe a clear amplitude increase for the negative field extreme [Fig. 5.5 (b)], where  $E_{neg}$  become higher than  $E_{pos}$  after transmission. This waveform “reversal” can be seen more clearly by comparing the instantaneous intensities in the time domain, where the difference reaches a maximum when the incident field is at 130 kV/cm [Fig. 5.5 (c)]. Meanwhile, the half-cycle duration of  $E_{neg}$  decreases from around 500 fs to 360 fs, while that of  $E_{pos}$  is still above 500 fs (Region 2 in Fig. 5.5 (f)). Due to the long relaxation time from the upper valleys to the central valley, this intriguing “reversal” of the transmitted pulse shape is caused by the residual carriers in the low-mobility upper valleys after excitation by  $E_{pos}$ , which results in a higher  $E_{neg}$ . The negative half-cycle  $E_{neg}$  can then rapidly decelerate the high-energy carriers in the  $\Gamma$ -valley, and then reaccelerate them in the opposite direction. In the end, the carriers that acquire enough kinetic energy can be also re-scattered to the upper valleys. However, when  $E_{pos}$  is sufficiently intense (Region 3 in Fig. 5.5 (f)),  $\Delta E_{trans}/E_{pos}$  starts to reduce and the pulse duration of  $E_{pos}$  decreases from 575 to less than 400 fs. This is consistent with the results using half-cycle pulses, where the current truncation leads to a shortening of the transmitted THz pulse. More interestingly, the half-cycle duration of  $E_{neg}$  starts to increase once the THz field is higher than 137 kV/cm, while that of the positive polarity continues to decrease (Region 4 in Fig. 5.5 (f)). This is a direct result of the intervalley carrier dynamics induced by single-cycle pulses as verified by our calculation. As shown in the following theoretical discussion, weak current density during

$E_{neg}$  allows more low-frequency components to be transmitted through the sample and in turn increases the half-cycle duration.

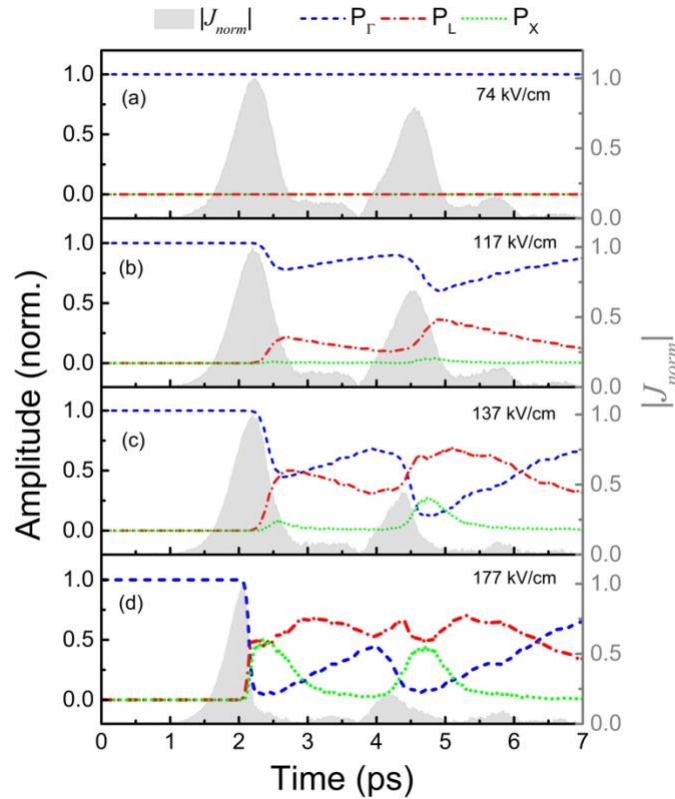


**Fig.5.6:** Calculated temporal dynamics of intraband free carriers driven by quasi-single-cycle THz pulse (ensemble Monte-Carlo simulation). Normalized absolute value of the current density (gray shaded area), carrier population in  $\Gamma$  (magenta curve), L (broken green line) and X (blue point curve) valleys at different incident field strengths: (a) 74 kV/cm. (b) 117 kV/cm. (c) 137 kV/cm and (d) 177 kV/cm.

The detailed carrier dynamics obtained from ensemble Monte-Carlo simulation are shown in Fig. 5.6. At low fields [Fig. 5.6 (a)], most of the electrons are in the  $\Gamma$  valley of the conduction band, where they possess small effective mass as well as low scattering rate. With higher field of

117 kV/cm [Fig. 5.6 (b)], intervalley scattering between  $\Gamma$  and L valleys take place for both positive and negative polarities of the pulse. The positive THz field provides the high kinetic energy to the charge carriers and leave some carriers in the upper valleys when the negative polarity transmits through the sample. Higher THz transmission is thus expected for the negative polarity and in turn a pulse shape “reverse” presents in the transmitted THz waveform. The contrast between the two peaks become stronger when the field is increased to 137 kV/cm, where significant intervalley scattering between the various valleys ( $\Gamma$ , L and X) lead to a current truncation within the negative polarity [Fig. 5.6 (c)]. Significant half-cycle pulse shortening is thus expected for the negative polarity. At this field of 137 kV/cm, around 50% carriers (blue broken curve) are scattered into the upper valleys during the positive polarity and the corresponding time scale of the current density is therefore still comparable to the incident pulse. However, since the positive polarity has brought the material onto a high-energy state with much fewer carriers close to the bottom of the conduction band, the amplitude of the current cut during the negative polarity is limited. On the other hand, when  $E_{pos}$  is sufficient to induce significant intervalley scattering effect, a current cut with large amplitude can be generated within the positive polarity, giving rise to efficient high-frequency generation similar to the half-cycle excitation [Fig. 5.6 (d)]. The amplitude of the current density within the negative polarity is therefore largely reduced due to the “low-conductivity state” of the semiconductor, leading to a significant transmission enhancement for both high and low frequency components and in turn increase the negative half-cycle pulse duration as observed experimentally [Fig. 5.5].

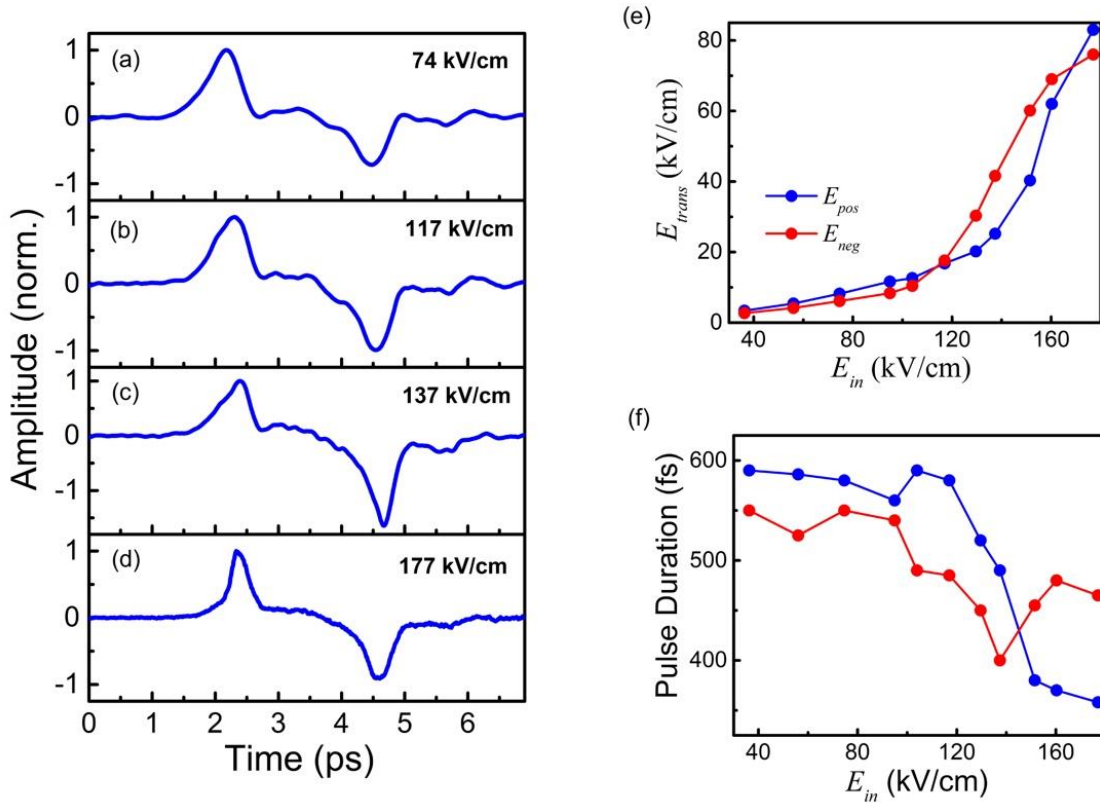


**Fig.5.7: Simulated transmitted THz pulses at (a) 74 kV/cm. (b) 117 kV/cm. (c) 137 kV/cm and (d) 177 kV/cm. (e) the transmitted peak fields of negative ( $E_{neg}$ ) and positive ( $E_{pos}$ ) half-cycle pulses versus the incident THz field. (f) field dependence of half-cycle duration (amplitude FWHM).**

Fig. 5.7 presents the transmitted THz pulses obtained from calculation. The calculated THz waveforms are normalized by the corresponding peak field of the  $E_{pos}$ . As shown in Fig. 5.7 (e),  $E_{neg}$  becomes higher than  $E_{pos}$  between 105 and 117 kV/cm, and at highest field of 177 kV/cm,  $E_{pos}$  becomes higher than  $E_{neg}$ . At high fields, the calculated THz pulses are stronger than the results obtained from THz-TDS, which could be due to the idealization of the thin conducting film,

where the phase variation is not included in the time-domain calculation. As shown in Fig. 5.7 (f), the half-cycle duration of  $E_{neg}$  starts to decrease first down to around 400 fs. Then the duration of  $E_{pos}$  decreases significantly when the field is above 137 kV/cm. At high fields, the half-cycle duration of  $E_{pos}$  decreases down to approximately 350 fs, while that of  $E_{neg}$  starts to increase due to the weaker current density caused by the carrier heating from the first half-cycle pulse. Here, some discrepancies have been shown between simulation (Fig.5.7 (e) and (f)) with experimental results (Fig.5.5 (e) and (f)) between 100 kV/cm and 120 kV/cm as well as the highest applied field of 177kV/cm. The alloy scattering rate is not taken into account in our model, which could result in some nonperiodic potential fluctuation caused by the random disposition of the different group III atoms that in turn alter the intervalley scattering rate [50,70]. This problem can be resolved by adding the alloy scattering effect in the simulation as a fitting parameter.

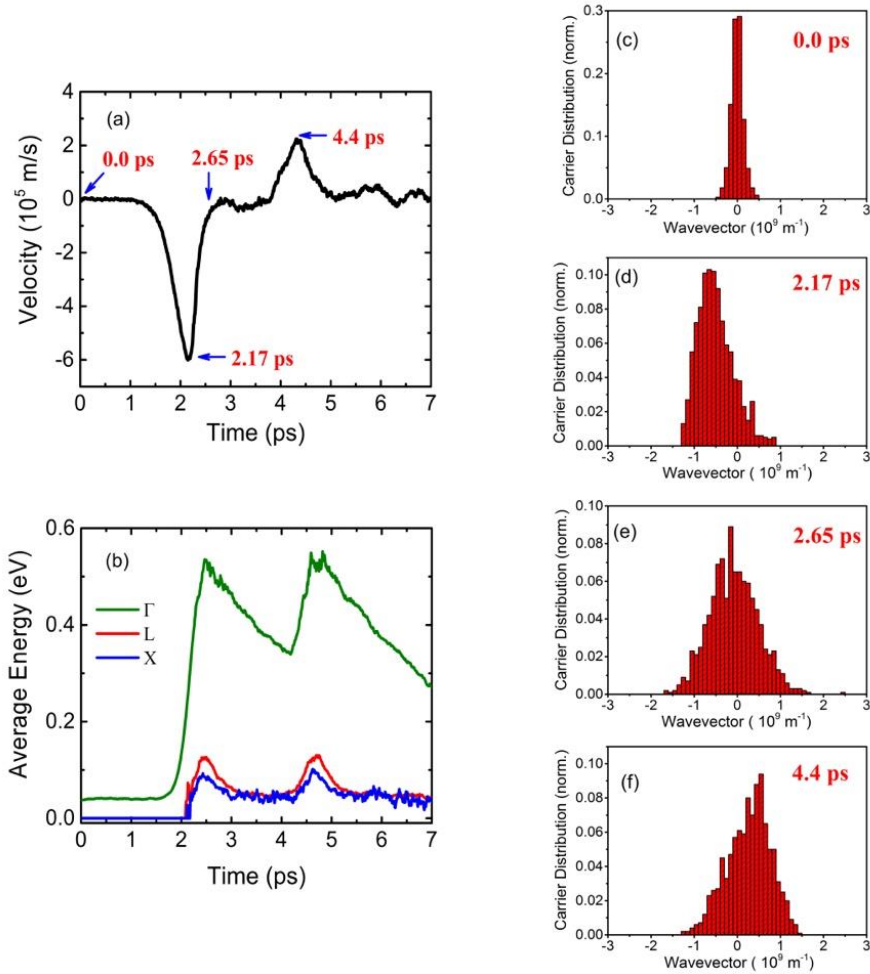


**Fig.5.8: (a) Calculated carrier average velocity driven by the quasi-single-cycle pulses with a peak field of 160 kV/cm. (b) average carrier energy at three valleys. The carrier momentum distribution at (a) 0.0 ps, (b) 2.17 ps, (d) 2.65 ps and (d) 4.4 ps.**

Here, we retrieve the carrier distribution at different points in time from the calculation as well. Fig. 5.8 (a) shows the carrier average velocity driven by the quasi-single-cycle pulse with a peak field of 160 kV/cm. In Fig. 5.8 (b), we show the average energy of carriers in the three different valleys  $\Gamma$ , L and X. We chose four time points on the current waveform and calculated the carrier momentum distribution as shown in Fig. 5.8 (c), (d), (e) and (f). The initial carrier distribution is

shown in Fig. 5.8 (c). After acceleration of the THz field, the carriers have shown a clear high field response in which the drift energy dominates at 2.17 ps (Fig. 5.8 (d)). As shown in Fig. 5.8 (e), the isotropic intervalley scattering then starts to take place and produces a large random component to the carrier momentum. As a result, the shift of the carrier distribution driven by the second half-cycle is much less due to the thermal energy dominant carrier dynamics (Fig. 5.8 (f)).

### **5.3 Terahertz Harmonic generation due to intervalley scattering effect (theory)**

In principle, intervalley scattering randomizes the momentum of different charge carriers and destroys coherent transport. However, the total current density is determined by the collective motion of an ensemble of carriers, or the macroscopic THz conductivity. Within one half-cycle pulse, the total current density has shown an acceleration followed by an abrupt reduction. From the excitation by the first half-cycle, a distorted current that synchronizes with the driving THz fields can be generated, which could lead to discrete HHG when multi-cycle pulses are applied. Here, although the coherency of individual scattered particles is diminished by isotropic intervalley scattering, the overall nonlinear current density has shown coherent characteristics that varies in phase with the driven THz pulse. In fact, this is similar to the THz coherent HHG in graphene, where a suppression in the temporal peaks of the current density is caused by the linear band dispersion, giving rise to the generation of odd harmonics in the transmitted THz wave [27,28].

For intraband Bloch oscillation, the number of oscillations within each half-cycle is field-dependent and increases with the driving laser field [56,57]. However, the field-dependence is considerably reduced for subcycle nonlinearities induced by non-parabolicity of the band dispersion [27,28] or by the current truncation due to carrier heating. The extent of non-

parabolicity and the speed of carrier heating determines the efficiency and the optimum spectral range of HFG. As can be seen from our experimental results (Fig. 5.1 (b) and Fig. 5.5 (f)), the reduction in the subcycle duration saturates gradually at high fields for the studied  $\text{In}_{0.57}\text{Ga}_{0.43}\text{As}$  sample. Therefore, low frequency THz sources [35], which possess much longer half-cycle duration, are more favorable here for the observation of HFG beyond their incident frequency range. In reality, depending on the desired functionality, the field at which the subcycle duration saturates can be controlled by tuning the carrier concentration, the thickness of the sample, or by using other semiconductor material that have different band structure, as well as mobility and speed of carrier heating and relaxation.

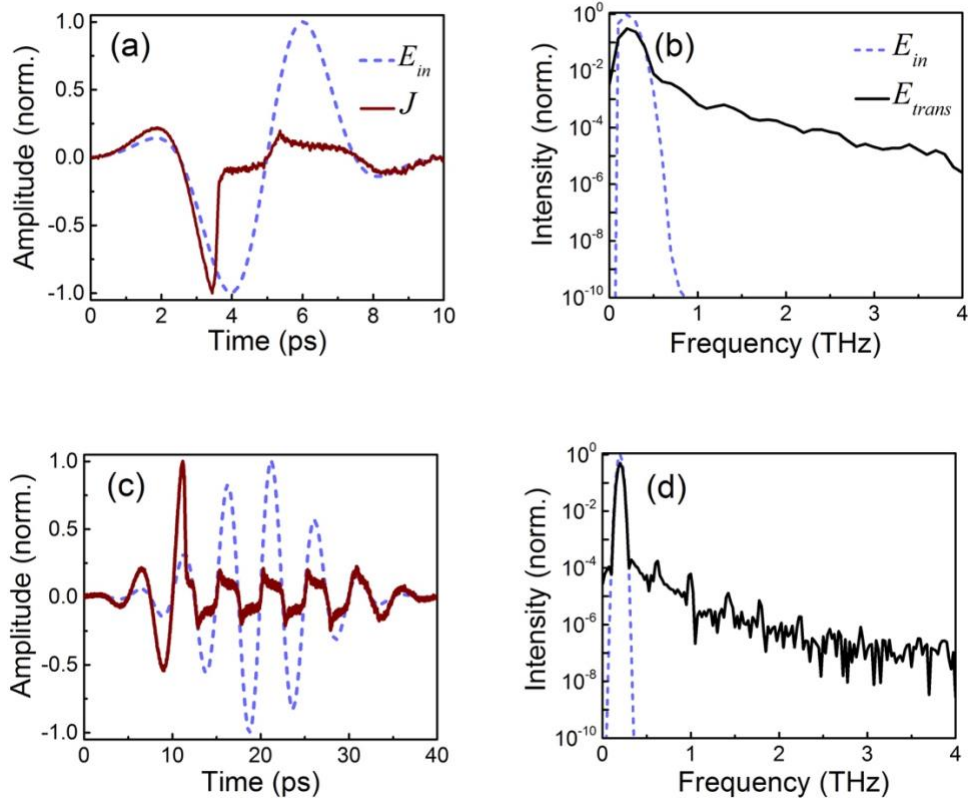


**Fig.5.9: HHG from single-cycle and multi-cycle THz pulses centered at 0.2 THz (Simulation). (a) nonlinear current density driven by single-cycle THz pulses centered at 0.2 THz. The applied peak field is 180 kV/cm.  $t_{relax}$  corresponds to the carrier relaxation time and  $t_{ETHz}$  represents the acceleration time to scatter the carriers to side valleys. (b) the intensity spectra of the  $E_{in}$  and  $E_{trans}$ . The intensity is normalized to the peak intensity of  $E_{in}$ . (c) nonlinear current density driven by multi-cycle THz pulses centered at 0.2 THz. The peak incident field used here is 350 kV/cm. (d) the normalized intensity spectra of the  $E_{in}$  and  $E_{trans}$ .**

In Fig. 5.9, we show results of theoretical calculations of HHG due to scattering effect of single-cycle and multi-cycle THz pulse. The shape of the HH spectrum is determined by the generation mechanism as well as the spectrum of the excitation pulse. Clear harmonic peaks of the driving frequency should be observed for multi-cycle pulses, while broadband high frequency

components are expected for single-cycle or half-cycle pulses. Here, the spectrum of the single-cycle pulse is confined below 0.6 THz, which is the third harmonic of the driving frequency (0.2 THz). A broadband transmitted spectrum is generated due to the nonlinear current density. As demonstrated experimentally by the measurements of quasi-single-cycle pulses, the amplitude of the second half-cycle current density is much lower due to the long carrier relaxation time  $t_{relax}$ . However, this distorted half-cycle signal remains in the successive half-cycles as long as the field is sufficient to scatter the carriers to the upper valleys. As a result, the generated HH shows much less dependence on the driving field. Using multicycle pulses (Fig.5.9 (c) and (d)), clear HHG is observed up to the 11<sup>th</sup> order on the transmitted THz spectrum.

In conclusion, nonlinear interactions between intense subcycle THz pulse and intraband charge carriers lead to unique experimental observations with the emission of a continuum high-frequency THz spectrum. The nonlinearities of material evolve half-cycle by half-cycle along the entire THz waveform. Our experimental and theoretical investigations have demonstrated a new approach to subcycle control of THz high frequency generation based on intraband carrier scattering effects. Our findings are important for future THz electronics and optoelectronics. Incoherent effects such as intervalley scattering could considerably alter the waveform of a sub-THz pulse, resulting in the generation of high frequency components.

## Chapter 6

### From intraband to interband nonlinear terahertz optics

In Chapter 5, we have demonstrated that the intervalley scattering effect dominates the nonlinear responses of doped semiconductor  $\text{In}_{0.53}\text{Ga}_{0.47}\text{As}$  at high field around 200 kV/cm. For low-frequency LAPCA THz sources (centered at 0.15 THz), such effect can be used to control the transmitted THz spectra via high frequency generation up to 2.2 THz. On the other hand, subcycle nonlinearities are not significant for higher frequency THz pulses above 1 THz [50,52]. However, due to a huge contrast of conductivities before and after intervalley scattering, it has been suggested that by using intraband carrier heating effect, doped semiconductor can serve as a saturable absorber in the THz frequency range [50,52]. Here, a straightforward question is what will happen if the field strength is further increased and how does it affect the functionalities of the doped semiconductor as a saturable absorber.

In 2011, Hirori *et al.* [74] has shown that at low temperature, a 1 MV/cm electric field of a THz pulse can generate a substantial number of electro-hole pairs via impact ionization in GaAs quantum wires. More recently, a transition from intraband intervalley scattering to interband impact ionization and Zener tunneling have been observed by Fan *et al.* [75] on doped GaAs semiconductor samples with a THz metamaterial structure. A maximum local field of 2.8 MV/cm was estimated with the field enhancement of THz metamaterial structure. In fact, with the remarkable advances in THz photonics during the last decade, a THz peak field of a few MV/cm is now accessible [76-78]. Hence, it is very important to extend our investigation of the

optoelectronic properties of doped semiconductors by using intense THz pulses with field strength of several MV/cm.

This work is in collaboration with Prof. Savel'ev's group from Lomonosov Moscow State University. Extremely intense few-cycle THz pulses are generated from the organic crystal 4-NN, NN-dimethylamino-4'4'-N'N'-methyl-stilbazolium 2, 4, 6 trimethylbenzenesulfonat (DSTMS). The maximum emitted THz electric field is more than 2 MV/cm.

We show that as the THz beam becomes more intense, interband dynamics will eventually take place in addition to the intervalley scattering effects. We demonstrate that the doped semiconductor InGaAs can be an excellent candidate as a saturable absorber up to a certain THz field. The THz energy transmission ratio between the sample and the bare substrate increases from 6% to approximately 86% by increasing the THz beam intensity. Compared to the optical counterparts, THz saturable absorber based on nonlinear carrier dynamics can be used in a broad frequency range, in which the overall performance is nearly frequency independent. However, at higher THz intensities, a crossover from intraband to interband nonlinear optics takes place, which increases the number of low-energy free charge carriers and in turn reduces the THz transmission.

## **6.1 Observation from intraband to interband carrier dynamics**

*This chapter is written based on:*

© X. Chai, X. Ropagnol, A. Ovchinnikov, O. Chefonov, A. Ushakov, C. M. Garcia-Rosas, E. Isgandarov, M. Agranat, T. Ozaki, and A. Savel'ev. "Observation of crossover from intraband to interband nonlinear terahertz optics." *Optics Letters* **43**, no. 21: 5463-5466. [2018] *Optical Society of America*.

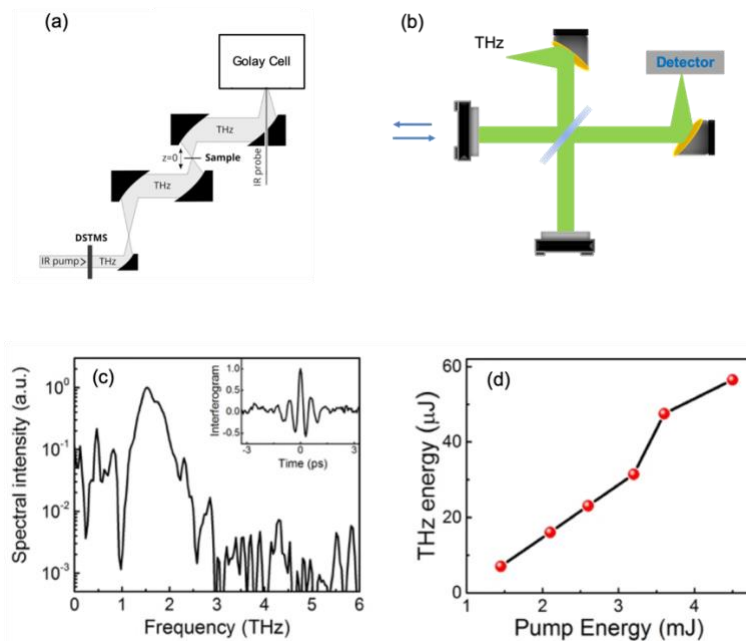


**Fig.6.1: (a) Experimental-setup. The THz pulse energy is measured using a calibrated Golay Cell. (b) THz Michelson interferometer is used to retrieve the THz spectra. (c) THz intensity spectra. (d) Radiated THz pulse energies as a function of the IR pump energy.**

The organic DSTMS crystal is pumped by 100-fs laser pulses at a central wavelength of 1240 nm, which is provided by a 10 Hz multistage chirped-pulse amplification Cr:Mg<sub>2</sub>SiO<sub>4</sub> (Cr:forsterite) laser system [76,79]. Fig. 6.1 (a) shows the detailed schematic of the experimental set-up [79]. The energies of the radiated THz pulses were measured by a calibrated Golay Cell (GC-1D, Tydex Inc.), which provides similar results of energy measurements of a pyroelectric sensor (SPI-D, Spectrum Detector Inc.) [76]. As shown in Fig. 6.1 (b) and (c), the emitted THz spectra were retrieved by interferometric autocorrelation using a THz Michelson interferometer. By splitting the THz pulses into two and varying the relative time delay between the two pulses using a time-delay stage, we can retrieve the THz interference pattern and calculate the corresponding intensity spectrum. As shown in Fig. 6.1(c), the emitted THz spectrum is centered

at 1.8 THz and an absorption dip is observed at around 1 THz, which is due to the phonon absorption of the DSTMS crystal [76]. Fig. 6.1(d) shows the measured THz energies (uncertainty  $\leq \pm 3\%$ ) as a function of the pump laser energy. We observed a nearly linear increase in THz output energy by increasing the pump energy, which is consistent with the previous measurements under similar experimental conditions [76]. Open-aperture Z-scan measurements on semiconductor  $\text{In}_{0.53}\text{Ga}_{0.47}\text{As}$  are performed with these incident THz energies. The radius of the THz beam at the focus is  $259 \mu\text{m}$  at  $1/e^2$ , which is measured using the knife-edge technique. A separate calibration experiment was performed to make an independent estimate of the THz field strength using electro-optical (EO) sampling technique with a  $100\text{-}\mu\text{m}$  thick GaP crystal and Tydex THz attenuators (1% and 3%). The measured waveforms are shown in Fig. 6.4 and used to perform the theoretical calculation. By dividing the difference to the sum of the measured intensities from the two photodetectors, we obtained a modulation of around 5% and the corresponding peak field for the maximum energy of  $56 \mu\text{J}$  is approximately  $2.36 \text{ MV/cm}$  [80]. Extremely intense THz field leads to the observation of a clear THz image at the beam focus from a standard silicon CCD camera, in which free charge carriers are generated through interband tunneling [80].

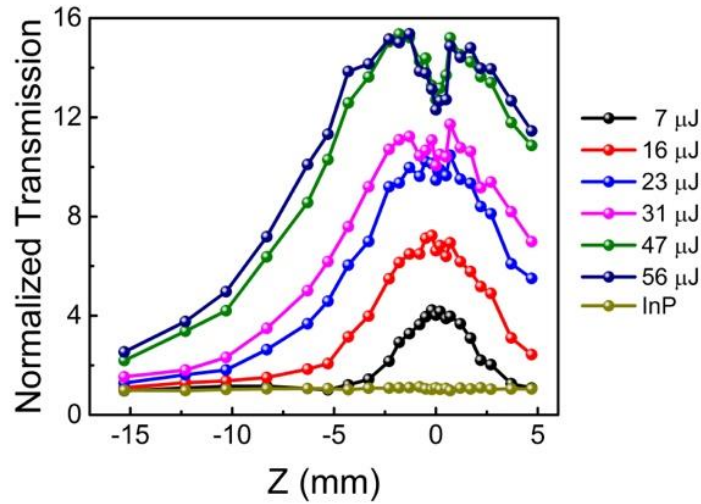


**Fig.6.2: Z-scan normalized transmission (enhancement ratio) of various THz pulse energies measured by the Golay cell. All the transmitted THz energies are normalized to the transmitted THz energy at  $Z = -15.3$  mm.**

Fig. 6.2 shows the behavior of the normalized transmitted THz energy obtained from the Z-scan experiments for several THz energies. All the transmitted THz energies are normalized to the THz energy transmitted through the  $\text{In}_{0.53}\text{Ga}_{0.47}\text{As}$  sample placed at  $Z = -15.3$  mm from the THz focus, and with a THz pulse energy of  $7 \mu\text{J}$ . Nonlinear THz transmission is not observed with the bare substrate InP. By illuminating the  $\text{In}_{0.53}\text{Ga}_{0.47}\text{As}$  sample with low THz pulse energies of 7 and  $16 \mu\text{J}$ , a clear THz saturable absorption is observed when the sample is placed near the focus. Linear responses with transmission enhancement ratio of approximately 1 are obtained when the sample is scanned far away from the focus. THz saturable absorption is further enhanced when the THz pulse energies are increased to 23 and  $31 \mu\text{J}$ , where an enhancement ratio of approximately 9 is observed near the focus. Here, nonlinear absorption bleaching starts to take place at  $Z > 10$  mm, and we observe a plateau of the enhancement for sample positions located at  $Z = \pm 2$  mm. More interestingly, when using the maximum tested THz pulse energies of 47 and  $56 \mu\text{J}$ , we observe an

intriguing reduction in the enhancement ratio near the focus. This unusual response suggests that the THz conductivity starts to increase at such extremely high fields of a few MV/cm.

We further measured the transmitted THz spectra using the same approach of interferometric autocorrelation by a Michelson interferometer. An overall transmission enhancement followed by a reduction of spectral intensity is observed around the central frequency by moving the sample towards the focus.

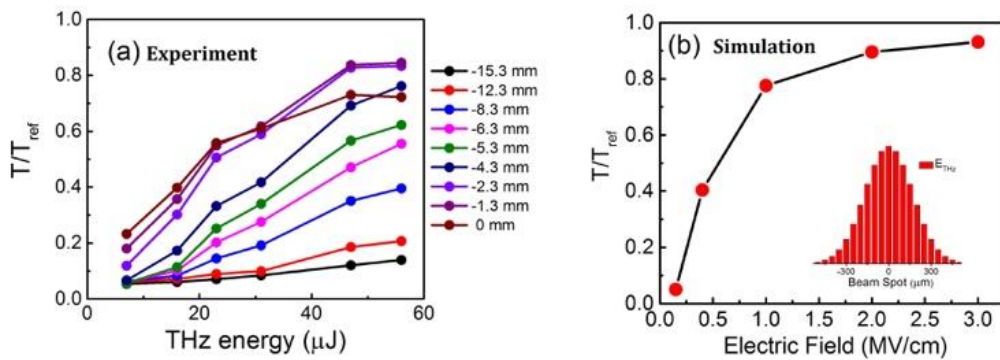


**Fig.6.3: (a) Transmitted energy ratio between InGaAs sample and bare InP substrate versus the incident THz pulse energy at different Z-scan positions. (b) Calculated results by the described intraband model, where the time-domain simulations are performed at each  $50 \mu\text{m}$ .**

Fig. 6.3 shows the measured and calculated THz transmission ratio between the transmitted energy through the sample and the bare substrate for various Z-scan positions or incident field strengths. A clear saturable absorption response is shown for several Z positions. At low intensities, the THz transmission is only 0.06 and remains almost identical for several THz energies. When the sample is close to the focus, the THz transmission increases nonlinearly with the incident THz energy, and a maximum transmission of 0.85 is obtained at  $Z = -2.3$  and  $-1.3$  mm. On the other

hand, the transmission measured at the focus increases rapidly at low energies and then starts to saturate, subsequently decreasing from 0.85 to 0.7 for the maximum THz energy of 56  $\mu\text{J}$ .

To obtain quantitative insight into the nonlinear absorption bleaching effects, we performed a theoretical simulation using the THz waveforms measured via electro-optical sampling. Since the experiment was performed on a 10 Hz laser system, the measured THz waveform is noisy and can only be used as an estimation to calculate the transmitted THz fields. The incident THz waveforms are shown in Fig. 6.4 and the calculated transmission ratio is shown in Fig. 6.3(b).

In Fig. 6.3(b), we calculate the transmitted THz waveform by varying the peak field of the principal half-cycle pulse from 150 kV/cm up to 3 MV/cm (Fig. 6.4) and the pulse energy is calculated by the time integral of the modulus squared of the THz field [50]. Since we measured the whole beam energy, the THz spatial field distribution needs to be considered in the calculation. For simplicity, we assume the same Gaussian field spatial distributions for all the frequency components. Time-domain simulations are carried out for each 50  $\mu\text{m}$  along the beam spot and the transmitted THz energy is then estimated by normalizing the corresponding surface areas. As shown in Fig. 6.3(b), we obtain a linear transmission of 0.07 when the incident THz peak field is at 150 kV/cm, which increases rapidly to 0.8 when the field is at 1 MV/cm. At high fields above 1 MV/cm, the absorption bleaching effect saturates gradually and a transmission ratio of 0.89 is obtained when the peak field is at 2 MV/cm.

As can be seen from the comparison between the experimental and simulation results, the overall responses are always dominated by the saturable absorption due to intraband carrier heating. By increasing the THz intensity, THz transmission increases approximately 17 times and the sample becomes nearly transparent. However, the dip of the Z-scan curve around the focus suggests that other effects that can increase the THz conductivity takes place under the illumination of extremely

intense THz intensity, which in turn reduces the transmitted THz energy. This conductivity enhancement can be realized by adding extra high-mobility free charge carriers in the semiconductor sample. Two interband pathways are possible here, which are impact ionization and Zener tunneling [73-75,81-87].

In the presence of a strong electric field, the instantaneous potential energy in a semiconductor can drop significantly over atomic distances, facilitating field-induced interband Zener tunneling [88,89]. Comparing with the intraband heating effect that reduces the THz conductivity, the generation of a large density of carriers on ultrashort time scales via Zener tunneling can, on the other hand, increase the THz conductivity and in turn reduce the transmitted THz energy. For electrons that are already in the conduction band, they can be accelerated by strong electric field and gain sufficient energy to scatter electrons from valence band to the conduction band as well through impact ionization [90]. Both interband Zener tunneling and impact ionization can provide extra free charge carriers, giving rise to an enhancement of THz conductivity at high fields.

We estimate the efficiency of impact ionization and Zener tunneling using the model proposed by Keldysh and Kane [88,89]. The impact ionization rate is in the order of  $1 \times 10^{10} \text{ s}^{-1}$  at high energies above 1.4 eV and become comparable to the intervalley scattering rate when the electron energy is far above the bottom of the conduction band (approximately 3 eV in InGaAs) [90]. On the other hand, Zener tunneling is also a pronounced phenomenon in direct bandgap semiconductors such as InGaAs [73-75,81-87]. At high fields above approximately 1.5 MV/cm, Zener tunneling can also generate a carrier concentration close to the initial doping concentration of  $2 \times 10^{18} \text{ cm}^{-3}$  within 100 fs [90]. However, increased carrier density reduces the instantaneous driving field on the thin film and as a result the nonlinear responses of doped semiconductor are always dominated by the carrier thermalization induced by scattering effects.

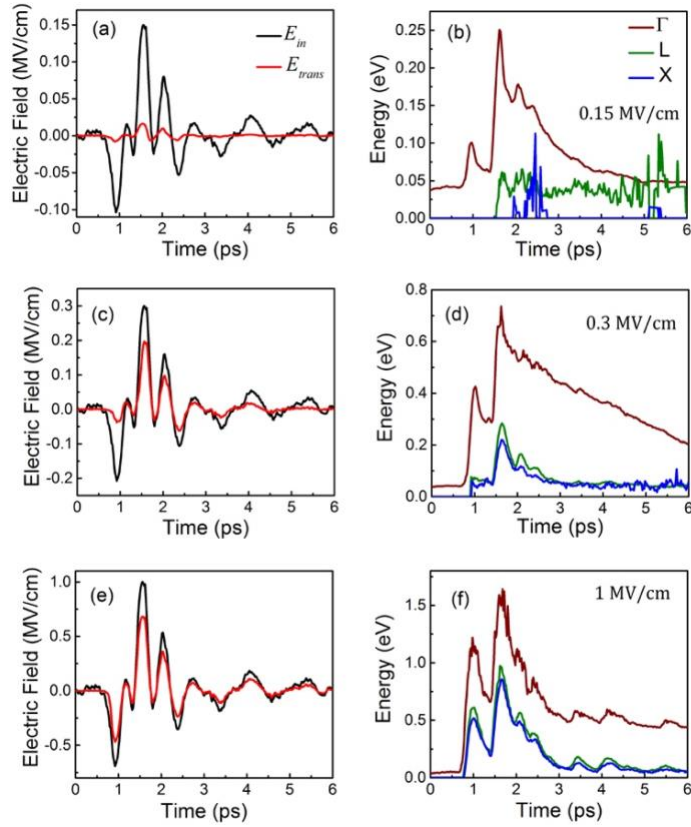


**Fig.6.4: Incident and calculated transmitted THz waveforms (a), (c), (e) as well as the corresponding average carrier energy (b), (d), (f) at 0.15, 0.3 and 1 MV/cm, respectively.**

In Fig. 6.4, we present the calculated transmitted THz waveforms and the average carrier energy at three fields of 0.15, 0.3 and 1 MV/cm based on the intraband ensemble Monte-Carlo model. At 0.15 MV/cm, we obtain an extremely low THz transmission due to the large amount of free charge carriers that are initially present in the  $\Gamma$  valley. Most of the carriers remain in the central valley during acceleration and the relaxation of the material is thus only determined by intravalley dynamics.

At 0.3 MV/cm, a clear transmission enhancement is shown in the time domain for several half-cycles. Here, the instantaneous peak transmission is only 0.16 for the first half-cycle, while the

transmission of the second half-cycle reaches approximately 0.6. This is ideal for the applications of saturable absorption, where the first half-cycle pulse is nearly completely truncated from the THz signal and in turn reduces the total pulse duration. As shown in Fig. 6.4 (d), both intervalley and intravalley relaxation take place after the THz excitation. Since the intervalley scatterings are due to optical phonons that occur in a shorter time-scale [54], the final carrier relaxation time is determined by intravalley relaxation in the  $\Gamma$  valley.

By further increasing the field to 1 MV/cm, the current density reduction takes place within the first negative half-cycle of the THz pulse, giving rise to an extremely low conductivity over the entire THz waveform afterwards. The pulse shortening effect becomes negligible with a transmitted pulse duration close to the incident THz signal. Furthermore, in addition to the high energy acquired by the electron, the transmitted field becomes saturated and becomes close to 0.65 of the incident field. This saturation occurs for all higher incident field strengths. The electron energy exceeds 1.4 eV and reaches around 3 eV when the incident peak field is around 2 MV/cm, where both impact ionization as well as Zener tunneling can take place and thus reduce the transmitted THz energy.

Here, our results have indicated some important guidelines to use doped semiconductor material  $\text{In}_{0.53}\text{Ga}_{0.47}\text{As}$  for the applications of saturable absorbers. The key parameters for the choice of a saturable absorber are the absorption wavelength range, the relaxation time and the saturation intensity. Here, doped semiconductor based THz saturable absorber possess a unique advantage of wide absorption frequency range. As shown in Fig.6.4, a half-cycle pulse is enough to turn the sample from high conductivity to low conductivity, giving rise to a frequency-independent THz transmission afterwards. The total relaxation time is in the range of tens of picoseconds and increases with THz intensity. This is due to the slow intravalley electron relaxation from high

energies of the conduction band. On the other hand, at high fields, doped semiconductors are eventually limited by the effects that can induce interband excitation, which in turn increases the THz absorption. In practice, once the sample thickness and the initial doping concentration is fixed, this problem can be avoided by enlarging the THz beam size in order to achieve the desirable performance of the saturable absorption.

In conclusion, we investigate the nonlinear carrier dynamics in n-doped semiconductor InGaAs and study its effects on the transmitted THz pulses. Intense THz pulses generated from the organic crystal DSTMS have pushed the nonlinear responses of doped InGaAs semiconductor into a new regime that involves interband carrier dynamics. Intraband heating dominates the overall THz responses and therefore doped semiconductor can still be a good candidate for the applications of saturable absorber. However, the interband effects as well as the time-scale of the strong absorption in the linear regime compared to the total pulse duration must be taken into account for the design and optimization of future optical systems in the THz frequency range.

## Chapter 7

### From linear to circular ponderomotive acceleration

Polarization is a unique property of transverse waves, such as electromagnetic waves. By using THz pulses with elliptical or circular polarization, we can easily realize a ponderomotive acceleration of free charge carriers with the orientation of electric field varying continuously in time. Hence, it is of great interest to perform a nonlinear THz-TDS with tunable THz polarization states. In 2011, Blanchard *et al.* [91] has demonstrated the anisotropic effective mass of energetic electrons in an isotropic, nonparabolic conduction band using THz-pump THz-probe spectroscopy with crossed polarization orientation. Due to the effective-mass anisotropy, after an intense THz pump, the transmission of the probe THz pulses with cross-linear polarization is found to be less than that with polarization collinear to that of the THz-pump [91]. This motivated us as well to perform such experiments using elliptically polarized THz pulses, because a much more efficient acceleration in the central  $\Gamma$  valley should be observed when the electric field vector can rotate in a picosecond time-scale.

In the following, we will first discuss the technique we developed for the generation of elliptically polarized THz pulses. Then we will discuss briefly the initial experimental results of the transmitted THz pulses through our  $\text{In}_{0.53}\text{Ga}_{0.47}\text{As}$  sample. In the last part, we will introduce an improved THz detection method that employs the Stokes-Mueller formalism. By using this technique, we can measure the amplitude and direction of the THz electric field vector, in space and in time. A theoretically unlimited dynamic range can be achieved as well. This technique is free of the small-angle-approximation used in EO sampling for the induced phase delay  $\phi$  ( $\sin \phi \approx$

$\phi$ ), or the over-rotation problem as we discussed in Chapter 2.3 of the conventional EO sampling technique.

## 7.1 Generation of elliptically polarized terahertz pulses

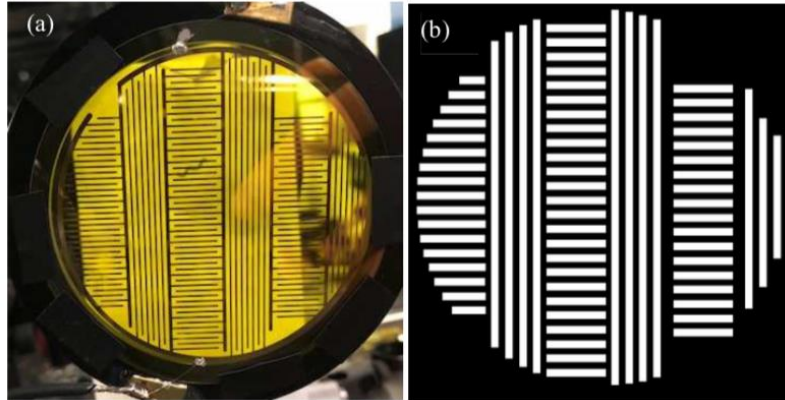


**Fig.7.1: (a) A photo of the ZnSe based iLAPCA with crossed electrodes. (b) a combination of shadow and binary phase mask is used here to generate THz pulses with tunable ellipticity. Three phase plates can be placed before the vertically or horizontally oriented electrodes.**

To generate THz waveforms with rotated field vectors, we have designed a unique iLAPCA source with both vertically and horizontally oriented electrodes [10,92]. As shown in Fig. 7.1, the iLAPCA used here is composed of two sets of electrodes that have orientations perpendicular to each other, which allows the generation of THz electric fields with crossed polarization. Similar to the generation of quasi-single-cycle pulses, we use a delay mask here for one polarization in order to generate either right-hand or left-hand elliptically polarized quarter-cycle THz pulses [10,92]. Here, we prepared three masks with different thickness to tune the angular speed of the THz field vector in the time domain.

## 7.2 Elliptically polarized THz-TDS on In<sub>0.53</sub>Ga<sub>0.47</sub>As

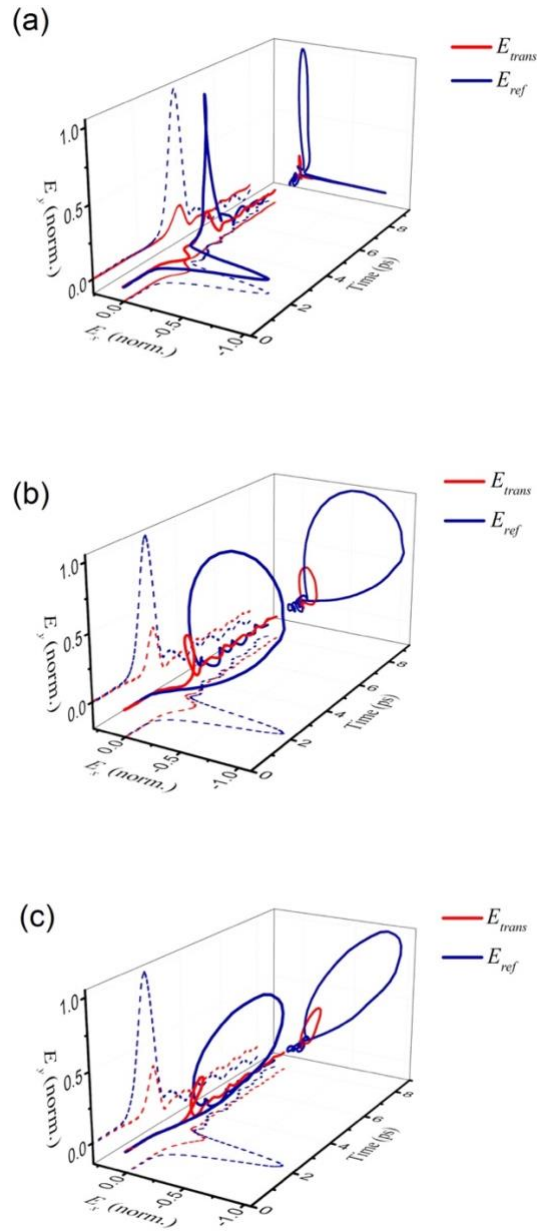


**Fig.7.2:** Transmitted THz waveforms through the bare InP substrate  $E_{ref}$  as well as the InGaAs sample  $E_{trans}$  with different thickness of phase masks of (a) 1, (b) 0.2 and (c) 0.12 mm.

To measure the two electric field components at  $x$  and  $y$ -direction in the laboratory frame, we place a wire-grid polarizer between the two off-axis mirrors after the studied sample and rotate its

orientation as well as the orientation of the detection crystal for the measurement of each orientation. In fact, we found that it is quite challenging to perform such measurement, because it is difficult to maintain the exact same orientation between each rotation by manually rotating the wire-grid polarizer. To perform nonlinear THz-TDS measurement, we need to switch between the substrate and the sample for the measurement of  $x$  and  $y$ -component. In Chapter 7.3, we proposed a new THz detection method that can solve this problem.

Fig. 7.2 shows the initial experiment results of THz-TDS measurement on  $\text{In}_{0.53}\text{Ga}_{0.47}\text{As}$  using elliptically polarized THz pulses. Fig. 7.2 (a) shows the result when the two half-cycle THz pulses are separated by 1.6 ps. The incident peak electric field of each component is approximately 65 kV/cm. Since the two half-cycles are well separated, the transmitted pulses are similar to that using quasi-monocycle pulses. The peak field is too weak to induce any intervalley scattering effect. On the other hand, by reducing the delay between the two half-cycle pulses, we observed a half-cycle pulse truncation on the rear part of the quarter-cycle elliptically polarized THz pulse [Fig. 7.2 (b) and (c)]. In fact, with a phase mask thickness of 0.1 mm, the incident peak field is approximately 90 kV/cm, which is much smaller compared with the THz field needed to induce nonlinear effects using THz pulses with linearly polarization (approximately 130 kV/cm to observe a clear half-cycle truncation with similar acceleration duration). Furthermore, after transmission, due to the huge conductivity contrast, the orientation of the polarization ellipse rotates towards the  $y$ -axis.

Our results have shown that elliptically polarized THz pulses are indeed much more efficient than linearly polarized THz pulses to accelerate free charge carriers, which could be partly due to the anisotropy of the carrier effective mass [91]. Further experiments as well as a 2-D Monte-Carlo calculation is needed to fully understand the observed effects.

### 7.3 Development of detection approach using Stokes-Mueller formalism

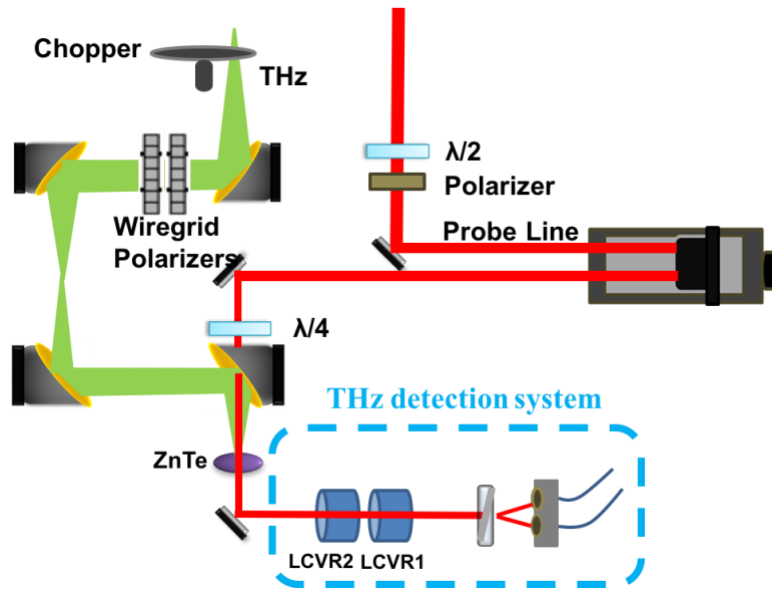


**Fig.7.3: Experimental set-up.** We use a polarization state analyzer that is composed of two liquid crystal variable retarders and a Wollaston prism.

The widely used EO sampling technique has made terahertz THz-TDS an extremely powerful tool to investigate the linear and nonlinear properties of materials in the far-infrared spectral range [4,6,18]. As discussed in Chapter 2, a fully coherent detection allows a direct measurement of the amplitude and the phase. For low-field measurements, this allows one to fully extract the complex refractive index of the material without assuming the Kramers-Kronig relations [93]. At high fields, on the other hand, such experiments become challenging, due to the small angle approximation used in conventional EO sampling technique [1,2,18] as well as the problem of over-rotation [21,22,94]. As a result, intense THz fields can only be detected by using thin detection crystals with small EO coefficient, or by pre-attenuating the THz beam intensity before the detection

crystal by adding attenuators [40,57,95]. In addition, the small angle approximation limits the dynamic range of the detection system and due to back reflection, the use of thin detector crystals also reduces the spectral resolution of THz-TDS.

Here, in the case of elliptically polarized THz-TDS, it becomes much more difficult to control the detection system. For these experiments involving elliptical or circular THz polarization, one has to rotate manually a wire-grid polarizer for the detection of two orthogonal components and to optimize the orientation of the detection crystal [96-100]. This is very challenging to maintain an accurate and stable shot-to-shot measurement, because one complete group of measurements needs both the  $E_{ref}(t)$  and  $E_{trans}(t)$ , which includes 4 measurements with manually rotating the optical elements.

In fact, to solve this problem, various approaches have been proposed for the measurement of the polarization state of the THz wave [20,101-107]. However, most of the techniques require the rotation of various optical elements or have only been demonstrated at relatively low THz fields. This motivates us to develop a new technique that can resolve all the issues and can be used to detect intense elliptically polarized THz pulses.

Here, we propose and demonstrate a new technique that takes into account the complete polarization variation of the probe optical beam. As shown in Section 2.3, we describe the polarization of light using the more general Stokes-Mueller formalism. The Stokes vector provides a complete description of the polarization state of an electromagnetic wave, and the measurement of different combinations of Stokes parameters provides different information on the THz waves. Our technique is easy to implement, has ultrahigh dynamic range since it is not limited by the small-angle approximation or over-rotation, and can also measure not just the amplitude but the polarization direction of the THz field, all as a function of space and time. A real-time self-

referenced imaging of THz electric field vector can also be realized by using a camera to detect the optical probe beam with a spot size larger than that of the THz beam [94].

For general purposes, we develop the technique using the four Stokes parameters here, which eventually allows a self-referenced measurement [94]. In practice, three components are sufficient for the characterization of an intense elliptically polarized THz pulse.

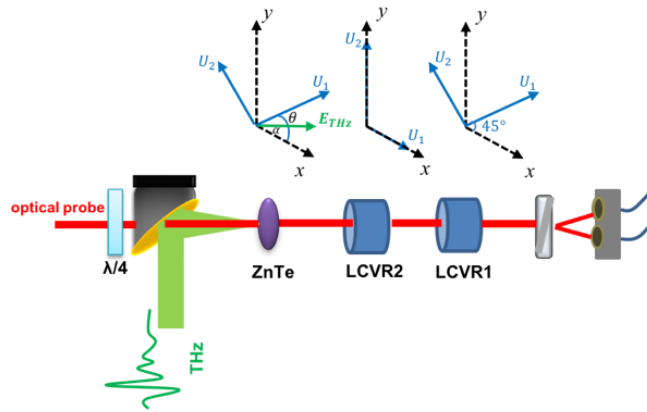


**Fig.7.4: Schematic diagram of the detection system with a polarization state analyzer (PSA), which is composed of two liquid crystal variable retarders (LCVR) and one Wollaston prism.**

As shown in Fig. 7.4, a circularly polarized probe beam is used rather than a linearly polarized one. When the THz polarization starts to rotate, the induced refractive-index axes may end up along the polarization orientation of the linearly polarized probe beam, giving rise to a false zero amplitude. The Stokes vector of a right circularly polarized probe beam can be described by [108]:

$$S_{in} = \begin{pmatrix} 1 \\ 0 \\ 0 \\ 1 \end{pmatrix} \quad (7.1)$$

Here, we write the Mueller matrix of a rotated waveplate to describe the nonlinear detection crystal:

$$M_{EO} = \begin{pmatrix} 1 & 0 & 0 & 0 \\ 0 & \cos^2 2\theta + \cos\phi \sin^2 2\theta & (1 - \cos\phi) \sin 2\theta \cos 2\theta & \sin\phi \sin 2\theta \\ 0 & (1 - \cos\phi) \sin 2\theta \cos 2\theta & \sin^2 2\theta + \cos\phi \cos^2 2\theta & -\sin\phi \cos 2\theta \\ 0 & -\sin\phi \sin 2\theta & \sin\phi \cos 2\theta & \cos\phi \end{pmatrix} \quad (7.2)$$

After transmitted through the detection crystal, the Stokes vector becomes:

$$S_{THz} = \begin{pmatrix} S_0 \\ S_1 \\ S_2 \\ S_3 \end{pmatrix} = \begin{pmatrix} 1 \\ \sin\phi \sin 2\theta \\ -\sin\phi \cos 2\theta \\ \cos\phi \end{pmatrix} = M_{EO} * S_{in} \quad (7.3)$$

Here,  $\phi$  is the phase retardation induced by the THz field and  $\theta$  is the rotation angle of the induced refractive-index axes due to the variation of THz polarization orientation  $\alpha$ . As shown in Fig. 7.4, the x-axis of the laboratory frame is along the [-110] direction of the (110)-orientated ZnTe crystal. For clarity, we rewrite the equations for phase delays and THz polarization orientation here. The delay phase  $\phi$  for a (110) zinc blend nonlinear crystal such as ZnTe can then be described by [20,109]:

$$\phi = \frac{\omega_0 d}{2c} n_0^3 r_{41} E_{THz} \sqrt{1 + 3\cos^2 \alpha} \quad (7.4)$$

and the orientation  $\theta$  of the refractive-index axis can be calculated by:

$$\cos\theta = \sin\alpha / \sqrt{1 + 3\cos^2 \alpha} \quad (7.5)$$

Therefore, by measuring the four elements in  $S_{THz}$  of equation (7.3), we obtain the THz electric field  $E_{THz}$  as well as the polarization orientation  $\alpha$  by using equation (7.4) and (7.5). This can be realized by using the technique of Stokes-Mueller polarimetry [108]. A polarization state analyzer (PSA) is used here, which is composed of two liquid crystal variable retarders (LCVR) (LVR100, Meadowlarks Optics) and one Wollaston prism for balanced detection.

Since only the total intensity  $S_0$  is observable in the Stokes vector, four intensity measurements are needed and a  $4 \times 4$  matrix  $M_{measure}$  is constructed by the first rows of four different Mueller matrices generated by the PSA.

$$\begin{pmatrix} I_0 \\ I_1 \\ I_2 \\ I_3 \end{pmatrix} = M_{measure} * S_{THz} \quad (7.6)$$

Here, to maximize the condition number of this matrix to perform the inverse calculation, we use two LCVRs to generate four independent Stokes vectors that can form a regular tetrahedron on the Poincaré sphere [110,111]. Both LCVRs have been calibrated for the wavelength of the probe beam (800 nm). The orientations of the principal axis are chosen to be  $45^\circ$  and  $0^\circ$  for LCVR1 and LCVR2. The four groups of phase delays we used for LCVR1 and LCVR2 are  $(91.4^\circ, 92.3^\circ)$ ,  $(-20^\circ, 108^\circ)$ ,  $(207.6^\circ, 126^\circ)$  and  $(63.3^\circ, -19.6^\circ)$ , which then generate the measurement matrix  $M_{measure}$ . Since the probe laser intensity is extremely low, the heating effect on the liquid crystal is negligible and the property of the LCVR has shown no sign of variation for a whole day measurement.

To preserve a good signal-to-noise ratio (SNR) comparable to the conventional EO sampling technique, we use a balanced detection configuration as the conventional EO sampling technique, and the differential signal is measured by a lock-in amplifier. As a result, the first element  $S_0$  of the obtained differential vector  $S_{THz}$  becomes zero and  $S_3$  is proportional to the change of  $\cos\phi$  away from 1 at  $\phi = 0^\circ$ .

To demonstrate our new technique under different experimental conditions, we tested it with three different photoconductive antenna THz sources: (i) a conventional THz source pumped by a femtosecond oscillator, (ii) an intense THz source with linear polarization ( $\approx 65 \text{ kV/cm}$ ) and (iii)

an intense quarter-cycle elliptically polarized THz source. We use the same 1 mm (110) ZnTe detection crystal for all the experiments.

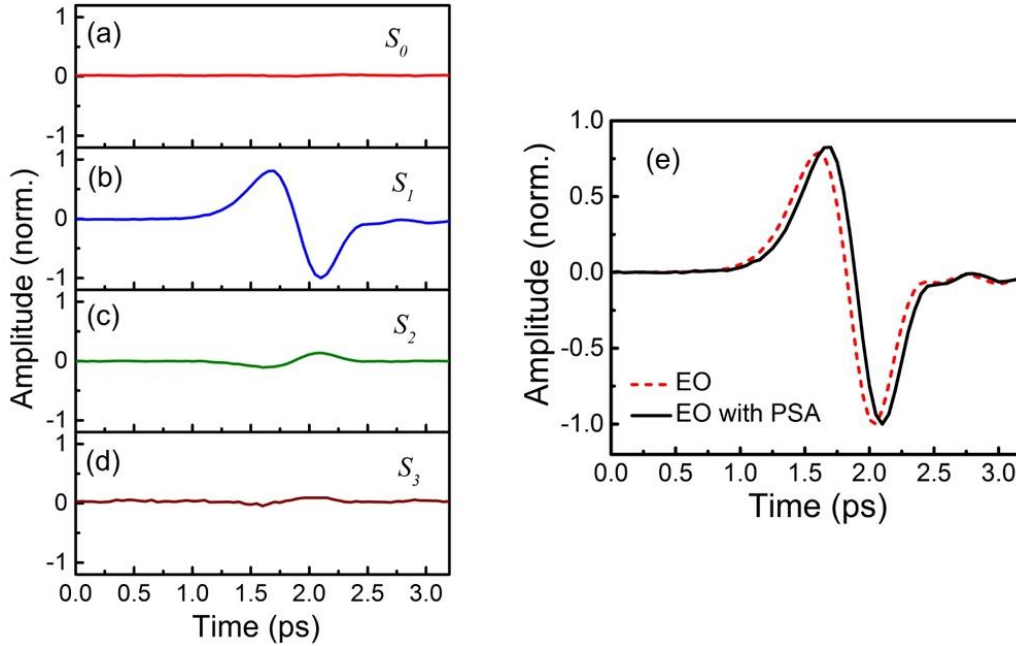


**Fig.7.5: Temporal Stokes parameters of the probe beam (a)  $S_0$ , (b)  $S_1$ , (c)  $S_2$ , and (d)  $S_3$ . (e) The extracted THz signals by using the system with a PSA and by using the conventional EO sampling technique.**

For the first experiment, the THz pulse is generated by a photoconductive antenna with silver paint electrodes, which is pumped by a 70 fs, 0.5 W Ti: Sapphire oscillator. The distance between the two electrodes are 600  $\mu\text{m}$ . The applied DC voltage on the antenna is 50V. Fig. 7.5 (a) to (d) show the measured four Stokes parameters  $S_0$ ,  $S_1$ ,  $S_2$  and  $S_3$ . As expected, a constant signal with 0 amplitude is observed for  $S_0$ . The THz induced birefringence is then measured by  $S_1$ . As shown in Fig. 7.5 (e), the obtained THz curve from EO sampling is similar to the measured  $\sin\phi$  of  $S_1$ , which is in accordance with the small angle approximation [1,2,18]. Here, a weak signal with

opposite polarity of  $S_1$  is observed on  $S_2$ . This can be induced by the orientation discrepancy between the THz polarization orientation and the crystallographic axis of ZnTe. Since the THz polarization orientation does not change, this experimental error can be easily removed by comparing the peak of  $S_1$  and  $S_2$ . Here, the variation of  $\cos\phi$  from 1 is measured by  $S_3$ . Since the cosine function varies slowly at small angles, the amplitude of  $S_3$  is relatively small and close to the noise reference level, as is  $S_0$ . By comparing the amplitude of  $S_1$  and  $S_3$  at 2.2 ps, we obtain a peak electric field of less than 1 kV/cm. Even though this value can only be used as a rough estimate due to the limitation of the SNR of  $S_3$ , this direct measurement of THz electric field is not accessible here by using other techniques such as conventional EO sampling. As can be seen from the comparison between the obtained THz signals in Fig. 7.5 (e), our technique can measure oscillator-pumped weak THz pulses equally well as the normal EO sampling technique.

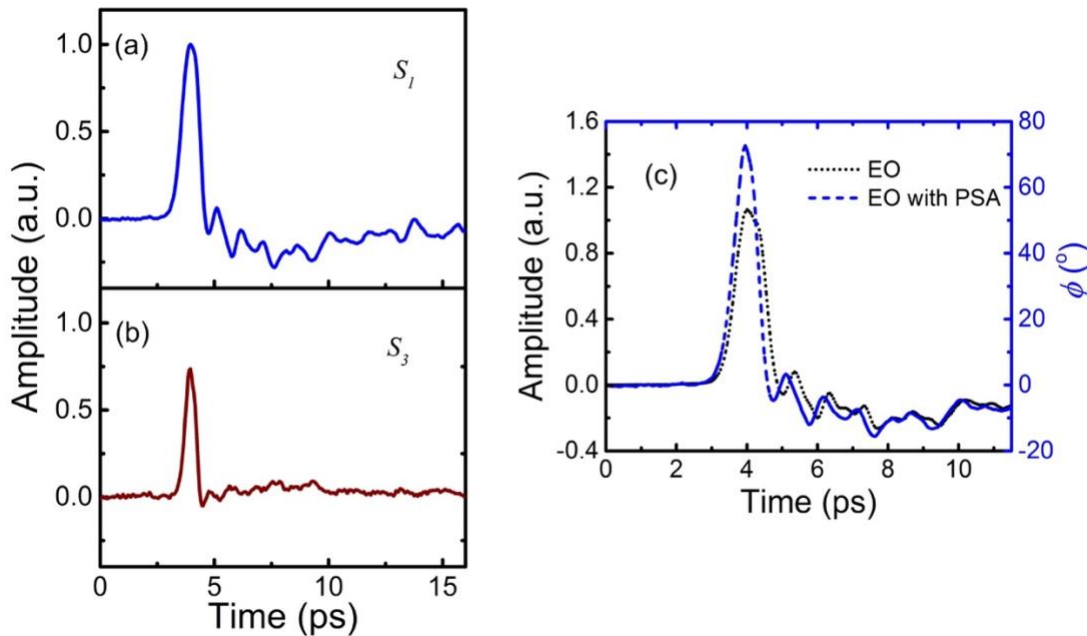


**Fig.7.6: Temporal Stokes parameters of the probe beam (a)  $S_1$ , and (b)  $S_3$ . (c) Measured THz signals by using the system with a PSA and by using the conventional EO sampling technique.**

Next, we tested our technique in a THz-TDS system with an intense THz source. For the experiment of detecting intense THz pulses that are linearly polarized, we place a wire-grid THz polarizer after the ILAPCA and perform the measurement using our detection technique.

Fig. 7.6 shows the experimental results using our technique, and a comparison with the EO sampling technique. Here, the measured signals of  $S_1$  and  $S_3$  are sufficient to reveal the intense THz signal with a high dynamic range, with the ultimate limitation being the detection crystal itself [112]. Atomically strong electric fields may lead to the generation of charge carriers via Zener tunneling and in turn completely change the detection probe signal [112]. As shown in Fig. 7.6 (a) and (b), the low-field and high-field details are retrieved precisely from  $S_1$  and  $S_3$ , respectively. On the other hand, the small-angle approximation used in EO sampling is no longer valid for large phase modulation induced by intense THz fields [1,2,18], which leads to the signal gradually saturating, as shown in Fig. 7.6 (c). Moreover, higher fields may cause the problem of over-rotation, which eventually limits the maximum detection range to a quarter-cycle phase retardation [21,22,94]. Here, by measuring  $\cos\phi$  simultaneously, we can calculate directly the peak phase retardation  $\phi$ , which is approximately  $72^\circ$ , which is equivalent to an electric field of 64.3 kV/cm. To verify this value, we measured the THz electric field by performing conventional EO sampling using a  $300\ \mu\text{m}$  (110) GaP crystal and obtain a field strength of 61 kV/cm [18].

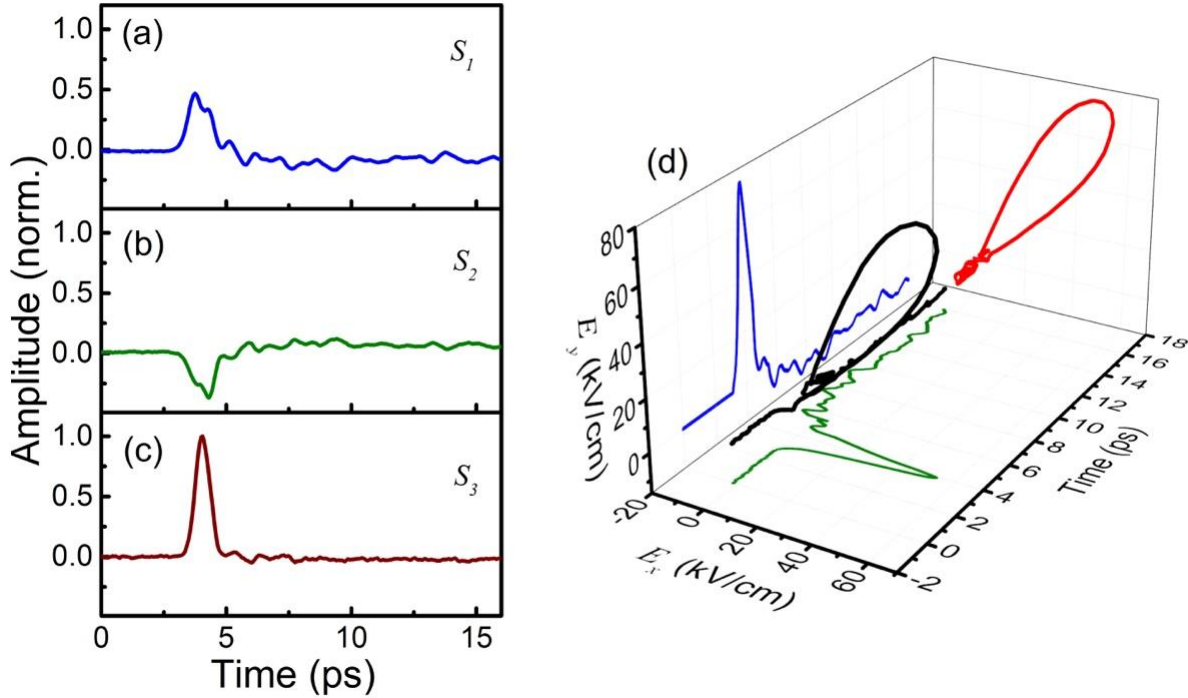


**Fig.7.7: Temporal Stokes parameters of the probe beam (a)  $S_1$ , (b)  $S_2$ , and (c)  $S_3$ . (d) Measured 3D THz waveform.**

To demonstrate the THz-polarization sensitive detection, we then removed the wire-grid polarizer and performed the experiment using our detection system. To generate a quarter-cycle elliptically polarized THz pulse, we used a delay mask with a thickness of 0.12 mm, which leads to a time delay of approximately 200 fs between the peaks of the horizontal ( $E_x$ ) and the vertical ( $E_y$ ) THz waveforms. Here, conventional EO sampling technique is no longer applicable in a single measurement limit and the 3D THz waveforms can only be obtained by measuring the polarization variation of the probe beam via Jones calculus or Stokes-Mueller calculus used here [20,103,109].

In Fig. 7.7, we show the measured three Stokes parameters  $S_1$ ,  $S_2$  and  $S_3$ . In practice,  $S_1$  and  $S_2$  are sufficient for the detection of elliptically polarized THz pulses with low fields. However, at

high fields, it is also necessary to measure  $S_3$ , because the change of polarization orientation may affect similarly on the signal of  $\sin\phi$  as that from saturation or over-rotation. The rotation of the refractive-index axis  $\theta$  is calculated from  $S_1$  and  $S_2$  and then the THz field orientation  $\alpha$  can be obtained by using equation (4). Fig. 7.7 (d) shows the measured 3D THz waveform, where the maximum is reached at 4.05 ps, corresponding to an electric field of 89.5 kV/cm and a polarization orientation  $\alpha$  of  $54^\circ$ . Here, the field induced phase delay  $\phi$  already exceeds  $90^\circ$  and as a result the correct value of  $\phi$  can only be retrieved by measuring both  $S_1$  and  $S_3$ , because  $\sin\phi$  starts to decrease for over-rotated  $\phi$  above  $90^\circ$ .

As demonstrated by the three measurements, one of the advantages of the current system is that it can be used for different experimental purposes. When using a lock-in amplifier, the measurement of  $S_0$  is not necessary. However, it can always be used as a reference signal, which eventually allows a self-referenced THz measurement by using thicker crystals [22,94]. By measuring both  $S_1$  ( $\cos\phi$ ) and  $S_3$  ( $\sin\phi$ ), the over-rotation problem (signal reduction for  $\sin\phi$  when  $\phi$  is higher than  $90^\circ$ ) that exists in conventional EO sampling technique is solved naturally. Furthermore, the same sensitivity is preserved for both low and high fields, because high signal gains are alternatively provided by sine and cosine signals measured by  $S_1$  and  $S_3$ . By adding the information of  $S_2$ , we can measure the THz polarization variation as well.

In summary, we have proposed and demonstrated a new EO sampling configuration that is simple and effective for the coherent detection of intense THz waves with any polarization state. The novel voltage controllable polarization modulators, such as LCVR, enables a complete polarization measurement of the probe beam without mechanical rotation of any optical elements [103,105]. Moreover, our technique can operate under multiple modes to fulfill different experimental requirements.

## Chapter 8

### Conclusions and Perspectives

In this thesis, we studied the effect of the nonlinear carrier dynamics on subcycle nonlinear THz optics. In particular, taking into account the temporal dynamics is highly essential for a clear observation of nonlinear effects. Compared with the techniques used in other electromagnetic frequency range, THz-TDS is much more powerful because it can provide a straightforward picture of the nonlinear phenomena by measuring the THz temporal profile. Here, the instantaneous THz conductivity determines the nonlinear interaction between THz waves and doped semiconductor material in time. The nonlinear intraband conductivity can be induced by either coherent approach via non-parabolic band dispersion or Bloch oscillation, or via incoherent scattering effects.

For both graphene and semiconductor  $\text{In}_{0.53}\text{Ga}_{0.47}\text{As}$ , the THz responses are determined by the number of charge carriers that interact with the THz radiation as well as the scattering rates driven at high fields. In Chapter 3, we have studied both the impact of carrier density as well as the scattering rate on the THz responses of graphene. We have demonstrated that graphene is extremely sensitive to the ambient temperature and a temperature increase may lead to the desorption of water and oxygen molecules from the surface of graphene, which will eventually increase the electron doping. A crossover from transmission reduction to transmission enhancement has been observed by performing OPTP spectroscopy, suggesting that graphene can be used in thermal switching and sensing applications. However, since graphene is very sensitive to the ambient temperature effects, the use of graphene in some applications that require high stability is strongly limited. We then discussed the nonlinear carrier dynamics in gated-graphene

using THz-TDS. The increased THz field will increase the total scattering rate and in turn gives rise to the THz transmission enhancement. However, clear subcycle THz nonlinear optics has not been observed, which is due to the high center frequency (around 0.8 THz) of the LiNbO<sub>3</sub> source and the fewer charge carrier compared with the heavily doped In<sub>0.53</sub>Ga<sub>0.47</sub>As semiconductor thin film.

In Chapter 4, we discussed the limitations of the Drude model and demonstrated that it is essential to take into account the nonlinear temporal dynamics for the analysis of the high field responses of charge carrier dynamics. We then introduced the ensemble Monte-Carlo approach to calculate the transient response of charge carrier dynamics. In this model, the scattering rates are calculated directly using the Fermi's Golden Rule at different carrier momenta, which allows us to retrieve the transient temporal dynamics without using any fitting parameter. In Chapter 5, we have demonstrated experimentally and theoretically the subcycle THz nonlinear optics using the intraband carrier dynamics in semiconductor In<sub>0.53</sub>Ga<sub>0.47</sub>As using the low peak frequency (0.15 THz) LAPCA THz source. We have observed the half-cycle THz pulses truncation after transmission and the generation of a continuous high frequency band up to 2.2 THz. HHG is predicted theoretically when multi-cycle pulses are used.

By increasing the applied THz field strength to a few MV/cm, a transition from intraband to interband carrier dynamics is observed. In the current study, we performed a direct energy measurement of the whole THz beam without measuring the THz waveforms. For future plans, a time-resolved measurement is required to fully reveal the effect of interband transitions on the subcycle nonlinear THz optics as we discussed in Chapter 5. Depending on the interplay between intraband carrier heating and interband carrier generation, we could actively control the transmitted THz spectra by varying the incident field strength and THz waveforms.

In addition to doped  $\text{In}_{0.53}\text{Ga}_{0.47}\text{As}$ , other semiconductor that possess lower band gap can also be a good system to study the impact of both inter- and intraband carrier dynamics on the subcycle THz nonlinear optics. By changing the applied THz electric field, the high order harmonic feature might be altered by controlling the interplay between intraband heating and interband carrier generation. For example, the InSb semiconductor possess a small band gap of 0.17 eV and effective mass ratio of 0.014. Both impact ionization and Zener tunneling effect could take place without the interference by the intervalley scattering effect.

Subcycle nonlinear THz optics induced by the intervalley scattering effects in doped  $\text{In}_{0.53}\text{Ga}_{0.47}\text{As}$  thin film shows a low field transmission of 5% at low fields and a much higher transmission of 86% at high fields, which suggests that it can be used a broadband THz saturable absorber for applications of ultrafast THz optics.

Compared with electronics, the effect of THz polarization is also of great interest to investigate, which may lead to the observation of new effects. Further experimental as well as theoretical work is needed to understand the carrier dynamics driven by elliptically rotating THz field vectors.

We anticipate that our findings will be important for future optoelectronic applications and contribute to the advancement of THz photonics.

## References

1. Y.-S. Lee, *Principles of Terahertz Science and Technology* (Springer Science Business Media **170**, 2009).
2. X. C. Zhang, *Introduction to THz Wave Photonics* (New York Springer **29**, 2010).
3. T. Kampfrath, K. Tanaka, and K. A. Nelson, "Resonant and nonresonant control over matter and light by intense terahertz transients," *Nat. Photon.* **7**, 680 (2013).
4. H. A. Hafez, X. Chai, A. Ibrahim, S. Mondal, D. Férachou, X. Ropagnol, and T. Ozaki, "Intense terahertz radiation and their applications," *Journal of Optics* **18**, 093004 (2016).
5. R. Ulbricht, E. Hendry, J. Shan, T. F. Heinz, and M. Bonn, "Carrier dynamics in semiconductors studied with time-resolved terahertz spectroscopy," *Rev. Mod. Phys.* **83**, 543 (2011).
6. P. U. Jepsen, D. G. Cooke, and M. Koch, "Terahertz spectroscopy and imaging - Modern techniques and applications," *Laser & Photon. Rev.* **5**, 124 (2011).
7. F. Blanchard, L. Razzari, H. C. Bandulet, G. Sharma, R. Morandotti, J. C. Kieffer, T. Ozaki, M. Reid, H. F. Tiedje, H. K. Haugen, and F. A. Hegmann, "Generation of 1.5  $\mu\text{J}$  single-cycle terahertz pulses by optical rectification from a large aperture ZnTe crystal," *Opt. Express* **15**, 13212 (2007).
8. F. Blanchard, G. Sharma, X. Ropagnol, L. Razzari, R. Morandotti, and T. Ozaki, "Improved terahertz two-color plasma sources pumped by high intensity laser beam," *Opt. Express* **17**, 6044 (2009).
9. F. Blanchard, G. Sharma, L. Razzari, X. Ropagnol, H.-C. Bandulet, F. Vidal, R. Morandotti, J.-C. Kieffer, T. Ozaki, H. Tiedje, H. Haugen, M. Reid, and F. Hegmann,

- "Generation of Intense Terahertz Radiation via Optical Methods," *IEEE J. Select. Topics Quantum Electron.* **17**, 5 (2011).
10. X. Ropagnol, R. Morandotti, T. Ozaki, and M. Reid, "THz pulse shaping and improved optical-to-THz conversion efficiency using a binary phase mask," *Opt. Lett.* **36**, 2662 (2011).
  11. X. Ropagnol, F. Blanchard, T. Ozaki, and M. Reid, "Intense terahertz generation at low frequencies using an interdigitated ZnSe large aperture photoconductive antenna," *Appl. Phys. Lett.* **103**, 161108 (2013).
  12. F. Blanchard, X. Ropagnol, H. Hafez, H. Razavipour, M. Bolduc, R. Morandotti, T. Ozaki, and D. G. Cooke, "Effect of extreme pump pulse reshaping on intense terahertz emission in lithium niobate at multimillijoule pump energies," *Opt. Lett.* **39**, 4333 (2014).
  13. X. Ropagnol, M. Khorasaninejad, M. Raeiszadeh, S. Safavi-Naeini, M. Bouvier, C. Y. Côté, A. Laramée, M. Reid, M. A. Gauthier, and T. Ozaki, "Intense THz Pulses with large ponderomotive potential generated from large aperture photoconductive antennas," *Opt. Express* **24**, 11299 (2016).
  14. S. Mondal, H. A. Hafez, X. Ropagnol, and T. Ozaki, "MV/cm terahertz pulses from relativistic laser-plasma interaction characterized by nonlinear terahertz absorption bleaching in n-doped InGaAs," *Opt. Express* **25**, 17511 (2017).
  15. K. Reimann, "Table-top sources of ultrashort THz pulses," *Rep. Prog. Phys.* **70**, 1597 (2007).
  16. S. Ono, H. Murakami, A. Quema, G. Diwa, N. Sarukura, R. Nagasaka, Y. Ichikawa, H. Ogino, E. Ohshima, A. Yoshikawa, and T. Fukuda, "Generation of terahertz radiation

- using zinc oxide as photoconductive material excited by ultraviolet pulses," *Appl. Phys. Lett.* **87**, 261112 (2005).
17. O. Imafuji, B. P. Singh, Y. Hirose, Y. Fukushima, and S. Takigawa, "High power subterahertz electromagnetic wave radiation from GaN photoconductive switch," *Appl. Phys. Lett.* **91**, 071112 (2007).
  18. Q. Wu and X. C. Zhang, "Free-space electro-optic sampling of terahertz beams," *Appl. Phys. Lett.* **67**, 3523 (1995).
  19. E. Collett, *Field Guide to Polarization* (SPIE press Vol. 15, 2005),".
  20. N. Yasumatsu and S. Watanabe, "Precise real-time polarization measurement of terahertz electromagnetic waves by a spinning electro-optic sensor," *Rev. Sci. Instrum.* **83**, 023104 (2012).
  21. G. Sharma, K. Singh, I. Al-Naib, R. Morandotti, and T. Ozaki, "Terahertz detection using spectral domain interferometry," *Opt. Lett.* **37**, 4338 (2012).
  22. A. Ibrahim, D. Ferachou, G. Sharma, K. Singh, M. Kirouac-Turmel, and T. Ozaki, "Ultra-high dynamic range electro- optic sampling for detecting millimeter and sub-millimeter radiation," *Sci. Rep.* **6**, 23107 (2016).
  23. M. C. Nuss and J. Orenstein, in *Millimeter and Submillimeter Wave Spectroscopy of Solids* (Springer-Verlag, Berlin, Germany, 1998), pp. 7-43.
  24. K. S. Novoselov, "Electric Field Effect in Atomically Thin Carbon Films," *Science* **306**, 666 (2004).
  25. S. Das Sarma, S. Adam, E. H. Hwang, and E. Rossi, "Electronic transport in two-dimensional graphene," *Rev. Mod. Phys.* **83**, 407 (2011).

26. K. L. Ishikawa, "Nonlinear optical response of graphene in time domain," *Phys. Rev. B* **82**, 201402 (2010).
27. I. Al-Naib, M. Poschmann, and M. M. Dignam, "Optimizing third-harmonic generation at terahertz frequencies in graphene," *Phys. Rev. B* **91**, 205407 (2015).
28. I. Al-Naib, J. E. Sipe, and M. M. Dignam, "High harmonic generation in undoped graphene: Interplay of inter- and intraband dynamics," *Phys. Rev. B* **90**, 245423 (2014).
29. F. Schedin, A. K. Geim, S. V. Morozov, E. W. Hill, P. Blake, M. I. Katsnelson, and K. S. Novoselov, "Detection of individual gas molecules adsorbed on graphene," *Nat. Mat.* **6**, 652 (2007).
30. E. H. Hwang and S. Das Sarma, "Acoustic phonon scattering limited carrier mobility in two-dimensional extrinsic graphene," *Phys. Rev. B* **77**, 115449 (2008).
31. S. Fratini and F. Guinea, "Substrate-limited electron dynamics in graphene," *Phys. Rev. B* **77**, 195415 (2008).
32. V. Perebeinos and P. Avouris, "Inelastic scattering and current saturation in graphene," *Phys. Rev. B* **81**, 195442 (2010).
33. C. J. Docherty, C.-T. Lin, H. J. Joyce, R. J. Nicholas, L. M. Herz, L.-J. Li, and M. B. Johnston, "Extreme sensitivity of graphene photoconductivity to environmental gases," *Nat. Commun.* **3**, 2235 (2012).
34. L. Ren, Q. Zhang, J. Yao, Z. Sun, R. Kaneko, Z. Yan, S. Nanot, Z. Jin, I. Kawayama, M. Tonouchi, J. M. Tour, and J. Kono, "Terahertz and Infrared Spectroscopy of Gated Large-Area Graphene," *Nano Lett.* **12**, 3711 (2012).

35. G. Jnawali, Y. Rao, H. Yan, and T. F. Heinz, "Observation of a Transient Decrease in Terahertz Conductivity of Single-Layer Graphene Induced by Ultrafast Optical Excitation," *Nano Lett.* **13**, 524 (2013).
36. K. J. Tielrooij, J. C. W. Song, S. A. Jensen, A. Centeno, A. Pesquera, A. Zurutuza Elorza, M. Bonn, L. S. Levitov, and F. H. L. Koppens, "Photoexcitation cascade and multiple hot-carrier generation in graphene," *Nat. Phys.* **9**, 248 (2013).
37. S. F. Shi, T. T. Tang, B. Zeng, L. Ju, Q. Zhou, A. Zettl, and F. Wang, "Controlling Graphene Ultrafast Hot Carrier Response from Metal-like to Semiconductor-like by Electrostatic Gating," *Nano Lett.* **14**, 1578 (2014).
38. A. J. Frenzel, C. H. Lui, Y. C. Shin, J. Kong, and N. Gedik, "Semiconducting-to-Metallic Photoconductivity Crossover and Temperature-Dependent Drude Weight in Graphene," *Phys. Rev. Lett.* **113**, 056602 (2014).
39. H. A. Hafez, I. Al-Naib, M. M. Dignam, Y. Sekine, K. Oguri, F. Blanchard, D. G. Cooke, S. Tanaka, F. Komori, H. Hibino, and T. Ozaki, "Nonlinear terahertz field-induced carrier dynamics in photoexcited epitaxial monolayer graphene," *Phys. Rev. B* **91**, 035422 (2015).
40. H. Razavipour, W. Yang, A. Guermoune, M. Hilke, D. G. Cooke, I. Al-Naib, M. M. Dignam, F. Blanchard, H. A. Hafez, X. Chai, D. Ferachou, T. Ozaki, P. L. Lévesque, and R. Martel, "High-field response of gated graphene at terahertz frequencies," *Phys. Rev. B* **92**, 245421 (2015).
41. H. A. Hafez, X. Chai, Y. Sekine, M. Takamura, K. Oguri, I. Al-Naib, M. M. Dignam, H. Hibino, and T. Ozaki, "Effects of environmental conditions on the ultrafast carrier dynamics in graphene revealed by terahertz spectroscopy," *Phys. Rev. B* **95**, 165428 (2017).

42. C. H. Lui, K. F. Mak, J. Shan, and T. F. Heinz, "Ultrafast Photoluminescence from Graphene," *Phys. Rev. Lett.* **105**, 127404 (2010).
43. F. Wang, Y. Zhang, C. Tian, C. Girit, A. Zettl, M. Crommie, and Y. R. Shen, "Gate-variable optical transitions in graphene," *Science* **320**, 206 (2008).
44. Z. Q. Li, E. A. Henriksen, Z. Jiang, Z. Hao, M. C. Martin, P. Kim, H. L. Stormer, and D. N. Basov, "Dirac charge dynamics in graphene by infrared spectroscopy," *Nat. Phys.* **4**, 532 (2008).
45. M. M. Glazov and S. D. Ganichev, "High frequency electric field induced nonlinear effects in graphene," *Phys. Rep.* **535**, 101 (2014).
46. H. A. Hafez, I. Al-Naib, K. Oguri, Y. Sekine, M. M. Dignam, A. Ibrahim, D. G. Cooke, S. Tanaka, F. Komori, H. Hibino, and T. Ozaki, "Nonlinear transmission of an intense terahertz field through monolayer graphene," *AIP Advances* **4**, 117118 (2014).
47. H. A. Hafez, P. L. Lévesque, I. Al-Naib, M. M. Dignam, X. Chai, S. Choubak, P. Desjardins, R. Martel, and T. Ozaki, "Intense terahertz field effects on photoexcited carrier dynamics in gated graphene," *Appl. Phys. Lett.* **107**, 251903 (2015).
48. A. J. Frenzel, C. H. Lui, Y. C. Shin, J. Kong, and N. Gedik, "Semiconducting-to-Metallic Photoconductivity Crossover and Temperature-Dependent Drude Weight in Graphene," *Phys. Rev. Lett.* **113**, 056602 (2014).
49. R. W. Boyd, *Nonlinear Optics* (Elsevier, 2008).
50. L. Razzari, F. H. Su, G. Sharma, F. Blanchard, A. Ayesheshim, H. C. Bandulet, R. Morandotti, J. C. Kieffer, T. Ozaki, M. Reid, and F. A. Hegmann, "Nonlinear ultrafast modulation of the optical absorption of intense few-cycle terahertz pulses in n-doped semiconductors," *Phys. Rev. B* **79**, 193204 (2009).

51. F. H. Su, F. Blanchard, G. Sharma, L. Razzari, A. Ayesheshim, T. L. Cocker, L. V. Titova, T. Ozaki, J. C. Kieffer, R. Marandotti, M. Reid, and F. Hegmann, "Terahertz pulse induced intervalley scattering in photoexcited GaAs," *Opt. Express* **17**, 9620 (2009).
52. M. C. Hoffmann and D. Turchinovich, "Semiconductor saturable absorbers for ultrafast terahertz signals," *Appl. Phys. Lett.* **96**, 151110 (2010).
53. D. Turchinovich, J. M. Hvam, and M. C. Hoffmann, "Self-phase modulation of a single-cycle terahertz pulse by nonlinear free-carrier response in a semiconductor," *Phys. Rev. B* **85**, 201304 (2012).
54. M. Lundstrom, *Fundamentals of Carrier Transport* (Cambridge University Press, 2009).
55. T. N. K. Phan, K. Kato, G. Isoyama, M. Yoshimura, S. Fujioka, and M. Nakajima, "Third harmonic generation from InSb excited by Free Electron Laser, 43rd International Conference on Infrared, Millimeter, and Terahertz Waves (IRMMW-THz) (2018).
56. S. Ghimire, A. D. DiChiara, E. Sistrunk, P. Agostini, L. F. DiMauro, and D. A. Reis, "Observation of high-order harmonic generation in a bulk crystal," *Nat. Phys.* **7**, 138(2010).
57. O. Schubert, M. Hohenleutner, F. Langer, B. Urbanek, C. Lange, U. Huttner, D. Golde, T. Meier, M. Kira, S. W. Koch, and R. Huber, "Sub-cycle control of terahertz high-harmonic generation by dynamical Bloch oscillations," *Nat. Photon.* **8**, 119 (2014).
58. M. Wegener, *Extreme Nonlinear Optics: an Introduction* (Springer Science & Business Media, 2005).
59. T. T. Luu, M. Garg, S. Y. Kruchinin, A. Moulet, M. T. Hassan, and E. Goulielmakis, "Extreme ultraviolet high-harmonic spectroscopy of solids," *Nature* **521**, 498 (2015).

60. M. Hohenleutner, F. Langer, O. Schubert, M. Knorr, U. Huttner, S. W. Koch, M. Kira, and R. Huber, "Real-time observation of interfering crystal electrons in high-harmonic generation," *Nature* **523**, 572 (2015).
61. F. Langer, M. Hohenleutner, C. P. Schmid, C. Poellmann, P. Nagler, T. Korn, C. Schüller, M. S. Sherwin, U. Huttner, J. T. Steiner, S. W. Koch, M. Kira, and R. Huber, "Lightwave-driven quasiparticle collisions on a subcycle timescale," *Nature* **533**, 225 (2016).
62. Y. S. You, D. A. Reis, and S. Ghimire, "Anisotropic high-harmonic generation in bulk crystals," *Nat. Phys.* **13**, 345 (2016).
63. H. Liu, Y. Li, Y. S. You, S. Ghimire, T. F. Heinz, and D. A. Reis, "High-harmonic generation from an atomically thin semiconductor," *Nat. Phys.* **13**, 262 (2016).
64. N. Yoshikawa, T. Tamaya, and K. Tanaka, "High-harmonic generation in graphene enhanced by elliptically polarized light excitation," *Science* **356**, 736 (2017).
65. G. Sharma, I. Al-Naib, H. Hafez, R. Morandotti, D. G. Cooke, and T. Ozaki, "Carrier density dependence of the nonlinear absorption of intense THz radiation in GaAs," *Opt. Express* **20**, 18016 (2012).
66. M. Asche, C. Canali, E. Constant, K. Hess, G. J. Iafrate, S. Komijama, T. Kurosawa, T. Masumi, F. Nava, and Y. K. Pozhela, *Hot-Electron Transport in Semiconductors* (Springer Science & Business Media, 2006), Vol. 58.
67. H. A. Hafez, S. Kovalev, J.-C. Deinert, Z. X. N. Mics, B. Green, N. Awari, M. Chen, S. Germanskiy, U. Lehnert, J. Teichert, Z. Wang, K.-J. Tielrooij, Z. Liu, Z. Chen, A. Narita, K. M. X. Ilen, M. Bonn, M. Gensch, and D. Turchinovich, "Extremely efficient terahertz high-harmonic generation in graphene by hot Dirac fermions," *Nature* **561**, 507 (2018).

68. M. Mohamed, A. Bharthuar, and U. Ravaioli, *Bulk GaAs Ensemble Monte Carlo*, DOI: 10.4231/D38C9R505 (2015).
69. C. Jacoboni and L. Reggiani, "The Monte Carlo method for the solution," *Rev. Mod. Phys.* **55**, 645 (1983).
70. A. P. Long, P. H. Beton, and M. J. Kelly, "Hot-electron transport in In<sub>0.53</sub>Ga<sub>0.47</sub>As," *J. Appl. Phys.* **62**, 1842 (1987).
71. W. Kuehn, P. Gaal, K. Reimann, M. Woerner, T. Elsaesser, and R. Hey, "Coherent Ballistic Motion of Electrons in a Periodic Potential," *Phys. Rev. Lett.* **104**, 146602 (2010).
72. K. L V, "Behavior of non-metallic crystal in strong electric fields," *Sov. Phys. JETP* **6**, (1958).
73. M. C. Hoffmann, J. Hebling, H. Y. Hwang, K.-L. Yeh, and K. A. Nelson, "Impact ionization in InSb probed by terahertz pump—terahertz probe spectroscopy," *Phys. Rev. B* **79**, 161201 (2009).
74. H. Hirori, K. Shinokita, M. Shirai, S. Tani, Y. Kadoya, and K. Tanaka, "Extraordinary carrier multiplication gated by a picosecond electric field pulse," *Nat. Commun.* **2**, 594 (2011).
75. K. Fan, H. Y. Hwang, M. Liu, A. C. Strikwerda, A. Sternbach, J. Zhang, X. Zhao, X. Zhang, K. A. Nelson, and R. D. Averitt, "Nonlinear Terahertz Metamaterials via Field-Enhanced Carrier Dynamics in GaAs," *Phys. Rev. Lett.* **110**, 217404 (2013).
76. C. Vicario, A. V. Ovchinnikov, S. I. Ashitkov, M. B. Agranat, V. E. Fortov, and C. P. Hauri, "Generation of 09-mJ THz pulses in DSTMS pumped by a Cr:Mg 2SiO<sub>4</sub> laser," *Opt. Lett.* **39**, 6632 (2014).

77. C. Vicario, B. Monoszlai, and C. P. Hauri, "GV/m Single-Cycle Terahertz Fields from a Laser-Driven Large-Size Partitioned Organic Crystal," *Phys. Rev. Lett.* **112**, 213901 (2014).
78. S. Mondal, H. A. Hafez, X. Ropagnol, and T. Ozaki, "MV/cm terahertz pulses from relativistic laser-plasma interaction characterized by nonlinear terahertz absorption bleaching in n-doped InGaAs," *Opt. Express* **25**, 17511 (2017).
79. O. V. Chefonov, A. V. Ovchinnikov, S. A. Romashevskiy, X. Chai, T. Ozaki, A. B. Savel'ev, M. B. Agranat, and V. E. Fortov, "Giant self-induced transparency of intense few-cycle terahertz pulses in n-doped silicon," *Opt. Lett.* **42**, 4889 (2017).
80. M. Shalaby, C. Vicario, and C. P. Hauri, "High-performing nonlinear visualization of terahertz radiation on a silicon charge-coupled device," *Nat. Commun.* **6**, 8439 (2015).
81. H. Wen, M. Wiczler, and A. M. Lindenberg, "Ultrafast electron cascades in semiconductors driven by intense femtosecond terahertz pulses," *Phys. Rev. B* **78**, 125203 (2008).
82. I.-C. Ho and X. C. Zhang, "Driving intervalley scattering and impact ionization in InAs with intense terahertz pulses," *Appl. Phys. Lett.* **98**, 241908 (2011).
83. W. Kuehn, P. Gaal, K. Reimann, M. Woerner, T. Elsaesser, and R. Hey, "Terahertz-induced interband tunneling of electrons in GaAs," *Phys. Rev. B* **82**, 075204 (2010).
84. K. Shinokita, H. Hirori, K. Tanaka, T. Mochizuki, C. Kim, H. Akiyama, L. N. Pfeiffer, and K. W. West, "Terahertz-Induced Optical Emission of Photoexcited Undoped GaAs Quantum Wells," *Phys. Rev. Lett.* **111**, 067401 (2013).
85. C. Lange, T. Maag, M. Hohenleutner, S. Baierl, O. Schubert, E. R. J. Edwards, D. Bougeard, G. Woltersdorf, and R. Huber, "Extremely Nonperturbative Nonlinearities in

- GaAs Driven by Atomically Strong Terahertz Fields in Gold Metamaterials," *Phys. Rev. Lett.* **113**, 227401 (2014).
86. A. T. Tarekegne, K. Iwaszczuk, M. Zalkovskij, A. C. Strikwerda, and P. U. Jepsen, "Impact ionization in high resistivity silicon induced by an intense terahertz field enhanced by an antenna array," *New J. Phys.* **17**, 043002 (2015).
  87. A. T. Tarekegne, H. Hirori, K. Tanaka, K. Iwaszczuk, and P. U. Jepsen, "Impact ionization dynamics in silicon by MV/cm THz fields," *New J. Phys.* **19**, 123018 (2017).
  88. E. O. Kane, "Zener tunneling in semiconductors," *J. PHYS. CHEM. SOLIDS* **12**, 181 (1959).
  89. K. L. V, "Kinetic theory of impact ionization in semiconductors," *Sov. Phys. JETP* **37**, (1960).
  90. K. Y. Choo and D. S. Ong, "Analytical band Monte Carlo simulation of electron impact ionization in In<sub>0.53</sub>Ga<sub>0.47</sub>As," *J. Appl. Phys.* **96**, 5649 (2004).
  91. F. Blanchard, D. Golde, F. H. Su, L. Razzari, G. Sharma, R. Morandotti, T. Ozaki, M. Reid, M. Kira, S. W. Koch, and F. A. Hegmann, "Effective Mass Anisotropy of Hot Electrons in Nonparabolic Conduction Bands of n-Doped InGaAs Films Using Ultrafast Terahertz Pump-Probe Techniques," *Phys. Rev. Lett.* **107**, 107401 (2011).
  92. X. Ropagnol, X. Chai, M. Raeiszadeh, S. Safavi-Naeini, M. Reid, and T. Ozaki, "Intense THz Source of Sub-Cycle Pulses with Tunable Elliptical Polarization," 43rd International Conference on Infrared, Millimeter, and Terahertz Waves (IRMMW-THz) (2018).
  93. B. B. Hu and M. C. Nuss, "Imaging with terahertz waves," *Opt. Lett.* **20**, 1716 (1995).

94. G. Sharma, K. Singh, A. Ibrahim, I. Al-Naib, R. Morandotti, F. Vidal, and T. Ozaki, "Self-referenced spectral domain interferometry for improved signal-to-noise measurement of terahertz radiation," *Opt. Lett.* **38**, 2705 (2013).
95. X. Chai, X. Ropagnol, S. M. Raeis-Zadeh, M. Reid, S. Safavi-Naeini, and T. Ozaki, "Subcycle Terahertz Nonlinear Optics," *Phys. Rev. Lett.* **121**, 143901 (2018).
96. J. Shan, J. I. Dadap, and T. F. Heinz, "Circularly polarized light in the single-cycle limit: the nature of highly polychromatic radiation of defined polarization," *Opt. Express* **17**, 7431 (2009).
97. G. Yumoto, J. Y. Yoo, R. Matsunaga, S. Tanabe, H. Hibino, T. Morimoto, H. Aoki, and R. Shimano, "Quantum Faraday and Kerr rotations in graphene," *Nat. Communi.* **4**, 1841 (2013).
98. M. Sato, T. Higuchi, N. Kanda, K. Konishi, K. Yoshioka, T. Suzuki, K. Misawa, and M. Kuwata-Gonokami, "Terahertz polarization pulse shaping with arbitrary field control," *Nat. Photon.* **7**, 724 (2013).
99. X. Lu and X. C. Zhang, "Generation of Elliptically Polarized Terahertz Waves from Laser-Induced Plasma with Double Helix Electrodes," *Phys. Rev. Lett.* **108**, 123903 (2012).
100. Z. Zhang, Y. Chen, Sen Cui, F. He, M. Chen, Z. Zhang, J. Yu, L. Chen, Z. Sheng, and J. Zhang, "Manipulation of polarizations for broadband terahertz waves emitted from laser plasma filaments," *Nat. Photon.* **12**, 554 (2018).
101. N. C. J. van der Valk, W. A. M. van der Marel, and P. C. M. Planken, "Terahertz polarization imaging," *Opt. Lett.* **30**, 2802 (2005).

102. T. Nagashima, M. Tani, and M. Hangyo, "Polarization-sensitive THz-TDS and its Application to Anisotropy Sensing," *Journal of Infrared, Millimeter, and Terahertz Waves* **34**, 740 (2013).
103. N. Nemoto, T. Higuchi, N. Kanda, K. Konishi, and M. Kuwata-Gonokami, "Highly precise and accurate terahertz polarization measurements based on electro-optic sampling with polarization modulation of probe pulses," *Opt. Express* **22**, 17915 (2014).
104. M. Takai, M. Takeda, M. Sasaki, T. Tachizaki, N. Yasumatsu, and S. Watanabe, "Video-rate terahertz electric-field vector imaging," *Appl. Phys. Lett.* **105**, 151103 (2014).
105. N. Yasumatsu, A. Kasatani, K. Oguchi, and S. Watanabe, "High-speed terahertz time-domain polarimeter based on an electro-optic modulation technique," *Appl. Phys. Express* **7**, 092401 (2013).
106. Z. Lü, D. Zhang, C. Meng, L. Sun, Z. Zhou, Z. Zhao, and J. Yuan, "Polarization-sensitive air-biased-coherent-detection for terahertz wave," *Appl. Phys. Lett.* **101**, 081119 (2012).
107. K. Oguchi, H. Iwasaki, M. Okano, and S. Watanabe, "Polarization-sensitive electro-optic detection of terahertz wave using three different types of crystal symmetry: Toward broadband polarization spectroscopy," *Appl. Phys. Lett.* **108**, 011105 (2016).
108. N. M. Bashara, *Ellipsometry and Polarized Light* (North Holland, 1987).
109. N. C. J. van der Valk, T. Wenchkebach, and P. C. M. Planken, "Full mathematical description of electro-optic detection in optically isotropic crystals," *JOSA B* **21**, 622 (2004).
110. H. Dong, Y. D. Gong, V. Paulose, P. Shum, and M. Olivo, "Optimum input states of polarization for Mueller matrix measurement in a system having finite polarization-dependent loss or gain," *Opt. Express* **17**, 23044 (2009).

111. A. Peinado, A. Lizana, J. Vidal, C. Iemmi, and J. Campos, "Optimization and performance criteria of a Stokes polarimeter based on two variable retarders," *Opt. Express* **18**, 9815 (2010).
112. C. Vicario, M. Shalaby, and C. P. Hauri, "Subcycle Extreme Nonlinearities in GaP Induced by an Ultrastrong Terahertz Field," *Phys. Rev. Lett.* **118**, 083901 (2017).

## **Abstract in French (Résumé en Français)**

### **1. Introduction**

Situées entre les ondes infrarouges et le domaine des micro-ondes, les ondes térahertz (THz) sont définies par la plage couvrant la gamme de fréquences de 0.1 THz à 10 THz [1]. En particulier, cette gamme de fréquences a été appelée « gap THz » en raison de l'absence de sources et de détecteurs efficaces et compacts. Au cours des deux dernières décennies, avec le développement rapide des sources de rayonnement THz et des techniques de détection, ce « gap THz » est maintenant devenu obsolète [1]. Le développement de sources THz efficaces, de détecteurs et de leurs applications ont été facilités par l'avancée des systèmes laser femtoseconde impulsive, qui ont permis de faire progresser rapidement les applications de divers domaines, tels que la physique de la matière condensée, la photonique ultrarapide, la biomédecine communications [1-4].

L'une des propriétés les plus intéressantes de cette gamme de fréquences est son énergie photonique relativement basse. Par exemple, un photon 1 THz possède une énergie de 4 meV, ce qui est beaucoup plus petit que l'énergie de la bande interdite des matériaux semi-conducteurs. En conséquence, on peut utiliser la spectroscopie THz pour effectuer une détection directe, sans contact et non-invasive, du transport ultrarapide de porteurs de charge intra-bande dans des matériaux semi-conducteurs dopés, ou pour observer la relaxation de porteurs photoexcités dans des semi-conducteurs [1-4]. Par conséquent, la spectroscopie THz devient un outil très pratique pour étudier la dynamique des porteurs de charge ultrarapides, ce qui est essentiel pour les applications de l'électronique à haute répétition opérationnelle et de l'optoélectronique.

## 2. Spectroscopie THz résolue en temps (THz-TDS)

Dans la présente étude de spectroscopie THz nonlinéaire, nous utilisons deux méthodes pour générer le rayonnement THz intense. La première source est l'antenne photoconductrice de grande-ouverture (APCGO). Nous avons développé une source APCGO basée sur le substrat de ZnSe avec le système laser 10 Hz à ALLS [5]. Ce système laser peut fournir suffisamment d'énergie laser pour la génération d'impulsions de pompe (environ 15 mJ) à 400 nm, longueur d'onde pour photo-exciter le semi-conducteur de ZnSe. La Fig. 1 montre une impulsion THz typique générée à partir de notre source APCGO. Une propriété unique de ces impulsions THz générées est la grande asymétrie dans l'amplitude des composantes positive et négative du profil temporel. Ici, une impulsion THz quasi-demi-cycle est générée naturellement. La deuxième propriété unique des ondes THz générées est la présence de basses fréquences, typiquement dans la plage de fréquences comprise entre 0,05 et 1 THz [1,5,6]. Dans le domaine temporel, cela correspond à une longue durée de demi-cycle avec une énergie pondéromotrice élevée, ce qui est avantageux pour de nombreuses applications comme l'accélération de porteurs de charge libre [4].

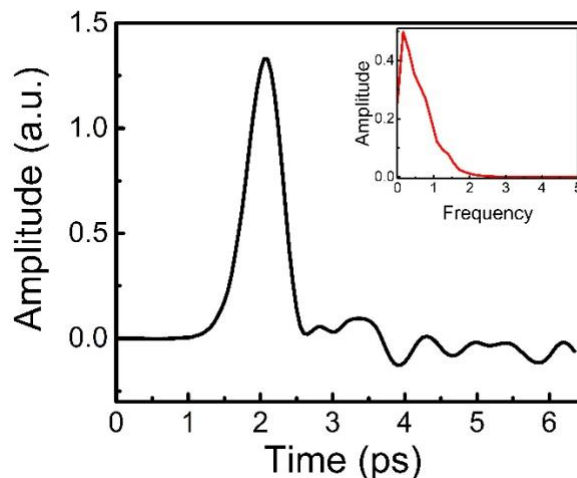


**Fig.1: Impulsion THz générée par une source APCGO THz à base de substrat ZnSe.**

La deuxième source utilisée dans cette étude est le redressement optique dans un cristal nonlinéaire de  $\text{LiNbO}_3$ . En raison de la grande efficacité de conversion à 800 nm, le système THz-TDS basé sur la source de  $\text{LiNbO}_3$  peut fonctionner avec un système laser à taux de répétition élevé [1,7]. Notre système a été développé sur la ligne du faisceau à 2.5 kHz de ALLS, ce qui a permis d'obtenir une sensibilité élevée, un meilleur ratio de signal sur bruit et une vitesse de balayage élevée. Le champ électrique crête de cette source THz est compris entre 60 et 70 kV/cm et l'impulsion générée a un profil temporel quasi-mono-cycle et un spectre centré à 0.75 THz (Fig. 2) [8].

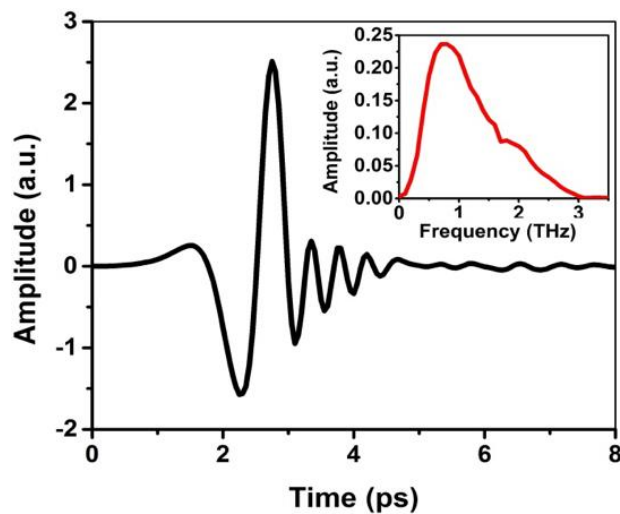


**Fig.2 : Impulsion THz générée par une source de  $\text{LiNbO}_3$ .**

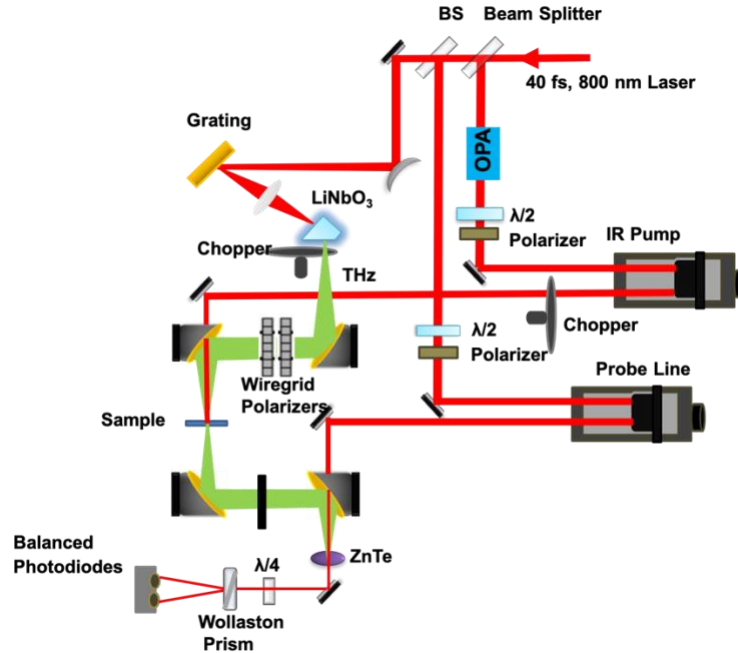


**Fig.3 : Le montage expérimental du système de spectroscopie THz résolue en temps.**

La spectroscopie THz résolue en temps est basée sur la génération et la détection cohérente de l'impulsion THz. La détection THz est réalisée par la méthode de l'échantillonnage électro-optique, où une sonde optique est utilisée pour balayer la forme d'onde THz en utilisant l'effet de Pockels [9]. L'amplitude et la phase de l'impulsion THz peuvent donc être résolues directement. La Fig. 3 montre un système THz-TDS typique avec une source de LiNbO<sub>3</sub>. Ici, un faisceau laser optique est séparé en deux parties. Une partie est utilisée pour la génération d'onde THz et l'autre, à faible énergie, sert de faisceau sonde pour la détection des ondes THz. Pour effectuer des mesures non-linéaires, on peut utiliser une paire de polariseurs linéaire pour contrôler l'énergie THz incidente ou modifier la tension de polarisation appliquée à l'APCGA. Ce montage aussi permet d'effectuer une spectroscopie de pompe-optique et sonde-THz en ajoutant une autre ligne de faisceau [10-12].

### 3. Spectroscopie THz nonlinéaire du graphène

Nous avons étudié l'effet de la température et l'effet de champ THz sur la réponse non-linéaire du graphène monocouche [12,13]. Pour étudier l'effet de température (condition ambiante), nous avons testé deux types d'échantillons de graphène implicite à grande échelle sur le même substrat de 4H-SiC, préparés par des méthodes de croissance épitaxiale à partir de 4H-SiC puis en transférant le graphène déposé par vaporisation chimique (CVD) sur un substrat de 4H-SiC. Les échantillons de graphène CVD ont montré des concentrations de dopage de trous élevés, alors que les échantillons de graphène épitaxiale ont montré un dopage d'électrons relativement faible. Nous avons effectué une spectroscopie linéaire THz sur les échantillons de graphène à diverses températures allant de la température ambiante jusqu'à 300 °C. L'impulsion THz est générée par redressement optique d'impulsions laser à 800 nm et 40 fs de durée dans un cristal de LiNbO<sub>3</sub>. Dans cette étude, on a contrôlé le champ THz à environ 1.5 kV/cm pour éviter tout effet non-linéaire induit par un champ électrique THz intense.

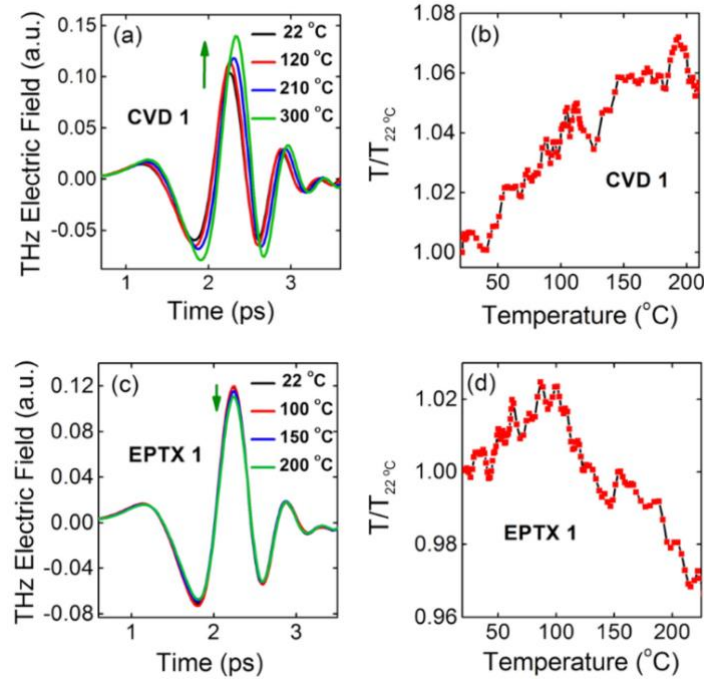


**Fig.4 : Mesures THz-TDS en changeant la température ambiante : les impulsions transmises (a) et (c) et le champ de crête normalisé (b) et (d) pour le graphène CVD et épitaxié.**

Les Figs. 4 (a) et (c) montrent les mesures de THz-TDS en faisant varier les températures ambiantes pour le graphène CVD et épitaxié. Les Figs.3.1. (b) et (d) montrent la transmission du champ crête THz correspondant qui est normalisé à la transmission THz de l'échantillon à la température ambiante. Les deux échantillons de graphène présentent un comportement presque opposé lorsque la température augmente. La transmission THz du graphène CVD dopé- $p$  augmente généralement avec l'augmentation de la température, tandis que la transmission THz du graphène épitaxié dopé- $n$  augmente légèrement, mais la tendance générale est une diminution de la transmission lorsque la température augmente. Nous attribuons ces observations à un changement de niveau de Fermi du graphène suite à la désorption de molécules d'eau et d'oxygène dans l'air entourant le graphène, ce qui conduit à un dopage supplémentaire en électrons [12,14].

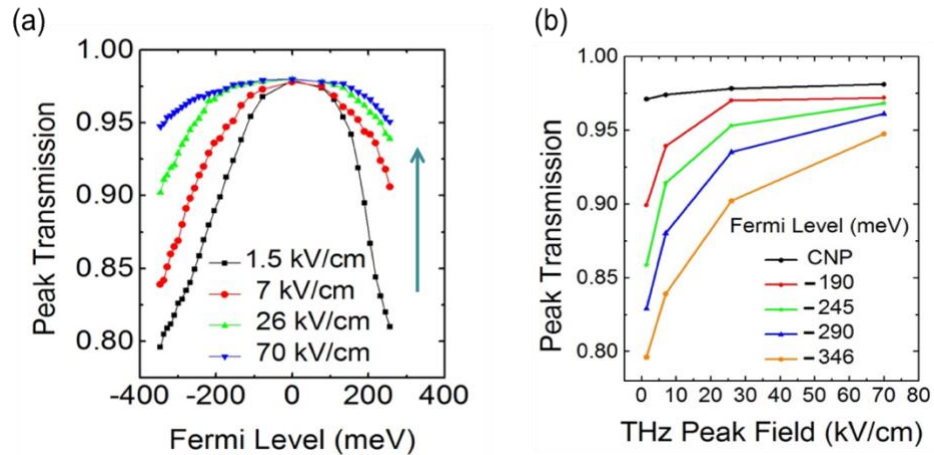


**Fig.5 : THz-TDS non-linéaire du graphène à grille : (a) Transmission de champ crête THz en fonction du niveau de Fermi pour différents champs incidents. (b) Dépendance du champ transmis en fonction du champ incident pour différents niveaux de Fermi.**

Pour étudier l'effet du champ THz, on a utilisé un échantillon de graphène à grille, dans laquelle le niveau de Fermi peut être contrôlé. Nous avons mesuré les impulsions THz transmises à travers de graphène et aussi à travers la partie de l'échantillon sans graphène et avons tracé la transmission du champ crête en fonction de l'énergie du niveau de Fermi de graphène à différentes intensités de champ. Tel que présenté par la Fig. 5 (a), la transmission du champ crête atteint une valeur maximale lorsque l'énergie du niveau de Fermi est proche du point neutre de la charge. Ici, la densité des porteurs de charge est minimale et la transmission maximale est obtenue car la conductivité THz est la plus basse. D'autre part, comme indiqué par la flèche sur la Fig. 5 (a), il a été constaté que les tendances des champs crêtes THz transmis montrent une transmission accrue avec une augmentation du champ THz. Lorsque la concentration du dopage diminue, l'augmentation relative de la transmission avec l'augmentation du champ THz devient moins grande, ce qui indique une diminution des effets non-linéaires du champ THz lorsque la

concentration de dopage est réduite. Ces observations soulignent que la réponse non-linéaire de l'échantillon du graphène dépend principalement de la présence de porteurs libres et peut s'expliquer par une diffusion des porteurs lorsque le champ THz est augmenté.

## **5. Optique THz non-linéaire sous-cycle**

Dans cette étude, nous avons étudié l'optique THz non-linéaire sous-cycle en utilisant la dynamique de porteurs de charge dans un semi-conducteur d' $\text{In}_{0.53}\text{Ga}_{0.47}\text{As}$  dopé [15]. À champ intense, une réponse non-linéaire THz peut être introduite par l'effet de diffusion inter-vallée [16,17]. En fait, pour les non-linéarités induites par la diffusion, il n'y a pas de différence fondamentale entre le semi-métal graphène et les semi-conducteurs conventionnels. L'augmentation du taux de diffusion entraîne une diminution de la conductivité THz, qui donne lieu à une augmentation de transmission THz. Cependant, nous avons besoin d'une modulation ou d'un contraste plus élevé entre les champs hauts et bas pour obtenir une observation expérimentale claire [5,6,18]. Ici, nous avons utilisé l'APCGO, qui a une fréquence centrale plus basse et une durée de l'impulsion demi-cycle plus longue.

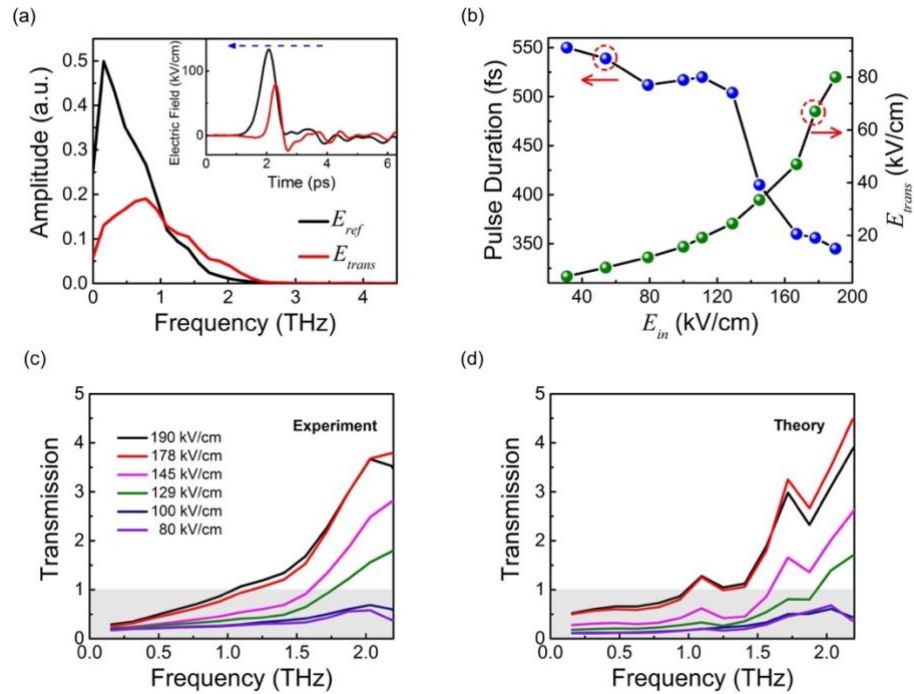


**Fig.6 : (a) Spectre en amplitude des impulsions THz transmises à travers le substrat ( $E_{ref}$ ) et l'échantillon ( $E_{trans}$ ). Encadré : formes d'ondes THz correspondantes. (b) Dépendance du champ électrique THz transmis et de la durée de l'impulsion (c) Spectres de transmission mesurés avec différent champs incidents (d) Spectres de transmission calculés avec le modèle théorique.**

La Fig. 6 (a) présente les formes d'onde THz transmises à travers le substrat d'InP et l'échantillon semi-conducteur d' $In_{0.53}Ga_{0.47}As$  lorsque le champ crête incident est à 190 kV/cm. Nous avons observé la génération de hautes fréquences (HFG) avec une augmentation d'amplitude spectrale allant d'environ 1 THz à 2.5 THz. Pour étudier l'effet non-linéaire, nous avons fait varier le champ crête incident de 31 kV/cm à 190 kV/cm. La Fig. 6 (b) représente les champs crêtes THz transmis et les durées des demi-cycles en fonction du champ THz incidents. L'échantillon a montré une transmission linéaire aux champs bas, tandis qu'une forte augmentation de la transmission non-

linéaire est observée aux champs élevés. Pendant ce temps, la durée du demi-cycle se maintient au-dessus de 500 fs pour des champs faibles et diminue rapidement lorsque le champ est supérieur à 129 kV/cm, où des transmissions supérieures à l'unité ont été observées aux fréquences élevées (Fig. 6(c)). Comme on peut le voir sur la Fig. 6 (c), la région d'augmentation d'amplitude spectrale s'agrandit avec le champ et couvre la plage spectrale au-dessus de 1 THz.

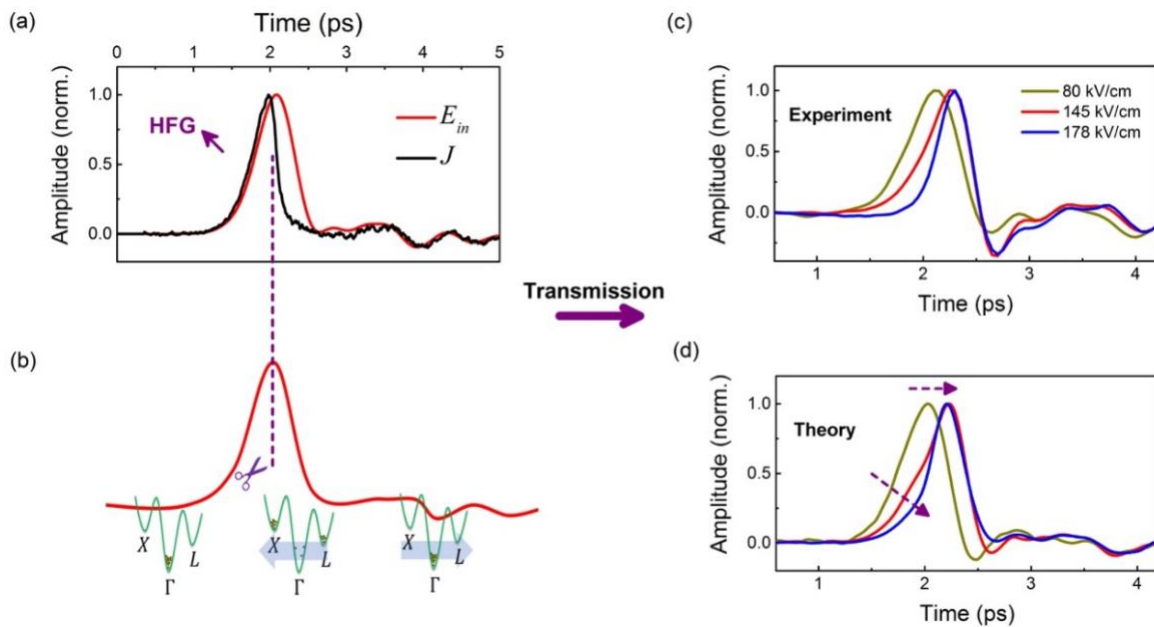


**Fig.7 : (a) Forme d'onde THz incidente et la densité de courant calculée avec un champ incident de 190 kV/cm. (b) Schéma de l'expérience dans l'espace de la bande d'énergie : une rampe THz intense induit une diffusion inter-vallée de porteurs de charge. L'augmentation de champ crête cause un amortissement de la densité de courant sous-cycle et une augmentation du temps de relaxation total des porteurs de charge. (c) Impact de la chute de courant sur les formes d'onde THz transmises à différents champs testés. (d) Ondes THz transmises normalisées obtenues par simulation.**

Pour comprendre la dynamique des porteurs non-linéaires sous-cycle, nous avons effectué une analyse théorique dans le domaine temporel en utilisant l'équation de transmission d'une couche mince [16,19,20]:

$$E_{trans}(t) = \frac{1}{Y_0 + Y_S} \left( \frac{4Y_S}{N+1} E_{in}(t) - J(t)d \right)$$

Ici,  $d$  est l'épaisseur de l'échantillon.  $Y_0$  et  $Y_S$  est l'admittance en espace libre et l'admittance du substrat avec  $N$ , l'indice de réfraction de l'InP [16,17]. L'équation a été ajustée pour la configuration où l'onde THz est transmise d'abord au travers du substrat [15]. Dans le régime des couches minces, on suppose que tous les porteurs de charge subissent le même champ d'accélération, qui est de 80 kV/cm lorsque le champ crête incident est de 190 kV/cm. Comme montré dans la relation linéaire entre la densité de courant et le champ émis, une distorsion non-linéaire ultrarapide sur une densité de courant périodique devrait contenir des harmoniques d'ordre élevé de la fréquence d'attaque et une bande de haute fréquence continue pourrait être générée lorsque des impulsions sous-cycle sont utilisées. Pour caractériser la dynamique des porteurs de charge transitoire, nous avons utilisé l'approche Monte-Carlo d'ensemble à bande analytique comme une solution de l'équation de transport de Boltzmann [21,22]. Contrairement à la génération d'harmonique par une impulsion laser dans l'infrarouge moyen, le mouvement balistique peut être en grande partie inhibé aux énergies élevées en raison du champ relativement faible mais variant plus lentement avec une durée de 1 ps [19,23]. La dynamique de chaque porteur de l'ensemble a été simulée simultanément et a été déterminée par la vitesse de dérive moyenne.

La Fig. 6 (d) montre les transmissions THz calculées pour différentes intensités de champ. Une bande de haute fréquence continue est générée en raison de la chute de courant sous-cycle, comme illustré à la Fig. 7 (a). Cette chute rapide de la densité de courant provoque un décalage temporel du champ crête de l'onde THz transmise. Aux champs élevés, la partie arrière du demi-cycle a une

conductivité beaucoup plus basse et pousse à son tour le pic de THz dans le temps. Ces observations sont reproduites avec précision par notre analyse dans le domaine temporel.

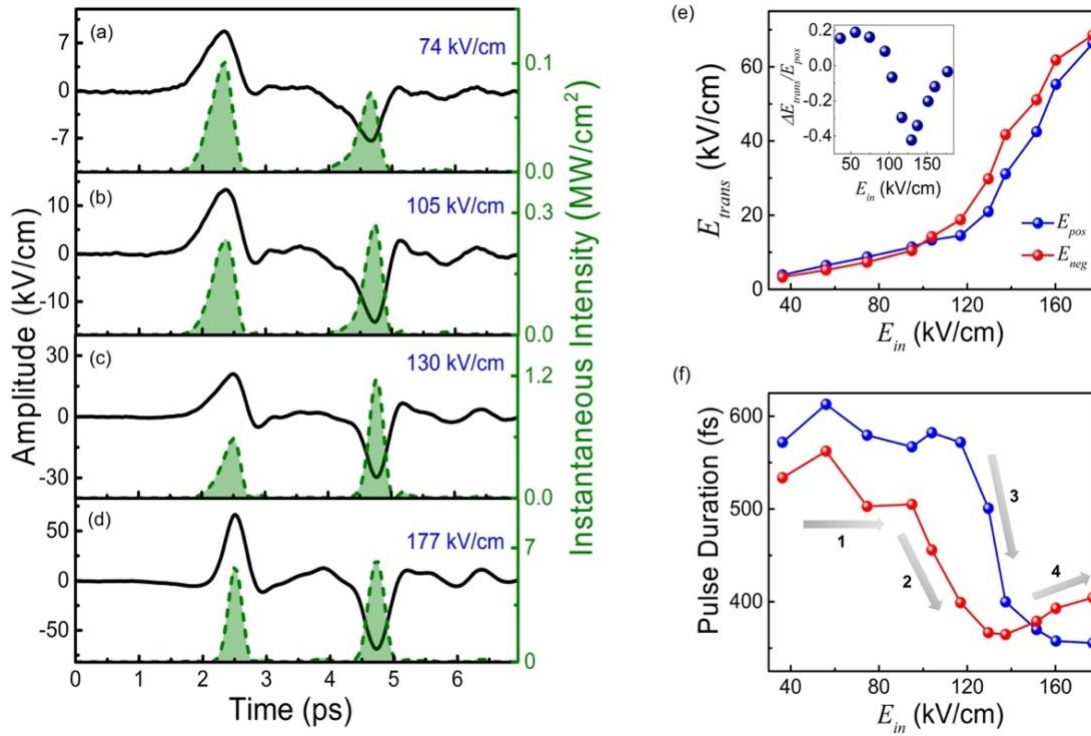


**Fig.8 : Impulsions THz transmises (courbe noire continue) et intensité instantanée du THz (courbe verte en pointillés) à divers champs incidents de (a) 74 kV/cm. (b) 105 kV/cm. (c) 130 kV/cm. et (d) 177 kV/cm. (e) les champs transmis des extrêmes négatif ( $E_{neg}$ ) et positif ( $E_{pos}$ ) par rapport au champ incident. (f) Dépendance au champ des durées du demi-cycle (amplitude FWHM). Quatre régions de champ peuvent être identifiées : 1, le régime linéaire; 2, troncature du courant sur la polarité négative; 3, troncature de courant sur la polarité positive et 4, élargissement d'impulsion de la polarité négative.**

Nous avons aussi effectué des expériences THz-TDS non-linéaires sur l'échantillon d'InGaAs avec une impulsion THz monocycle. Quatre formes d'onde transmises à différentes intensités de

champ sont illustrées aux Figs. 8 (a), (b), (c) et (d). Les champs de crête transmis [Fig. 8 (e)] ainsi que les durées demi-cycles de chaque impulsion [Fig. 8 (f)] sont extraits pour les  $E_{pos}$  et  $E_{nég}$ . Aux champs bas (région 1 sur la Fig. 8 (f)), des réponses linéaires sont obtenues et les formes d'onde THz transmises restent similaires aux impulsions incidentes. Lorsque le champ de crête est augmenté à 105 kV/cm, nous observons une augmentation claire de l'amplitude de  $E_{nég}$  (Fig. 8 (b)), où  $E_{nég}$  devient plus élevé que  $E_{pos}$  après la transmission. Cette observation peut être vue plus clairement en comparant les intensités instantanées dans le domaine temporel, où la différence atteint un maximum lorsque le champ incident est à 130 kV/cm [Fig. 8 (c)]. Pendant ce temps, la durée du demi-cycle  $E_{nég}$  diminue d'environ 500 fs à 360 fs, tandis que celle de  $E_{pos}$  est encore supérieure à 500 fs (région 2 de la Fig. 8 (f)). Cette inversion de la forme d'onde est provoquée par les porteurs de charge résiduels dans les vallées supérieures après excitation, ce qui entraîne une accélération supérieure qui peut décélérer et ré-accélérer rapidement les porteurs restants dans la vallée, puis les faire rediffuser dans les vallées supérieures. Cependant, quand  $E_{pos}$  est suffisamment intense (région 3 sur la Fig. 8 (f)), la différence commence à diminuer et la durée de l'impulsion diminue de 575 à moins de 400 fs. Ceci est en accord avec les résultats obtenus en utilisant les impulsions demi-cycles, où la coupure du courant donne lieu à un raccourcissement de l'impulsion THz transmise. En plus, la durée des  $E_{nég}$  commence à augmenter lorsque le champ THz est supérieur à 137 kV/cm, tandis que celle de la polarité positive  $E_{pos}$  continue à diminuer (région 4 de la Fig. 8 (f)). Ceci est un résultat de la dynamique de porteurs de charge inter-vallée induite par les impulsions monocycles. Une densité de courant faible pendant la transmission permet à davantage de composants basse fréquence d'être transmis à travers l'échantillon, ce qui augmente la durée totale du demi-cycle  $E_{nég}$ .

## 6. Effets des dynamiques de porteur de charges inter-bande

En continuant à augmenter le champ maximal THz, on pourrait observer une transition de la non-linéarité intra-bande à une non-linéarité inter-bande. Pour cette étude, nous avons effectué une mesure directe de l'énergie THz transmise en utilisant une source THz intense basé sur le cristal organique de DSTMS. Cette source peut fournir un champ électrique de crête extrêmement intense de quelque MV/cm [24,25].

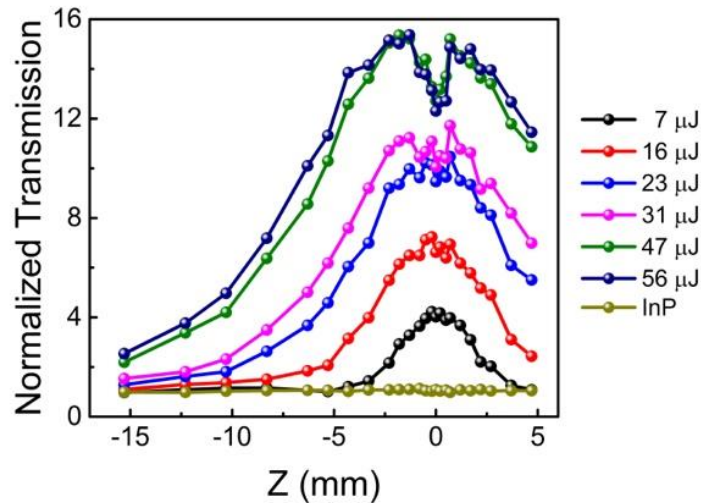


**Fig.9 : Transmission normalisée par balayage de la position Z de l'échantillon avec différentes énergies d'impulsion THz incidentes.**

La Fig. 9 montre le comportement de l'énergie THz transmise normalisée obtenue à partir des expériences de balayage Z pour plusieurs énergies THz [16,17]. Toutes les énergies THz transmises sont normalisées à l'énergie THz transmise par l'échantillon  $\text{In}_{0.53}\text{Ga}_{0.47}\text{As}$  placé à  $Z = -15.3$  mm du point focal du faisceau THz et avec une énergie d'impulsion THz de  $7 \mu\text{J}$ . En éclairant

l'échantillon avec des énergies d'impulsion THz faibles de 7 et 16  $\mu\text{J}$ , une absorption saturable claire de l'onde THz est observée lorsque l'échantillon est placé près du point focal. Des réponses linéaires avec une transmission normalisée d'environ 1 sont obtenues lorsque l'échantillon est balayé loin du point focal. L'absorption saturable de l'onde THz devient plus forte lorsque les énergies des impulsions THz sont augmentées à 23 et 31  $\mu\text{J}$ , où une transmission normalisée de 9 est observée près du point de focale. Ici, le blanchiment de l'absorption non-linéaire commence à avoir lieu à  $Z > 10$  mm et nous observons un plateau de la transmission normalisée autour du point focal. En utilisant les énergies d'impulsion THz maximales testées de 47 et 56  $\mu\text{J}$ , nous observons une réduction de la transmission normalisée à proximité du point focal. Cette réponse inhabituelle suggère que la conductivité THz commence à augmenter à des champs extrêmement élevés de quelques MV/cm.

Comme montré ici par la Fig. 9, les réponses générales sont toujours dominées par l'absorption saturable à cause du chauffage des porteurs de charge intra-bandes. En augmentant l'intensité des impulsions THz, la transmission de l'onde THz augmente environ 17 fois et l'échantillon devient presque transparent. Cependant, l'inclinaison de la courbe de balayage  $Z$  autour du point focal suggère que d'autres effets, qui peuvent augmenter la conductivité THz, se produisent sous l'illumination d'une intensité THz extrêmement intense. Cette augmentation de la conductivité peut être réalisée en ajoutant des porteurs de charges libres à mobilité élevée dans l'échantillon de semi-conducteur. Deux voies inter-bandes sont possibles ici, qui est l'ionisation par impact et l'effet tunnel de Zener [20,26-29].

Nous estimons l'efficacité de l'ionisation impacte et de l'effet tunnel de Zener à l'aide du modèle proposé par Keldysh et Kane [30,31]. Le taux d'ionisation impacte est de l'ordre  $10^{12} \text{ s}^{-1}$  pour des hautes énergies supérieures à 1.4 eV et devient comparable au taux de diffusion inter-vallée lorsque

l'énergie des électrons est bien au-dessus du bas de la bande de conduction (environ 3 eV pour l' $\text{In}_{0.53}\text{Ga}_{0.47}\text{As}$ ). D'autre part, l'effet tunnel de Zener est également un phénomène prononcé dans les semi-conducteurs à bande interdite directe comme l' $\text{In}_{0.53}\text{Ga}_{0.47}\text{As}$ . Aux champs élevés supérieurs à environ 1.5 MV/cm, l'effet tunnel de Zener peut aussi générer une densité de porteurs proche de la densité de dopage initiale avec un temps inférieure à 100 fs. Cependant, l'augmentation de la densité de porteurs réduit le champ d'attaque instantané sur le film mince et, par conséquent, les réponses non-linéaires des semi-conducteurs dopés sont toujours dominées par la thermalisation des porteurs induite par les effets de diffusion.

1. H. A. Hafez, X. Chai, A. Ibrahim, S. Mondal, D. Férachou, X. Ropagnol, and T. Ozaki, "Intense terahertz radiation and their applications," *Journal of Optics* **18**, 093004 (2016).
2. X. C. Zhang, *Introduction to THz Wave Photonics* (New York Springer 2010).
3. R. Ulbricht, E. Hendry, J. Shan, T. F. Heinz, and M. Bonn, "Carrier dynamics in semiconductors studied with time-resolved terahertz spectroscopy," *Rev. Mod. Phys.* **83**, 543 (2011).
4. T. Kampfrath, K. Tanaka, and K. A. Nelson, "Resonant and nonresonant control over matter and light by intense terahertz transients," *Nat. Photon.* **7**, 680 (2013).
5. X. Ropagnol, M. Khorasaninejad, M. Raeiszadeh, S. Safavi-Naeini, M. Bouvier, C. Y. Côté, A. Laramée, M. Reid, M. A. Gauthier, and T. Ozaki, "Intense THz Pulses with large ponderomotive potential generated from large aperture photoconductive antennas," *Opt. Express* **24**, 11299 (2016).

6. X. Ropagnol, F. Blanchard, T. Ozaki, and M. Reid, "Intense terahertz generation at low frequencies using an interdigitated ZnSe large aperture photoconductive antenna," *Appl. Phys. Lett.* **103**, 161108 (2013).
7. F. Blanchard and K. Tanaka, "Improving time and space resolution in electro-optic sampling for near-field terahertz imaging," *Opt. Lett.* **41**, 4645 (2016).
8. H. A. Hafez, I. Al-Naib, K. Oguri, Y. Sekine, M. M. Dignam, A. Ibrahim, D. G. Cooke, S. Tanaka, F. Komori, H. Hibino, and T. Ozaki, "Nonlinear transmission of an intense terahertz field through monolayer graphene," *AIP Advances* **4**, 117118 (2014).
9. Q. Wu and X. C. Zhang, "Free-space electro-optic sampling of terahertz beams," *Appl. Phys. Lett.* **67**, 3523 (1995).
10. H. A. Hafez, I. Al-Naib, M. M. Dignam, Y. Sekine, K. Oguri, F. Blanchard, D. G. Cooke, S. Tanaka, F. Komori, H. Hibino, and T. Ozaki, "Nonlinear terahertz field-induced carrier dynamics in photoexcited epitaxial monolayer graphene," *Phys. Rev. B* **91**, 035422 (2015).
11. H. A. Hafez, P. L. Lévesque, I. Al-Naib, M. M. Dignam, X. Chai, S. Choubak, P. Desjardins, R. Martel, and T. Ozaki, "Intense terahertz field effects on photoexcited carrier dynamics in gated graphene," *Appl. Phys. Lett.* **107**, 251903 (2015).
12. H. A. Hafez, X. Chai, Y. Sekine, M. Takamura, K. Oguri, I. Al-Naib, M. M. Dignam, H. Hibino, and T. Ozaki, "Effects of environmental conditions on the ultrafast carrier dynamics in graphene revealed by terahertz spectroscopy," *Phys. Rev. B* **95**, 165428 (2017).
13. H. Razavipour, W. Yang, A. Guermoune, M. Hilke, D. G. Cooke, I. Al-Naib, M. M. Dignam, F. Blanchard, H. A. Hafez, X. Chai, D. Ferachou, T. Ozaki, P. L. Lévesque, and R. Martel, "High-field response of gated graphene at terahertz frequencies," *Phys. Rev. B*

- 92**, 245421 (2015).
14. F. Schedin, A. K. Geim, S. V. Morozov, E. W. Hill, P. Blake, M. I. Katsnelson, and K. S. Novoselov, "Detection of individual gas molecules adsorbed on graphene," *Nat. Mat.* **6**, 652 (2007).
  15. X. Chai, X. Ropagnol, S. M. Raeis-Zadeh, M. Reid, S. Safavi-Naeini, and T. Ozaki, "Subcycle Terahertz Nonlinear Optics," *Phys. Rev. Lett.* **121**, 143901 (2018).
  16. L. Razzari, F. H. Su, G. Sharma, F. Blanchard, A. Ayeshehshim, H. C. Bandulet, R. Morandotti, J. C. Kieffer, T. Ozaki, M. Reid, and F. A. Hegmann, "Nonlinear ultrafast modulation of the optical absorption of intense few-cycle terahertz pulses in n-doped semiconductors," *Phys. Rev. B* **79**, 193204 (2009).
  17. G. Sharma, L. Razzari, F. H. Su, F. Blanchard, A. Ayeshehshim, T. L. Cocker, L. V. Titova, H. C. Bandulet, T. Ozaki, J. C. Kieffer, R. Morandotti, M. Reid, and F. A. Hegmann, "Time-Resolved Terahertz Spectroscopy of Free Carrier Nonlinear Dynamics in Semiconductors," *IEEE Photonics J.* **2**, 578 (2010).
  18. X. Ropagnol, R. Morandotti, T. Ozaki, and M. Reid, "THz pulse shaping and improved optical-to-THz conversion efficiency using a binary phase mask," *Opt. Lett.* **36**, 2662 (2011).
  19. W. Kuehn, P. Gaal, K. Reimann, M. Woerner, T. Elsaesser, and R. Hey, "Coherent Ballistic Motion of Electrons in a Periodic Potential," *Phys. Rev. Lett.* **104**, 146602 (2010).
  20. W. Kuehn, P. Gaal, K. Reimann, M. Woerner, T. Elsaesser, and R. Hey, "Terahertz-induced interband tunneling of electrons in GaAs," *Phys. Rev. B* **82**, 075204 (2010).
  21. C. Jacoboni and L. Reggiani, "The Monte Carlo method for the solution of charge transport in semiconductors with applications to covalent materials," *Rev. Mod. Phys.* **645**

- (1983).
22. A. P. Long, P. H. Beton, and M. J. Kelly, "Hot-electron transport in In<sub>0.53</sub>Ga<sub>0.47</sub>As," *J. Appl. Phys.* **62**, 1842 (1987).
  23. O. Schubert, M. Hohenleutner, F. Langer, B. Urbanek, C. Lange, U. Huttner, D. Golde, T. Meier, M. Kira, S. W. Koch, and R. Huber, "Sub-cycle control of terahertz high-harmonic generation by dynamical Bloch oscillations," *Nat. Photon.* **8**, 119 (2014).
  24. O. V. Chefonov, A. V. Ovchinnikov, S. A. Romashevskiy, X. Chai, T. Ozaki, A. B. Savel'ev, M. B. Agranat, and V. E. Fortov, "Giant self-induced transparency of intense few-cycle terahertz pulses in n-doped silicon," *Opt. Lett.* **42**, 4889 (2017).
  25. X. Chai, X. Ropagnol, A. Ovchinnikov, O. Chefonov, A. Ushakov, C. M. Garcia-Rosas, E. Isgandarov, M. Agranat, T. Ozaki, and A. Savelev, "Observation of crossover from intraband to interband nonlinear terahertz optics," *Opt. Lett.* **43**, 5463 (2018).
  26. H. Hirori, K. Shinokita, M. Shirai, S. Tani, Y. Kadoya, and K. Tanaka, "Extraordinary carrier multiplication gated by a picosecond electric field pulse," *Nat. Commun.* **2**, 594 (2011).
  27. C. Lange, T. Maag, M. Hohenleutner, S. Baierl, O. Schubert, E. R. J. Edwards, D. Bougeard, G. Woltersdorf, and R. Huber, "Extremely Nonperturbative Nonlinearities in GaAs Driven by Atomically Strong Terahertz Fields in Gold Metamaterials," *Phys. Rev. Lett.* **113**, 227401 (2014).
  28. K. Fan, H. Y. Hwang, M. Liu, A. C. Strikwerda, A. Sternbach, J. Zhang, X. Zhao, X. Zhang, K. A. Nelson, and R. D. Averitt, "Nonlinear Terahertz Metamaterials via Field-Enhanced Carrier Dynamics in GaAs," *Phys. Rev. Lett.* **110**, 217404 (2013).
  29. A. T. Tarekegne, H. Hirori, K. Tanaka, K. Iwaszczuk, and P. U. Jepsen, "Impact ionization

- dynamics in silicon by MV/cm THz fields," *New J. Phys.* **19**, 123018 (2017).
30. E. O. Kane, "Zener tunneling in semiconductors," *J. PHYS. CHEM. SOLIDS* **12**, 181 (1959).
  31. K. L V, "Kinetic theory of impact ionization in semiconductors," *Sov. Phys. JETP* **37** (1960).